



UNIVERSITÀ DEGLI STUDI DI PADOVA

Dipartimento di Geoscienze  
Direttore Prof.ssa Cristina Stefani

TESI DI LAUREA MAGISTRALE  
IN  
GEOLOGIA E GEOLOGIA TECNICA

**STRUCTURAL ANALYSIS AND 3D MODELING  
OF A POTENTIAL ANALOGUE OF HYDROCARBON  
RESERVOIR:  
THE JURASSIC SYNSEDIMENTARY STRUCTURE OF  
MONTE TESTO  
(SOUTHERN ALPS, ITALY)**

*Relatore: Prof. Matteo Massironi*  
*Correlatori: Dott. Marco Franceschi*  
*Dott. Raffaele Di Cuia*

*Laureando: Mattia Martinelli*

ANNO ACCADEMICO 2015 / 2016



*Ai miei genitori...*





# Index

<b>Index</b>	<b>5</b>
<b>Abstract</b>	<b>9</b>
<b>Introduction</b>	<b>13</b>
<b>1. Geological Setting</b>	<b>16</b>
<b>1.1 Stratigraphy</b>	<b>18</b>
<b>1.2 Tectonic evolution</b>	<b>21</b>
<b>1.3 Dolomitization in the Calcari Grigi group</b>	<b>23</b>
<b>1.4 The petroleum system</b>	<b>24</b>
<b>2. Geological map and structural analysis</b>	<b>27</b>
<b>2.1 Description of the geological map</b>	<b>28</b>
<b>2.2 Structural Analysis</b>	<b>32</b>
<b>2.2.1 Paleostress calculation and inversion methods</b>	<b>42</b>
<b>2.2.1.1 Wintensor</b>	<b>43</b>
<b>2.2.1.2 Result of stress inversion</b>	<b>45</b>
<b>2.2.1.2.1 Jurassic Paleostress</b>	<b>45</b>
<b>2.2.1.2.2 Alpine Paleostress</b>	<b>48</b>
<b>3. Porosity analysis</b>	<b>50</b>
<b>3.1 Porosity in reservoir</b>	<b>50</b>
<b>3.2 Dolomitization in the Calcari Grigi group</b>	<b>54</b>
<b>3.3 Image analysis for porosity extraction</b>	<b>56</b>
<b>3.4 Porosity analysis of the M.te Testa rocks</b>	<b>58</b>
<b>3.4.1 Sample collection and preparation</b>	<b>58</b>
<b>3.4.2 Image analysis</b>	<b>60</b>
<b>3.5 Discussion on porosity</b>	<b>74</b>

<b>4. 3D Analysis</b>	<b>76</b>
<b>4.1 Photogrammetry</b>	<b>76</b>
4.1.1 Image acquisition	79
4.1.2 Interior orientation	79
4.1.3 Exterior orientation	79
4.1.4 3D photogrammetric model	80
4.1.5 3D photogrammetric model of the Monte Testa main structure.	81
4.1.5.1 Image acquisition	81
4.1.5.2 Creation of the Photogrammetric 3D model	82
<b>4.2. 3D topographic model</b>	<b>85</b>
4.2.1 Lidar DTM and topography	85
4.2.2 Integration of the Photogrammetric model with the DTM	87
<b>4.3. 3D geological modeling in Skua/Gocad</b>	<b>92</b>
4.3.1 General remarks	92
4.3.2 Geologic modelling in Skua/Gocad	94
4.3.2.1 Polylines and surfaces in Skua/Gocad	96
4.3.2.2 Structural and Stratigraphy workflow	99
4.3.2.3 Digitizing formation boundaries	108
4.3.2.4 Digitizing fault traces	110
4.3.2.5 Creation of the bounding box	112
4.3.2.6 Generation of fault surfaces	112
4.3.2.7 Generation of horizon surfaces.	114
4.3.2.8 Modelling the Monte Testa structure in the Structural and stratigraphy workflow	122
4.3.2.9 Modelling of dolimitized bodies.	132
4.3.2.10 Features of the Monte Testa structure 3D geologic model	135
<b>5. Porosity distribution</b>	<b>141</b>
<b>5.1 The geostatistic</b>	<b>141</b>

<b>5.2 Distribution of porosity in the Monte Testa 3D model</b>	<b>146</b>
<b>5.3 Results from the porosity distribution</b>	<b>149</b>
<b>6. Conclusion</b>	<b>153</b>
<b>7. Bibliography</b>	<b>157</b>
<b>8. Thanks</b>	<b>163</b>



## **Abstract**

Structural traps created by synsedimentary extensional tectonics events can hold very interesting hydrocarbon accumulation and for this reason, they are a main target for the hydrocarbon exploration. Furthermore, the faults generated during extensional events can favour the circulation of dolomitizing fluids, leading to the formation of fault related dolomitized bodies that can strongly improve the porosity framework. In the last few years, this type of bodies received particularly attention by the hydrocarbon industry, due to the decrease of conventional reservoir discoveries. However, structural network, porosity distribution, shape and geometry of the fault related dolomitized bodies and the porosity evolution of these types of reservoirs are difficult to predict only on the bases of well-logs and seismic information. The study of outcrop analogues can help to solve these issues.

In this work I focused my attention to the carbonate platform of the Calcari Grigi group (formed by Monte Zugna, Loppio and Rotzo Formations), located on the Trento platform in the Southern Alps, which was extensively affected by synsedimentary extensional tectonic during the Early Jurassic. This tectonic event led to the tilting of the Loppio Formation and caused abruptly change of thickness in the Rotzo Formation. The extension ceased during the deposition of the upper part of the Rotzo Formation, which seals the Jurassic faults.

During the late Paleocene-early Eocene, the Alpine tectonics reactivated, with a strike slip movement, the Jurassic faults allowing the circulation of dolomitizing fluids and leading to the formation of secondary fault-related dolomitized bodies. A Jurassic synsedimentary structure affected by secondary dolomitization is spectacularly exposed near the Monte Testa on the Asiago Plateau.

In this work a geological map, structural studies, porosity analysis, 3D photogrammetric model and 3D geomodel were realized in order to reconstruct the tectonic evolution, porosity distribution and reservoir potential of M.Testa structure and better understand geometry, shape and porosity of the fault-related

dolomitized bodies. Moreover, this multi-approaching analysis allows to reconstruct the complex porosity evolution of the potential reservoirs.

The final results have shown that during the Jurassic, the early cemented tilted and high porous (8%) blocks of the Loppio Formation were put in contact laterally and above with the low porous (0%) Rotzo Formation, creating important potential hydrocarbon traps on the upper part of the tilted blocks. At that time the Zugna Formation likely had a porosity given only by fracturing (1%), hence fluids might have circulated from depth up to potential Loppio reservoir following the extensional fault network. Starting from this moment onwards the porosity of the Loppio Formation began to decrease due to cementation. During Late Paleocene-Early Eocene, the formation of the fault-related dolomitized bodies within reactivated fault zones gave a new chance to the reservoir potential of the M. Testa structure. Indeed, these bodies have a porosity ranging from 0% to 10,6% with a mean of 4,7%. The higher porosity values are concentrated along the breccia fault zones enclosed within low porous and low permeable formations, confirming the strong relationship between late dolomitization and the structural network as well as the great potential of these bodies for hydrocarbon accumulation.

Le trappole strutturali create da eventi tettonici sinsedimentari estensionali possono contenere importanti quantità di idrocarburi e per questo motivo sono un target primario per l'esplorazione petrolifera. Inoltre, le faglie create da tettonica estensionale possono favorire la circolazione di fluidi dolomitizzanti i quali portano alla formazione di corpi dolomitizzati strettamente correlati alle faglie, che possono migliorare notevolmente la porosità.

A causa della diminuzione delle scoperte di giacimenti convenzionali, questi corpi dolomitizzati stanno ricevendo una particolare attenzione dall'industria petrolifera.

La geometria delle faglie, la distribuzione della porosità, la geometria e la distribuzione dei corpi dolomitizzati e l'evoluzione della porosità di questi potenziali giacimenti sono però difficili da predire basandosi solamente su informazioni di pozzo e su sezioni sismiche.

Lo studio di analoghi esumati può aiutare a risolvere questo problema.

In questo lavoro, ho concentrato la mia attenzione sulla piattaforma carbonatica del Gruppo dei Calcari Grigi (composto dalle formazioni di Monte Zugna, Loppio e Rotzo), che si trova sulla Piattaforma di Trento nel Sud Alpino e che durante il Giurassico inferiore è stata interessata da tettonica sinsedimentaria estensionale.

Questo evento tettonico ha portato al tilting della formazione di Loppio e a bruschi cambiamenti di spessore della formazione di Rotzo. La tettonica estensionale cessò durante la deposizione della parte superiore della formazione di Rotzo, la quale sigilla le faglie giurassiche.

Tra il Paleocene Superiore e l'Eocene Inferiore, le faglie giurassiche sono state riattivate in trascorrenza dalla tettonica alpina favorendo la circolazione di fluidi dolomitizzanti e la formazione dei corpi dolomitizzati correlati alle faglie.

Nei pressi del Monte Testa sul altopiano del Pasubio, affiora in maniera spettacolare una struttura sinsedimentaria giurassica interessata da dolomitizzazione secondaria.

Durante questo lavoro è stata realizzata la carta geologica, l'analisi strutturale, l'analisi di porosità, un modello fotogrammetrico e un modello 3D della struttura geologica per ricostruirne l'evoluzione tettonica, la distribuzione della porosità e

il potenziale come reservoir e per capire geometria, forma e porosità dei corpi dolomitizzati legati alle faglie. Questo approccio multi-metodologico ha inoltre permesso di ricostruire la complessa evoluzione della porosità del potenziale reservoir.

I risultati finali mostrano che durante il Giurassico inferiore, i blocchi di Loppio cementati precocemente ma ancora porosi (8%), sono stati messi in contatto lateralmente e nella parte superiore con la poco porosa e poco permeabile formazione di Rotzo (0%). Portando alla formazione di potenziali reservoir nella parte superiore dei blocchi tiltati. La formazione di Monte Zugna aveva una porosità data dalla fratturazione del 1%. I fluidi avrebbero potuto raggiungere il potenziale reservoir nel Loppio seguendo le faglie estensionali.

Da questo momento in poi la porosità del Loppio iniziò a diminuire a causa della cementazione.

Tra il Paleocene Superiore e l'Eocene Inferiore, la formazione dei corpi dolomitizzati lungo le faglie riattivate ha dato una nuova chance alle potenzialità di reservoir della struttura del Monte Testa. Questi corpi infatti hanno una porosità che può andare dallo 0 al 10,6% con una media del 4,7%. Le porosità maggiori sono concentrate lungo le breccie associate alle zone di faglia e sono racchiuse all'interno di formazioni poco porose e poco permeabili. Questo conferma la stretta relazione tra i corpi dolomitizzati e le faglie così come il loro grande potenziale per l'accumulo di idrocarburi.



**Structural analysis and 3D modeling of a potential  
analogue of hydrocarbon reservoirs: the Jurassic  
syndimentary structure of M. Testa  
(Southern Alps, Italy).**

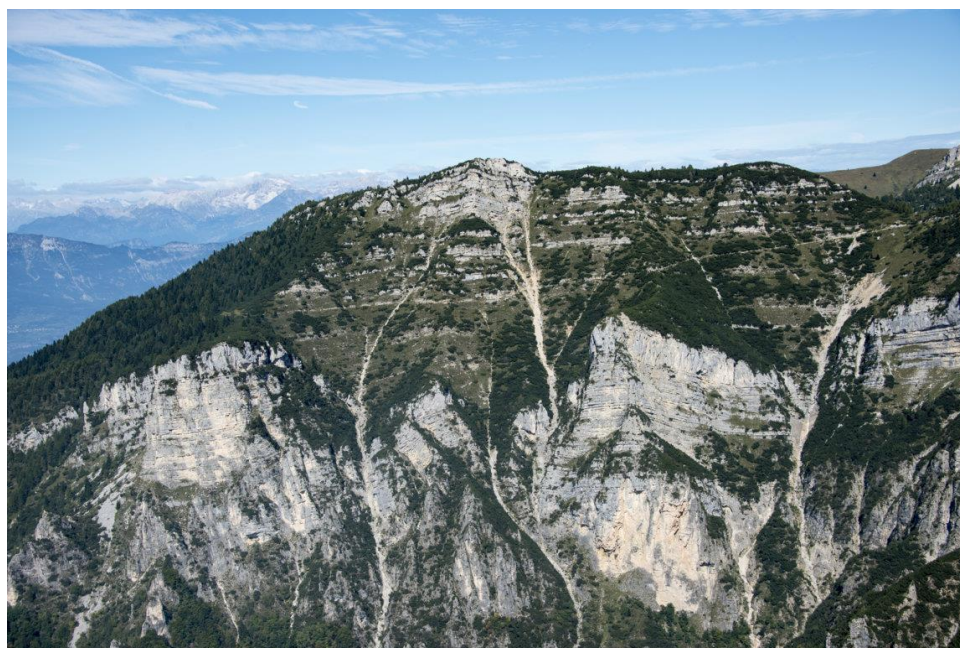
**Introduction**

Syn-sedimentary structures can form important hydrocarbon traps and potential reservoirs because of the particular relationships between trap and seal units and the potential of fault-zones as conduits for hydrocarbon. For this reason syn-sedimentary structure associated with permeable faults have been target for hydrocarbon exploration from several years.

However, in the last few years, the decrease of discoveries of conventional hydrocarbon reservoirs, pushed hydrocarbon exploration towards more complex types of reservoirs. (Møller-Pedersen & Koestler, 1997; Coward et al. 1998) Among the others are the dolomitized successions and the structurally controlled (hydrothermal) dolomites, which have gained increased attention worldwide (Davis and Smith, 2006).

It is well known that the dolomitization processes can substantially improve rock porosity and permeability (Qing Sun, 1995), two petro-physical properties that play a key role in determining the characteristics of reservoirs (Loucks R.G et al. 1986). For example, primary pores of a potential reservoir rock can be completely filled by cements and later events of hydrothermal dolomitization can create secondary porosity giving life to a new potential reservoir. Unfortunately, geometry, shape and distribution of porosity of dolomitized bodies are difficult to predict being strictly dependent from the involved dolomitization processes (Jacquemyn et al., 2015).

Study of outcrop analogues integrating geological mapping, 3D modelling and image analysis can allow to better understand the distribution of secondary porosity by hydrothermal fluid dolomitization along fault systems.



*Fig.1: The Monte Testa tectonic structure seen from NW*

The Jurassic Trento platform, located in the Southern Alps, presents several spectacularly outcrops of synsedimentary structures affected by hydrothermal dolomitization (Ronchi et al. 2012; DiCuia et al. 2011) such as Monte Toraro, Monte Cengio, Rotzo and the Monte Testa graben on the Pasubio plateau (Fig.1). The latter one, dissecting Lower Jurassic units such as Zugna, Loppio and Rotzo formations, has been investigated in this work using different techniques: geological mapping for the local context structural analysis to infer the sequence of kinematic events, image elaboration to retrieve rock porosity, and photogrammetry and 3D modelling to understand the potential as a putative reservoir of the entire structure. A particular attention has been paid to map and understand geometry and size of the dolomitized bodies. Indeed, the 3D

geometrical model shows the rock formations as well as the fault network, and the dolomitized bodies. In particular, the 3D model allows to display the shape and geometry of the dolomitized bodies and their direction of growth inferred on the bases of the field observations. Both formations and dolomitized bodies were also populated with petro-physical properties such as porosity, retrieved from image elaborations of representative thin sections, and permeability.

We have finally shown how the porosity in the region could be evolved through time during three possible steps: i) before and ii) after cementation of the potential primary reservoir (i.e. Loppio Formation), and iii) after the inception of the hydrothermal circulation which lead to the formation of later dolomitized bodies.

## 1. Geological Setting

The Pasubio Plateau is located in the southernmost part of the Southeastern Alps in North Italy and it is part of the Early Jurassic paleo-structural high of the Trento Platform (fig.2).

The Southern Alps represents the south vergent sector of the Alpine Chain, which escaped alpine metamorphism and is separated from the north-vergent collisional wedge by the Periadriatic Lineament.

The Southern Alps are carved on very different types of rocks ranging from the Variscan metamorphic basement to the Permian, Mesozoic and Tertiary clastic, volcanic and carbonate units (Bosellini et al. 2003). In particular the Trento Platform, is made up by the Late Triassic Dolomia Principale Formation and Early Jurassic Calcarei Grigi Group. The group is formed by the Monte Zugna Formation (Hettangian-Sinemurian); the Loppio Oolitic Limestone Formation (mid-Sinemurian) and Rotzo Formation (Sinemurian-Pliensbachian) (Bosellini and Hardie, 1988). Above the Calcarei grigi group is the Rosso Ammonitico unit of Middle Jurassic age.

The Calcarei Grigi Group is not well preserved on the entire platform since in the eastern part the Loppio and Rotzo formations are lacking and the Rosso Ammonitico Formation lays directly upon the Monte Zugna Formation

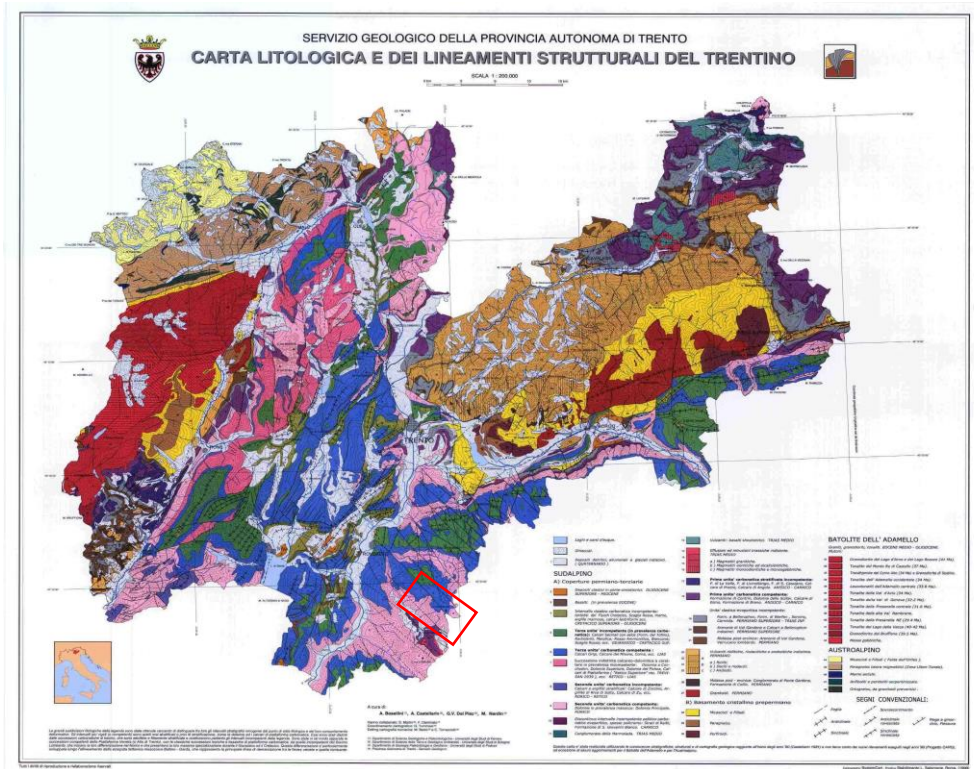


Fig. 2: Geological map of Trentino (Bosellini et al. 1999). Red rectangle: study area.

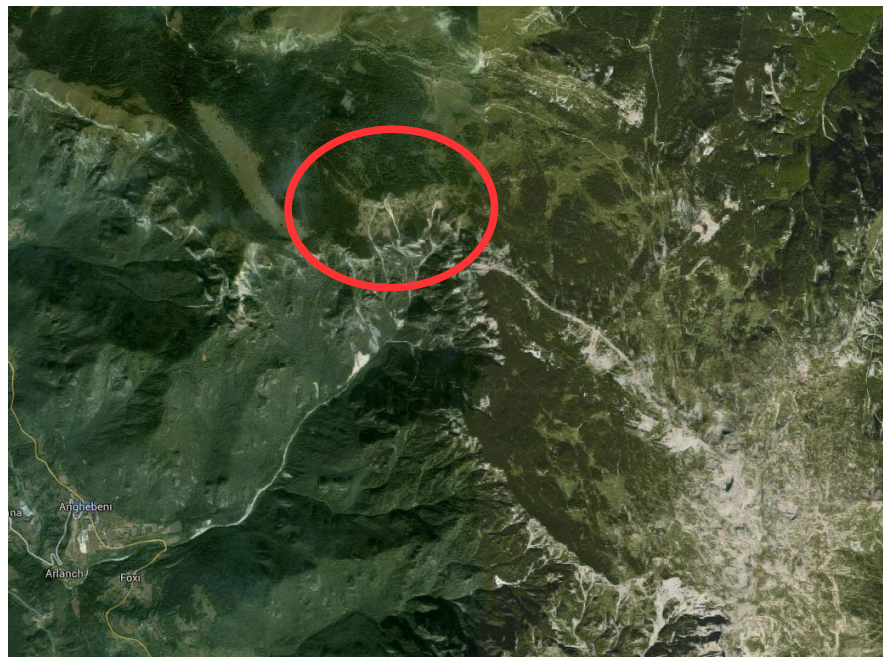


Fig.3: The area of study. Monte Testo into the red circle

## **1.1 Stratigraphy**

The Dolomia Principale is present in the area of the study, but it was not in the goal of this work, for this reason it will be described briefly. This formation (DP, Norian-Rhaetian) has a thickness ranging from 500 to 1500 m, is formed by a well stratified succession of metric peritidal cycles and presents a widespread early dolomitization (Iannance and Frisia, 1994).

### **Monte Zugna Formation (FMZ, Hettangian-Early Sinemurian).**

The Monte Zugna Formation is represented by three different shallow water lithofacies (Masetti et al., 1998; Romano et al., 2005): A) strongly bioturbate micritic or bioclastic oolitic limestones in metric or sub-metric cycles; B) stromatolitic limestones organized in peritidal successions characterized by metric cycles C) pseudo-nodular micritic limestones and dark marls.

The lower part of the formation presents a widespread early dolomitization similar to that of the Dolomia Principale Formation from which it is hardly recognizable.

The depositional environment of this formation is a tidal flat passing progressively to a subtidal environment.

### **Loppio Oolitic Limestone Formation (LOP, mid-Sinemurian)**

The Loppio Oolitic limestone testifies a deepening of the sedimentary environment (Masetti et al. 1998). It is formed by a sequence of poorly stratified oolitic limestones (grainstone) arranged in metric to decametric strata. The grains are mainly formed by ooids and in some cases intraclasts and bioclasts, welded together by a spatic cement. The top of the formation is characterized by an unconformity and its thickness within the Trento platform increases from the east, where it presents a minimum of 30 m on the Asiago plateau, to the west, where it reaches the maximum value of 200 m at the platform margin. This gradual increase in thickness, gives to the Loppio Formation a prismatic shape suggesting



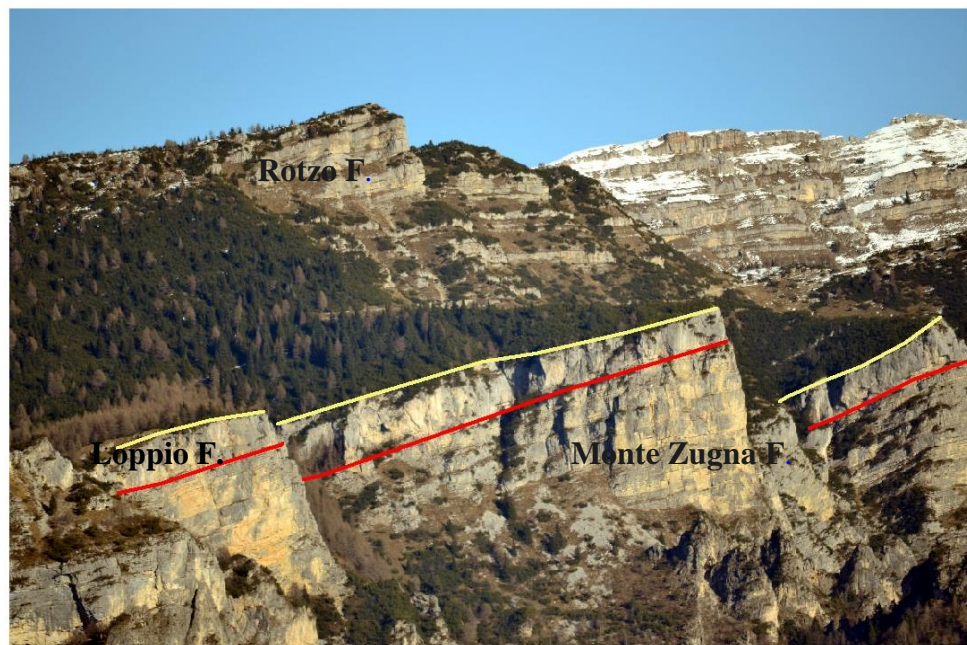
that it represents a set of coastal bodies that followed the rising of the sea level.

### **Rotzo Formation (RTZ, Sinemurian – Pliensbachian)**

The formation was deposited in a subtidal environment (Clari 1976; Masetti et al, 1998) and it is organized in asymmetrical, thickening and shallowing upward cycles (Masetti et al. 1998).

It is divided into two overlapping litofacies: i) the lower one is characterized by calcareous packstones interleaved by decimetric calcareous-marl layers; ii) the upper one is characterized by Lithotis mounds with lenticular and tabular shapes.

The depositional environment of the Rotzo Formation was interpreted by Bosellini and Broglio-Loriga (1971) as a lagoon enclosed by marginal oolitic bodies and by Masetti et al. (1998) as a ramp lagoon with a gentle regional westward slope bounded by coeval oolitic bodies.



*Fig.4: The Calcari Grigi group of the Pasubio Plateau (Looking towards Monte Testa from Monte Zugna)*

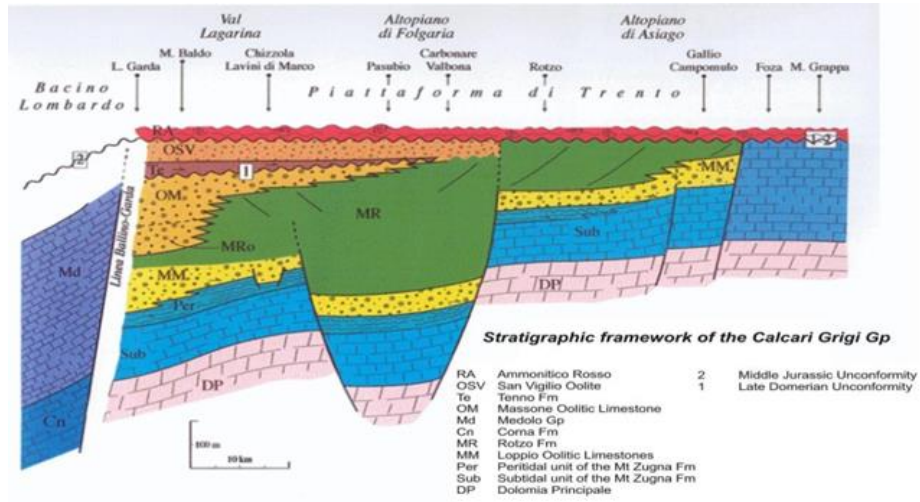


Fig.5: Stratigraphic framework of the Calcari Grigi group on the Trento Platform, E-W cross section (M. Avanzini et al. 2002)



## 1.2 Tectonic evolution

From the Late Triassic onwards, the Southern Alps underwent two important tectonic events: The first was the Late Triassic-Early Jurassic east-west extension due to the opening of the Piedmont and North Atlantic Oceans. During this event, the Dolomia Principale platform was fragmented into N-S trending paleostructural domains that from west to east are: the Lombardian Basin, the Trento Platform, the Belluno basin and the Friuli Platform (Fig. 6), (Bosellini et al. 1981).

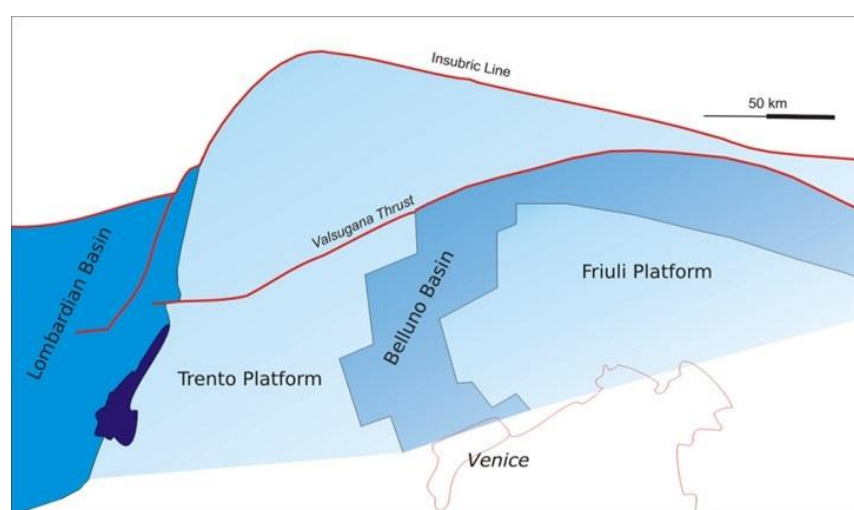


Fig.6: Paleogeography of the Southern Alps during Lias (Modified after Moretti 2007)

The Trento Platform, where our study area is located extends in an N-S direction and covers a wide region going from Verona to Cortina. During the Early Jurassic, on the Trento Platform a shallow-water sedimentary sequence (the Calcari Grigi group) was deposited on top of the Dolomia Principale, and along the western margin of the Platform submarine landslides developed in response to the Mesozoic extensional activity (Bertotti et al. 1993).

In the internal part of the platform, the Calcari Grigi group shows several sedimentary evidence of extensional tectonics, as testified by the large thickness variations affecting the group, especially the Rotzo Formation, and the presence of synsedimentary faults (Avanzini & Masetti, 1992; Avanzini 1994; Zampieri 1995, 1996; Franceschi et al., 2014). Relevant examples are Monte

Conello and Monte Testa structure.

At the end of the Jurassic, the platform drowned definitively leading to a pelagic condensed sedimentation with the deposition of the Rosso Ammonitico Veronese. In the last few years, new works suggest a complex tectonics setting for the Jurassic evolution of Southern Alps. In particular, an orthorhombic fault network has been recognized by analyzing variogram maps of thickness variations in the Early Jurassic sedimentary succession (Franceschi et al. 2014). According with this interpretation, Jurassic faults are organized in two sets with NNW-SSE and NE-SW directions. This suggests a non Andersonian faulting due to a true triaxial strain field (Reches, 1978; 1983; Aydin and Reches, 1983; Krantz, 1988; Healy et al. 2006) with a dominant N100° extensions during the Early Jurassic rifting (Franceschi et al., 2014).

The second main tectonic event affecting the Southern Alps, is the north-south compression caused by the collision between Europe and Africa, which lead to the formation of the Alpine chain.

According to some authors (e.g. Castellarin et al. 2010) the compression can be subdivided into three main stages: the late Cretaceous precollisional (Eo-Alpine), the Eocene collisional (Meso-Alpine) and the late Oligocene-Neogene (neo-Alpine) events. The last stage, characterized by a NNW-SSE sigma 1 orientation, is the main alpine phase recorded in the Southern Alps and led to the formation of major south verging thrusts (Valsugana Line, Belluno Line and Bassano-Valdobbiadene line) and the reactivation of Jurassic normal faults.

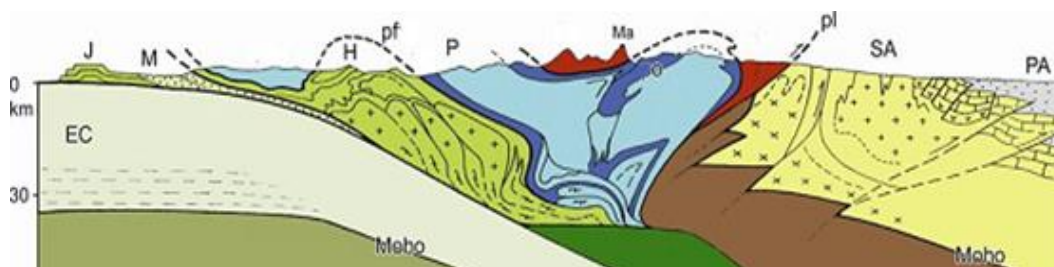


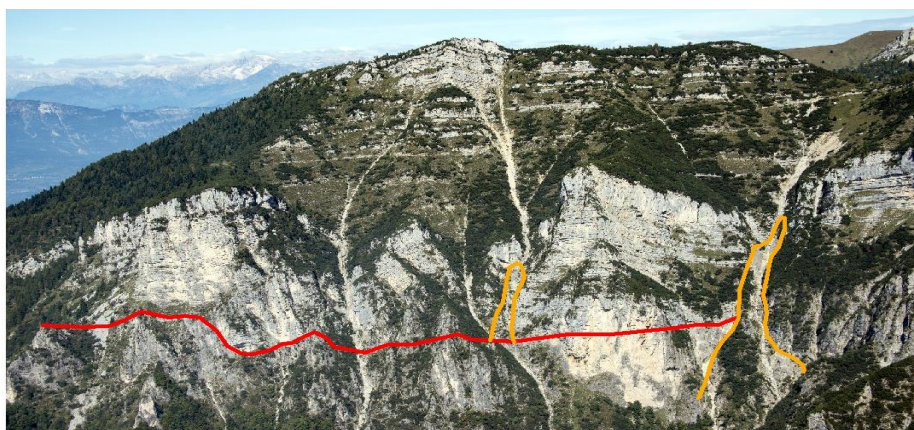
Fig.7: NW-SE cross section of the Alps. (Modified from Dal Piaz et al. 2003).  
Australpine domain, in red and brown (Ma), Penninic domain in blue (P), Helvetic basement in green(H) , Southern Alps in yellow (SA), Europea Continental crust (EC), Molasse(M), Jura belt (J)

### 1.3 Dolomitization in the Calcari Grigi group

The Calcari Grigi group underwent two major phases of dolomitization (DiCuia et al. 2011; Ronchi et al. 2012).

The first event happened during the Mesozoic, producing shallow burial and low temperature dolomites. It affected the lower part of Monte Zugna formation with a widespread dolomitization and an undulatory front, making difficult to recognize the boundary with the underlying Dolomia Principale formation.

The second event is represented by hydrothermal fault related dolomites which appear as pinnacle-shaped bodies and related dolomite fingers (DiCuia et al., 2011). In this case, the dolomitization is usually limited to the Monte Zugna and Loppio formations and only along major faults might reach younger formations. This pattern suggests that the fault network have strongly controlled the paleo-hydrological system and consequently, the dolomitizing fluid. This event probably occurred between the Oligocene and the early Miocene when the tectonic loading caused by the growth of the Alpine Chain, forced pressurized fluids to move from the collisional zone to the foreland according to a general “squeegee dolomitization model” (Ronchi et al. 2012).



*Fig. 8: The Monte Testo structure. In red the undulatory front of the first dolomitization phase. In yellow the fault related dolomitized bodies*

## 1.4 The petroleum system

One of the goal of this work is to understand the reservoir potentiality of a sin-sedimentary structures affected by fault-related hydrothermal dolomitization. For this reason, it is necessary to introduce the main building blocks of a petroleum system.

Five main ingredients must be present to let a petroleum play work:

1. a reservoir made up of one or several rock formations enough porous and permeable to store hydrocarbon
2. a petroleum charge system formed by a thermally mature source rock.
3. a regional top seal of low permeable rocks preventing the hydrocarbon to flow from the reservoir to the surface
4. petroleum traps focusing the hydrocarbon in specific locations
5. the timely relationship between the four ingredients above (it is essential that the migration of hydrocarbons from the source rock take place after the formation of the seal, the reservoir, and the traps).

If one of the above ingredient is lacking, the petroleum play cannot exist (Allen and Allen, 2013).

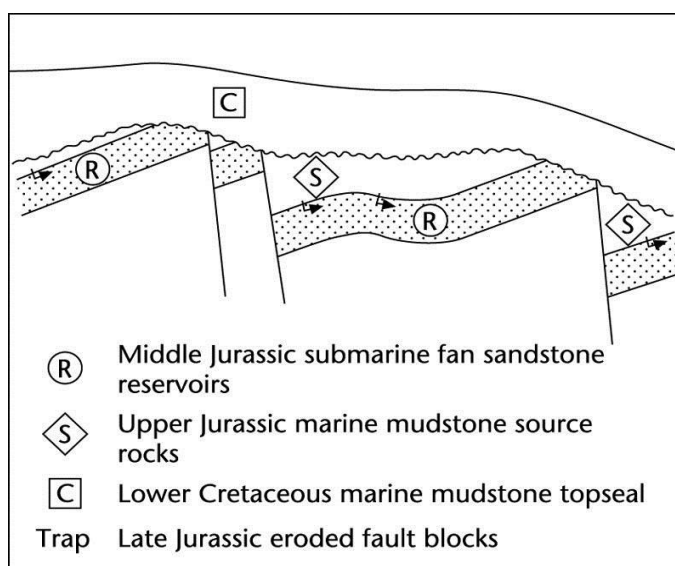


Fig.9: The main characteristic of a petroleum play (Allen and Allen, 2005).

In this work, we focused our attention on the potential properties of the reservoir and traps represented by our study area.

A trap is an obstacle in the subsurface that prevents the migration of the hydrocarbons toward the surface allowing their accumulation. Traps can be subdivided into four main groups: structural, stratigraphic, hydrodynamic and intrusive.

In the analyzed area, only two types of possible traps can be found: the structural ones, mainly represented by the Jurassic extensional fault geometries and the stratigraphic ones represented by the dolomitized body enclosed within low porous and permeable formations.

Structural traps can be formed both in extensional and compressional tectonic setting.

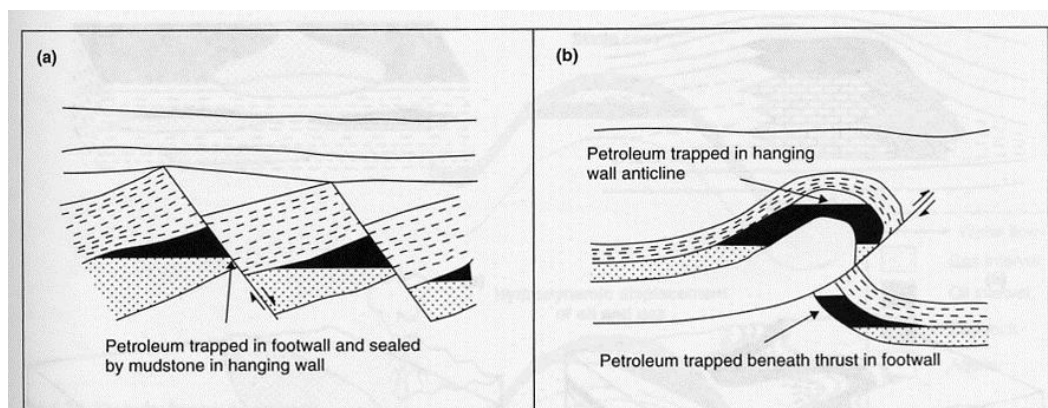


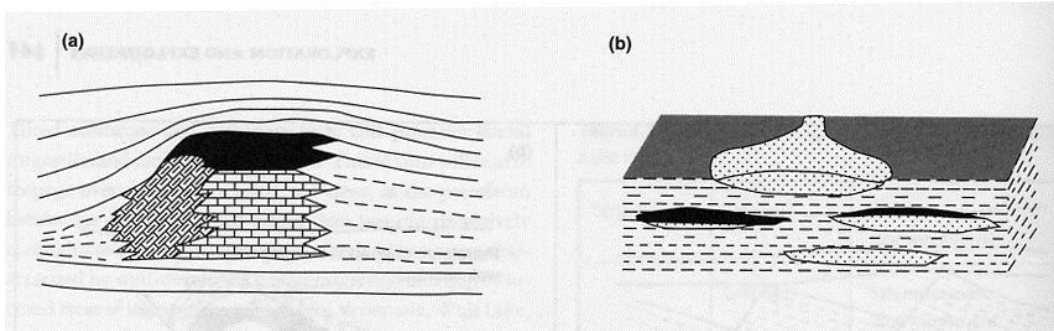
Fig. 10: An example of extensional (a) and compressional (b) traps. (Gluyas JG and Swarbrick RE, 2003).

The main compressional traps are represented by contractional folds and thrusts (fig.10), (e.g. Zagros field, Iran; El Furial, Venezuela). (Allen and Allen, 2013), whereas the more important extensional traps are rollover anticlines (eg. Vicksburg flexure, South Texas) and tilted fault blocks (fig.10), (e.g. Staffjord Field, Nort Sea).

Other structural traps are gravitational structures, gravity driven foldbelts, compactional structures and diapiric traps.

The stratigraphic traps (fig.11) are caused by variation on rock formations in a

stratigraphic sequence (Allen and Allen, 2013). The main stratigraphic traps are depositional traps (e.g. fluvial channel, submarine fans and reef), unconformity traps (e.g. supra-unconformity traps) and diagenetic traps like porous dolomitic bodies within low porous rock formations.



*Fig. 11: Reef (a) and pinchout (b) traps. Both are stratigraphic traps (Gluyas JG and Swarbrick RE, 2003.)*

The porosity of a reservoir must be high enough to contain an economical amount of petroleum within the trap. Besides the interconnection between pores is equally important since a low interconnection means low permeability, which prevent the oil to flow from the reservoir to the wellbore making difficult the hydrocarbon extraction.

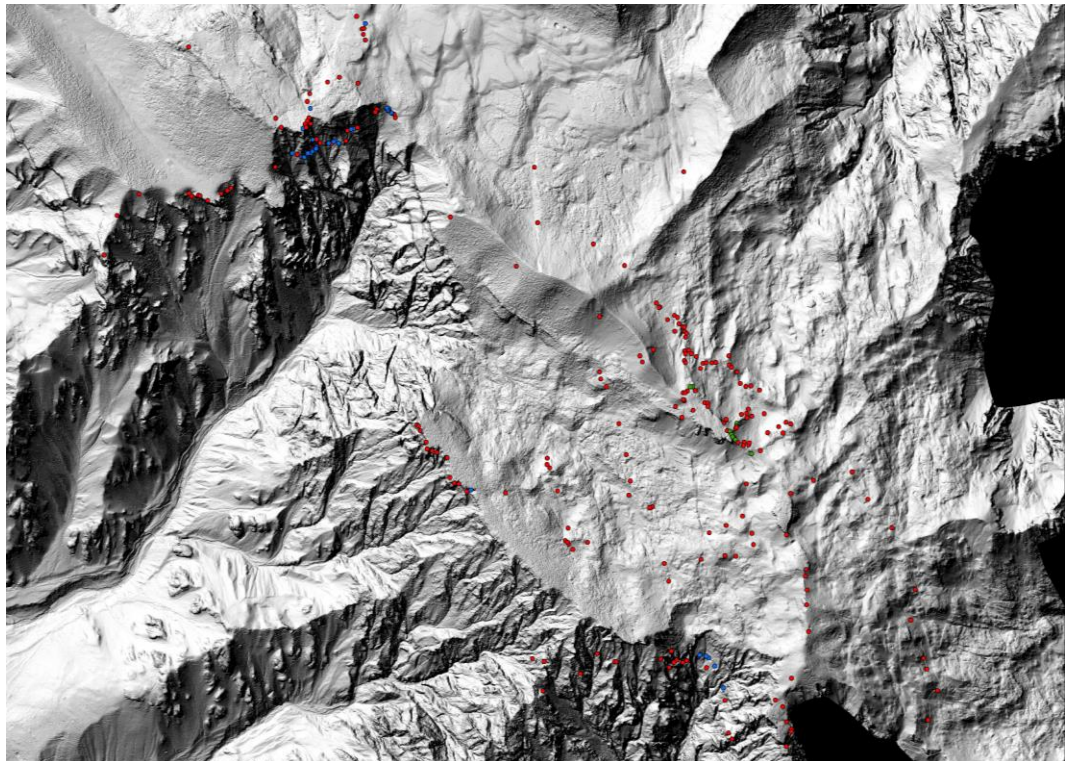
In conclusion, many factors difficult to predict, are in play during the formation of a hydrocarbon reservoir. With this work, we will try to understand if sin-sedimentary structures associated with fault-related hydrothermal dolomites can form important hydrocarbon reservoir. To achieve this goal an intensive field work and a 3D modeling of an exhumed analogue of these structures have been realized.



## 2. Geological map and structural analysis

The geological map was realized using the 1:25.000 topographic map of the IGM (Istituto Geografico Militare) during the field work, whereas the final digitalization with ArcGis was carried out on DTMs obtained from the airborne Lidar of the Provincia Autonoma di Trento.

During the field work, 270 GPS points were taken using a Garmin etrex GPS (fig.12): 10 points mark the place where rock samples for porosity analysis were collected, 35 define the shape of fault related dolomitized bodies and other 245 are associated with strata azimuths and dips and fault data used for the structural analysis and stress inversion (i.e. fault plane orientations, slickensides pitches and attitudes of secondary and conjugate fractures).



*Fig.12: The DTM of the Provincia Autonoma di Trento with the collected GPS points. In blue the structural data, in green the porosity samples and in red all the others (attitudes of rock formations and dolomitized bodies).*

## 2.1 Description of the geological map

The outcropping units are the Dolomia Principale, Monte Zugna Formation, Loppio Oolitic Limestones and Rotzo Formation. Due to the fact that the boundary between Dolomia Principale and Monte Zugna Formation is difficult to recognize, and exposed on steep and unreachable cliffs, I have given a constant thickness of 200 meters to the Monte Zugna Formation and I didn't map the Dolomia Principale Formation which is out of the goal of the present study.

The Loppio Formation has a constant thickness of 30 meters in the whole area. On the contrary the Rotzo Formation presents spectacular evidence of synsedimentary extensional tectonic as testified by the abruptly change of thickness of the formation across the main structure of the Monte Testa.

As far as structure are concerned, the geological map shows three fault systems crosscutting the Dolomia Principale Formation and the Calcari Grigi group with NW-SE, NNW-SSE and NE-SW trends respectively.

Among them 15 main faults were recognized (fig.13 and tab.1) and the higher throws seem to be recorded along the NW-SE trends.

The main NW-SE fault (fault n. 1) extends all over the study area and, together with faults 2, 3 and 4 of the same trend, defines the main tectonic structure of the Monte Testa (fig.15). This structure is in any case part of a larger synsedimentary geometry bounded by the fault 1 to the NE and its antithetic fault number 6 to the SE.

The activity of these faults caused the tilting of the Loppio formation, which does not show evidences of synsedimentary tectonic. This suggest that the faults were not active during the deposition of this Formation that should have been already partially or totally cemented and brittle deformed at the time of the Jurassic tectonic activity.

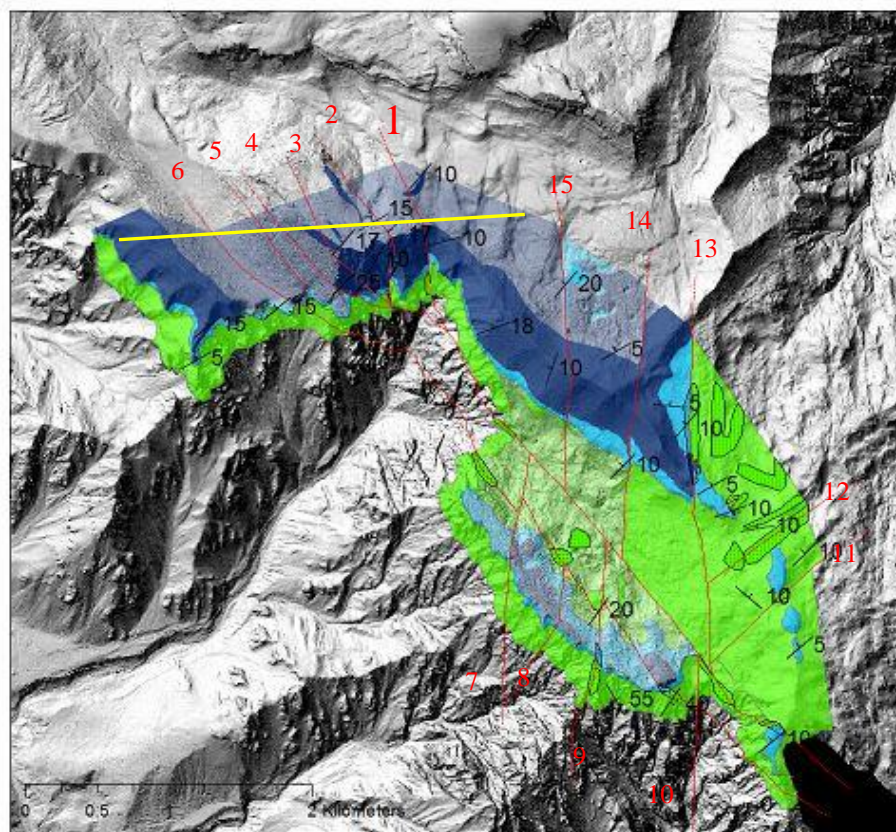
On the other hand, the Rotzo Formation shows spectacular evidence of synsedimentary deformation. Across faults 1 and 4 the thickness of the Formation abruptly increases creating spectacular onlap contacts with the Monte Zugna and Loppio Formations. Moreover, the dip of the Rotzo Formation decrease going



from the lower to the upper part of the formation until the strata became horizontal and is not possible to see any deformation (fig.15). This suggests that the activity of the fault ceased during the deposition of the upper part of the Rotzo Formation where the Jurassic faults were sealed.

A large fold also affects the whole area, with a NE-SW axes as testified by the increase of the dip going from SE to NW.

A structure like the Testo one, where carbonate tilted blocks (in this case the Loppio Formation) are covered by a formation sealing the fault systems (Rotzo Formation) can represent a very good hydrocarbon trap if the porosity of the tilted formation is high enough and the permeability of the sealing one is particularly low.



*Fig. 13: The 1:25.000 geological map of Monte Testa with the number of the faults.  
The yellow line is the cross section of fig.14.*

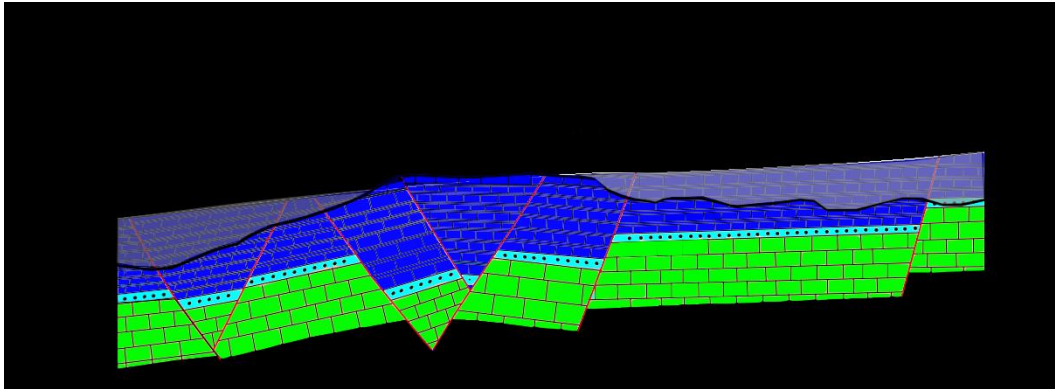
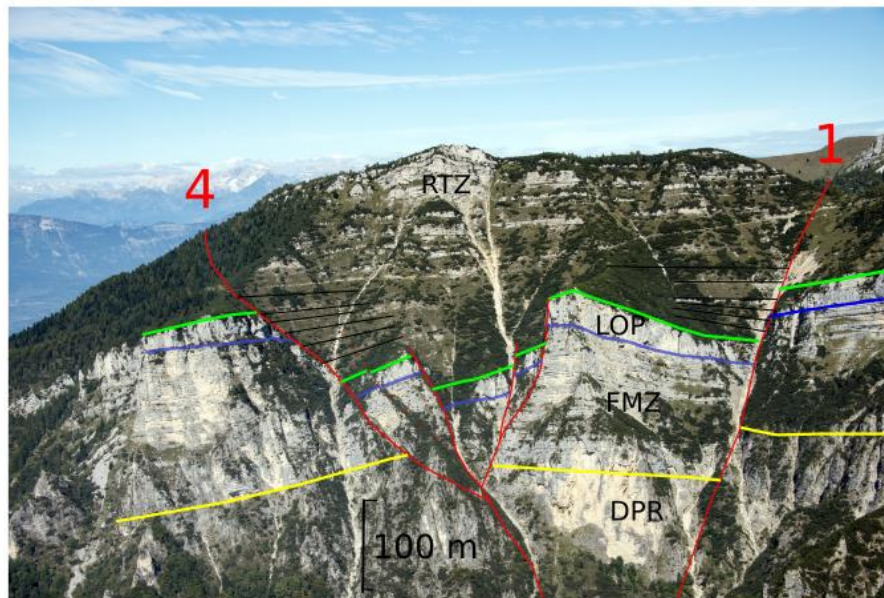


Fig. 14: The cross section of fig. 13. Monte Zugna in green, Loppio in light blue and Rotzo in blue. The red line are the faults. In black the topographic line and the geological interpretation covered by the grey polygon.

Table 1: Dip and directions of the main faults		
Fault	Dip direction	Dip
1	225	70
2	225	60
3	45	60
4	45	60
5	230	65
6	45	65
7	100	80
8	275	70
9	275	70
10	270	85
11	135	85
12	140	85
13	270	75
14	275	70
15	270	75



*Fig.15: The main structure of the Monte Testa.*

A particular attention was also paid in mapping the dolomitized bodies associated with fault and fractures, which were formed during the second event of dolomitization and affected the whole Calcarei Grigi group (e.g. DiCuia et al. 2011; Ronchi et al. 2012). These bodies are marked on the geological map with a dot pattern and have an almost constant width of 30-40 m across faults transecting the Monte Zugna Formation. This thickness abruptly decreases once the Loppio Formation is reached and only along some faults the dolomitization reaches the most lower part of the Rotzo Formation. In plan view, the dolomitized bodies seem to follow the fault without evident interruptions. It is noteworthy that all the three fault systems (NW-SE; NNW-SSE; NE-SW) are affected by dolomitization but not all the faults are associated to dolomitized bodies. This is probably due to the fact that a certain number of faults of the area were not enough permeable to allow the circulation of the dolomitizing fluids.

## 2.2 Structural Analysis

During the field work numerous structural data were collected. In particular, 36 fault planes were identified and for each of them azimuth, dip and, when possible kinematic indicators (slickenside and T fractures) were collected. These information permits to understand the fault orientation and their sense of movement as well as to obtain the paleostress ellipsoid with the use of an inversion method.

On each fault mirror, I looked for kinematic indicators such as “slickensides” which allow to retrieve the sense of movement. In addition to frictional striations, other kinematic indicators have been found such as secondary fractures with a close relationship with the main fault.

These fractures are classified according to their orientation with respect to the main fault (Fossen, 2010).

**T-fracture:** Extensional fracture, often open or filled by carbonates minerals. They don't show striations and they have an orientation of  $45^\circ$  with respect to the main fault.

**P-fracture:** Shear fractures forming a low angle ( $10^\circ$ ) with respect to the main fault. The sense of movement is synthetic with the main fault.

**R-fracture:** Low angle shear fractures with an orientation of  $15^\circ$  with respect to the main fault and a sense of movement synthetic with the main fault. They are the most common among the secondary fractures.

**R'-fracture:** Antithetic with respect to the main fault and R fracture. They have a high angle ( $75^\circ$ ) with respect to the main fault.

Other important kinematic indicators are ridges or grooves that forms when a hard object (rock fragment or mineral grain) on one side of the fault is pushed against the other side by the movement of the fault.

In the area of the study only T-fractures and R' conjugate faults were recognized.

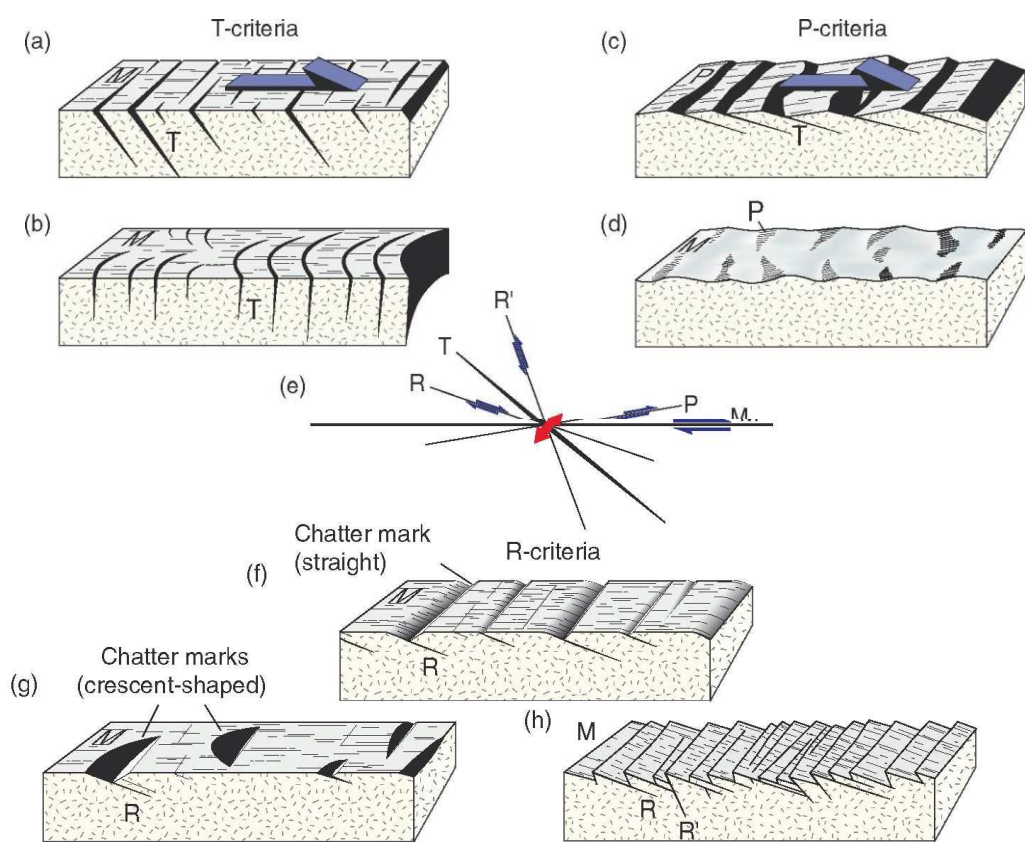
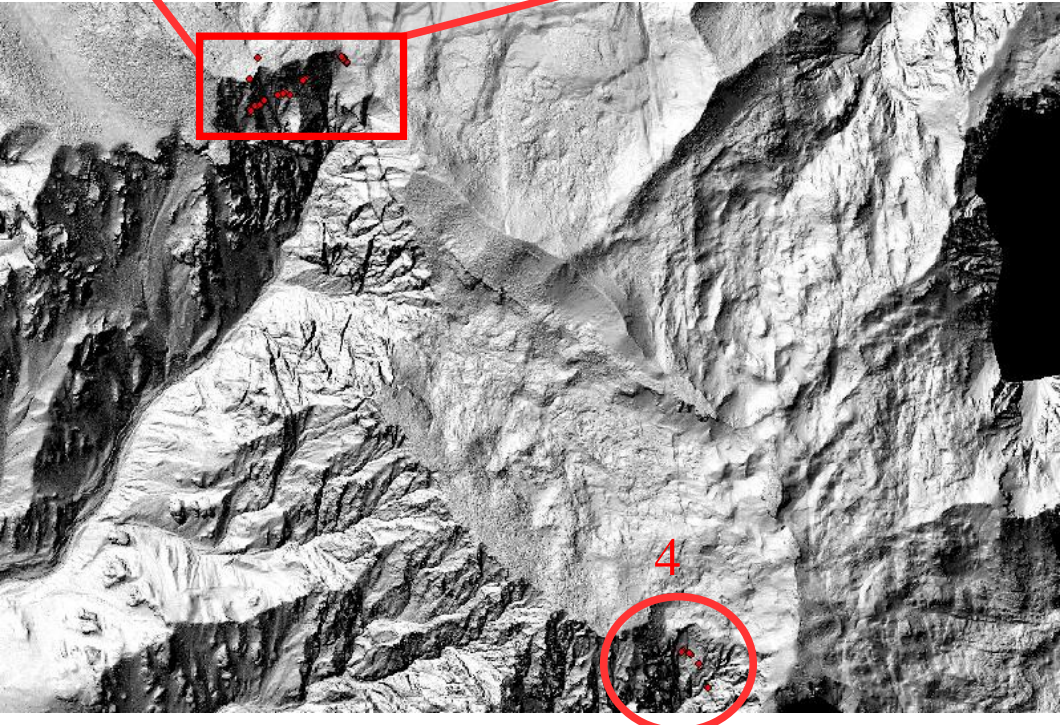
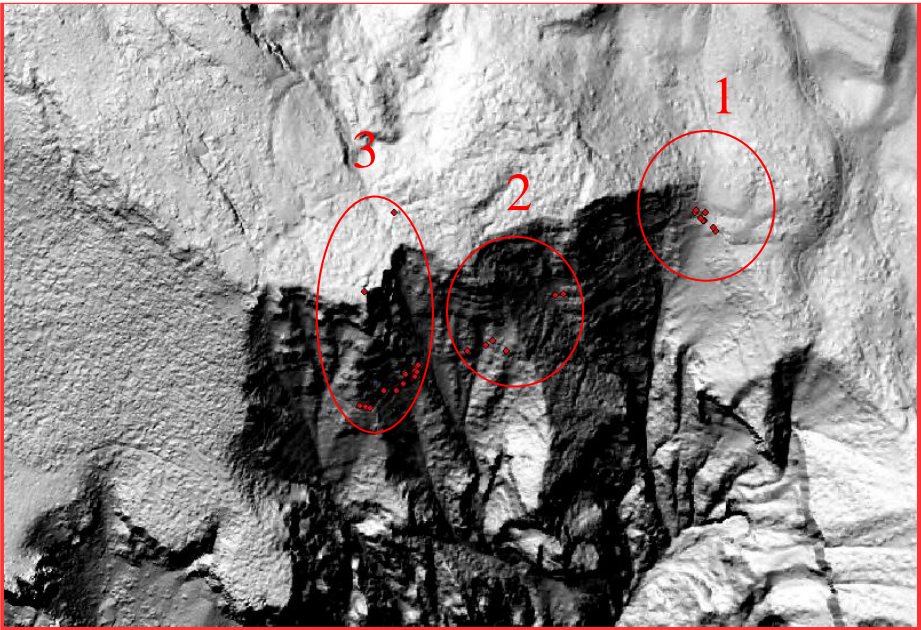


Fig. 16: Kinematic criteria for the determination of the sense of shear of a dextral strike slip fault using secondary fractures (Fossen, 2010)



The 36 structural stops related to fault planes were subdivided into four groups.



*Fig. 17: The location of the four station where the kinematic data were collected*

according to their location and the Jurassic faults have been separated from the Alpine ones (Table 2).

In the following table, the collected structural data are reported.

STOP 1		ALPINE			JURASSIC		
GPS Lat: Long:	Number	Dip-dir	Dip	Pitch and kinematics	Dip-dir	Dip	Pitch and kinematics
+45.8191000 +11.1456800	138	238 110	85 90	ONW txd T fracture			
+45.8193500 +11.1454800	139	110	90	ON txs			
+45.8193500 +11.1452800	140	110	90	ON txs			
+45.8192500 +11.1454300	160	290 270 50	85 85 85	T fracture T fracture txd			
+45.8192800 +11.1454000	161	270	85	txs			
+45.8193900 +11.1453000	162	280	90	vein			
+45.8191500 +11.1456300	158				240	65	60S
+45.8192500 +11.1454500	159	260	85	Txs ??			

STOP 2		ALPINE			JURASSIC		
GPS Lat: Long:	Number	Dip-dir	Dip	Pitch and kinematic	Dip-dir	Dip	Pitch
+45.8183100 +11.1426900	163	70	65	15N	70	65	60S
+45.8183000 +11.1425200	164	300 154	73 70	0-180 vein			
+45.8175700 +11.1415400	141	232	90				
+45.8177200 +11.1412800	142	110 240	80 90	Txs txd			
+45.8176600 +11.1411400	143	342	65	65W			
+45.8175900 +11.1407800	144	240	90	txd			

STOP 3		ALPINE			JURASSIC		
GPS Lat: Long:	Number	Dip-dir	Dip	Pitch and kinematic	Dip-dir	Dip	Pitch
+45.8174200 +11.1398100	165	220 220 220	60 65 65	180N txd 180N txd 180N txd	220	60	45S
+45.8173700 +11.1397800	145	230	80	180N txd	230	80	30 (roof)
+45.8173400 +11.1397500	166				230	70	25 (roof)
					88	12	vein



+45.8173200 +11.1397900	173				30	50	50
+45.817280+11.139 76000	146	220	85	txd			
+45.8172600 +11.1397500	172				230 216	50 85	Normal T fracture
+45.8171700 +11.1395100	171				40	65	40 (roof)
+45.8170800 +11.1393900	147	210 124	80 80	Txd T fracture			
+45.8170900 +11.1391400	170	180 340 325	87 80 85	180W txd 0 txs T fracture			
+45.8168900 +11.1386600	167				280 260 230 80 260	60 80 70 280 70	Normal 80S veins
+45.8168800 +11.1387800	168	220	85	180N txd			
+45.8168600 +11.1388600	169	310 270 270 320 280 118 280 312	80 80 80 80 85 89 90 80	0 txs T fracture T fracture 0 txs T fracture 0 T fracture 7 (roof)			

+45.8173000 +11.1395700	56				50 220 55	75 58 80	normal
+45.8194700 +11.1394300	26	295	90	20 NE improbable			
+45.8184200 +11.1388100	31	220	90	20N txd			

STOP 4		ALPINE			JURASSIC		
GPS Lat: Long:	Number	Dip-dir	Dip	Pitch and kinematic	Dip-dir	Dip	Pitch
+45.7877900 +11.1699700	180	280	87				
+45.7894100 +11.1688700	182	230	55				
+45.7895200 +11.1687200	183				240	55	60S
+45.7896300 +11.1682800	184	115	85	0N txs	115	85	50N
+45.7896000 +11.1682200	185				250	65	
+45.7889800 +11.1693400	186				290 300	85 85	120 (roof) 130 (roof)

The kinematic indicator suggest that this area underwent two main tectonic phases. One characterized by a transtensive tectonic and the other by a strike slip

movement. The first can be attributed to the Jurassic rifting as testified by the synsedimentary extensional tectonic evidence found in the Rotzo Formation. It is worth to note that all the three fault systems show evidence of transtensive tectonic. This suggests that all the systems acted together during the Jurassic. This tectonic event caused the tilting of the Monte Zugna and Loppio Formation creating structural geometries equivalent to the classical hydrocarbon traps.

The second tectonic event that affected the study area brought to the strike slip reactivation of the Jurassic faults and can be related to the Alpine tectonic. In particular faults striking NW-SE were reactivated with a dextral strike slip and the NNW-SSE (N-S) ones with a sinistral slip.

The Alpine compression is also testified by a very large fold with a NE-SW axis that affected the whole sedimentary sequence exposed in the area of the study.

The reactivation of the faults during the Alpine event allowed the circulation of the fluid responsible of the genesis of dolomitized bodies found within the fault zones. A similar process has been documented by Di Cuia et al.,(2011) and Ronchi et al. (2012) in the Asiago Plateau and Monte Grappa.



*Fig. 18: Transtensive kinematic indicators*



*Fig. 19: Transtensive kinematic indicators*





*Fig. 20: T fracture filled by calcite*



*Fig. 21: sinistral strike slip kinematic indicators*

### 2.2.1 Paleostress calculation and inversion methods

The calculation of the paleostress starting from the fault slip data (strike and dip of fault plane, sense of movement and orientation of the kinematic indicators) is generally based on several assumptions.

1. slip takes place in the direction parallel of the maximum resolved shear stress on the plane of movement
2. the stress field must be homogenous
3. the movement of one fault doesn't influence the movement of the other faults

The inversion of fault slip data allows to derive the parameters of the reduced stress tensor. The axes of principal stress  $\sigma_1$  (maximum compression),  $\sigma_2$  (intermediate compression) and  $\sigma_3$  (minimum compression) and the stress ratio  $R$ .  $R = (\sigma_2 - \sigma_3)/(\sigma_1 - \sigma_3)$ .  $R$  has a value that goes from 0 to 1.

There are a lot of methods and computer programs that allows to reconstruct the stress tensor. The direct methods use the least square minimization whereas the iterative methods or grid search methods test a wide range of possible tensor (Etchecopar *et al.* 1981, Delavaux and Sperner, 2003).

The most important and used direct inversion method is the Right Dihedron.

This method permits to determine the range of feasible orientations for the principal stress axes even when the orientations of all the three axes are unknown. In this method, for each fault another plane perpendicular to the fault plane and slip lineation is defined. In this way, the stereographic projection can be divided into two pairs of quadrants. Knowing the sense of slip of the fault is possible to understand which pair of quadrant is tensional (containing  $\sigma_1$  axis) and which is compressional (containing  $\sigma_3$  axis).  $\sigma_2$  axis is orthogonal to the other two axes. This procedure is repeated for all fault slip data. The counting values of a single fault is called “characteristic counting net” while the resulting average of the values of a data subset forms the “average counting net for this subset” (Delvaux and Sperner, 2003).

### ***2.2.1.1 Wintensor***

Wintensor developed by Delvaux in 1993 is the computer program used in this work for paleostress calculation.

The program introduces two main innovation: an improvement of the classic Right Dihedron method and an interative inversion method called “Rotational Optimization method”.

The improved Right Dihedron method allows, to calculate the stress ratio R, the use of secondary fractures together with slickenside data and an initial separation of the data to be performed on the basis of the Counting Deviation, which is a parameter used for estimating the degree of compatibility of the individual counting nets with the average counting net of the subset (Delavaux and Sperner, 2003).

For each regime extensional, compressional and strike slip, the value of R goes from 0 to 1 and when the value of R is near 0,5 the stress regime is said pure (Delvaux and Sperner, 2003). However, the distinction of the correct stress regime is not covered by the R value. For example an extensional regime with R=1 is equivalent to a strike slip regime with R=1.

For this reason in Wintensor another value called stress regime index or R' was defined. The relation between R and R' are the following:

1.  $R'=R$  when  $\sigma_1$  is vertical (extensional stress regime)
2.  $R'= 2 - R$  when  $\sigma_2$  is vertical (strike slip stress regime)
3.  $R'= 2 + R$  when  $\sigma_3$  is vertical (compressional regime)

The R' value goes from 0 to 3 such as values of 0,5 are for pure extension, 1.0 for extensional strike slip, 1.5 for pure strike slip, 2.0 for compressional strike slip and 2.5 for pure compression.

For all types of stress tensor when  $\sigma_1 > \sigma_2 > \sigma_3$  and  $0,25 < R < 0,75$ , the Improved Right Dihedron method successfully estimates the four parameters of the stress tensor ( $\sigma_1$ ,  $\sigma_2$ ,  $\sigma_3$  and R) (Delavaux and Sperner, 2003).

Another important improvement of Wintensor to the classic Right Dihedron method is the possibility to estimate the degree of compatibility of the individual

counting net with the average counting net through the calculation of a Counting Deviation for each datum. This consists in a preliminary check of the fault data allowing the rejection of bad data.

The preliminary stress tensor and the fault data selected using the Improved Right Dihedron method can be used as starting point for the iterative inversion procedure called that Rotational Optimization method in WinTensor (Delvaux and Sperner, 2003).

This method is based on testing a great number of different stress tensors in order to minimize the inversion error through a minimizing function with the following form:

$$F_j = \frac{\sum(f_j(i) \times w(i))}{n \times \sum w(i)}$$

where  $w(i)$  is the weight of the individual data,  $n$  is the number of data and  $f_j(i)$  is the function that has to be minimized which depends from the available structural data (Delvaux and Sperner, 2003).

The determination of the stress tensor using the Rotational Optimization procedure is a controlled 4D grid search. This procedure involving successive rotation of the tensor around the three principal stress axes ( $\sigma_1$ ,  $\sigma_2$ ,  $\sigma_3$ ) and equivalent testing of the stress ratio  $R$ . For each stress axis, the rotation angle is determined for which the misfit function has its minimum value (Delvaux and Sperner 2003). In this way four graphics are obtained (3 for the stress axis and one for  $R$ ) with the rotation angle in x axes and the value of the misfit function in y axes. The minimum value of the misfit function is determined by taking the minimum of the obtained regression curves.

The value  $R'$  is tested using the same process.

The process of rotation of the axes and determination of  $R$  is repeated several times until the tensor is stabilized (Delvaux and Sperner, 2003).



For a good result in the calculation of the stress tensor a check of the data before the starting of the optimization process is necessary. Therefore, the program automatically separated the data into population each being characterized by a unique stress tensor. An initial maximum slip deviation  $\alpha$  of  $30^\circ$  is set as upper limit for defining whether a fault slip datum is compatible to a stress tensor (Delvaux and Sperner, 2003). For a better fault separation, the procedure is executed successively with a decreasing value of the maximum slip deviation. However, it is necessary to say that this process is based on the assumption of an andersonian fault behavior.

### ***2.2.1.2 Result of stress inversion***

For the reconstruction of the Jurassic Paleostress we collected all the data of the stations number 1, 2 and 3 in a single stereoplot. Whereas station number 4 was plotted separately. This operation was done in order to have enough statistics for the application of the Rotational Optimisation method.

For the Alpine tectonics stations number 1 and 2 were plotted together and separately with respect to station number 3. Unfortunately, good alpine phase indicators were not found in station number 4.

#### *2.2.1.2.1 Jurassic Paleostress*

##### Station 1, 2 and 3

The Paleostress reconstruction for these stations was done using the Right Dihedron method followed by the Rotational Optimisation method. The latter was applied in order to calculate the regression curves for the stability of the stress axes. The results show a NE-SW extension as testified by the value of  $R = R' = 0,13$ . The orientation of the stress axes are:  $\sigma_1 = 54/162$ ,  $\sigma_2 = 31/309$ ,  $\sigma_3 = 16/049$ . Rotation around  $\sigma_2$  and  $\sigma_3$  has a good stability whereas rotation around  $\sigma_1$  has a bad stability as testified by the regression curves of fig.18.

This means an oblate strain ellipsoid with a vertical  $\sigma_1$ .

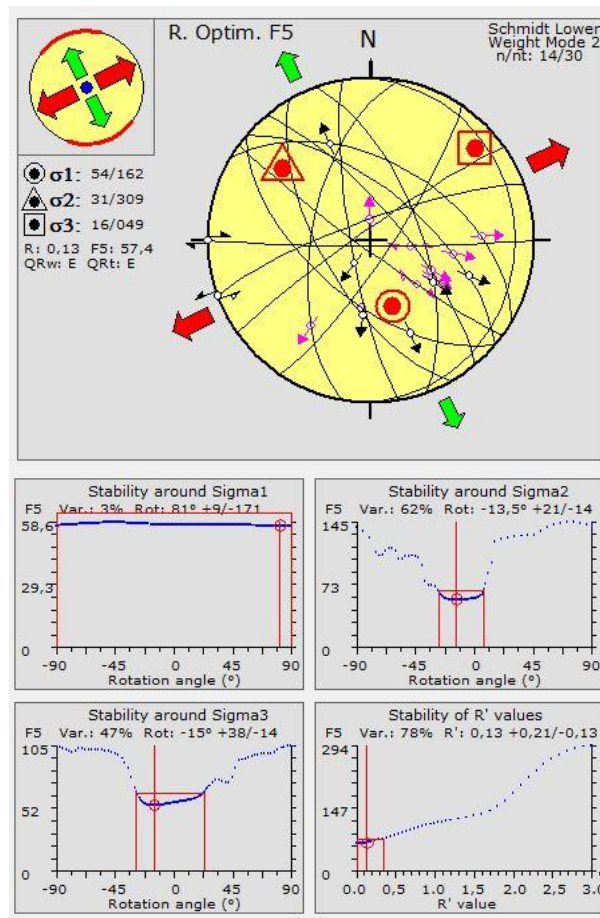


Fig. 22: Above: Results from the Rotational optimization method for station 1, 2 and 3. The black lines represent the fault planes, the black arrow is the sense of shear and the pink is the resolved shear. The red arrows represent  $\sigma_3$  and the green is  $\sigma_2$ . Below: Stability of the stress axes and of R'.

#### Station number 4

The same process adopted for stations number 1, 2, 3 was applied for the station number 4. The orientations of the three stress axes are  $\sigma_1=74/18$ ,  $\sigma_2= 14/341$ ,  $\sigma_3= 08/249$ . The value or  $R=R'$  suggests a NE-SW extensional regime.

The stability around  $\sigma_1$  is very low on the contrary  $\sigma_2$  and  $\sigma_3$  axes that have a good rotational stability. This again means an oblate strain ellipsoid with a vertical  $\sigma_1$ .

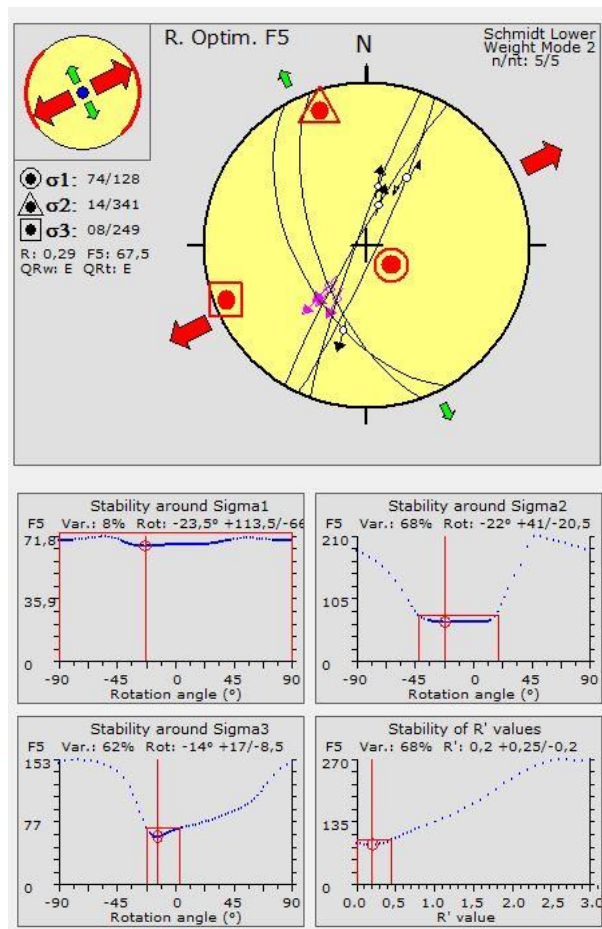


Fig. 23: Above: Results from the Rotational optimization method for station 4..  
 Below: Stability of the stress axes and of R'.

Hence, both reconstructions suggest a general oblate strain with a NE-SW main extension during the Jurassic. This result, is in contrast with the classic interpretation of the Jurassic tectonics foreseeing an andersonian E-W extension ruled by N-S fault systems (Bosellini, 1973; Castellarin, 1972; Castellarin and Picotti, 1990), but agrees with the study of Franceschi et al. 2014 which suggests an orthorhombic set of faults (NNW-SSE and ENE-WSW direction) on the entire Trento Platform during the early Jurassic in response of a regional oblate strain ellipsoid.

### 2.2.1.2.2 Alpine Paleostress

#### Station 1 and 2

This set of data was analyzed using the right Dihedron method and the Rotational Optimisation method. The stress axes trend are  $\sigma_1=05/005$ ,  $\sigma_2= 83/227$ ,  $\sigma_3= 05/096$ . The three stress axes have a good stability and the values of  $R'=0,65$  and  $R=1,95$  suggest a compressional strike-slip regime dominated by a N-S contraction during the Alpine tectonic event.

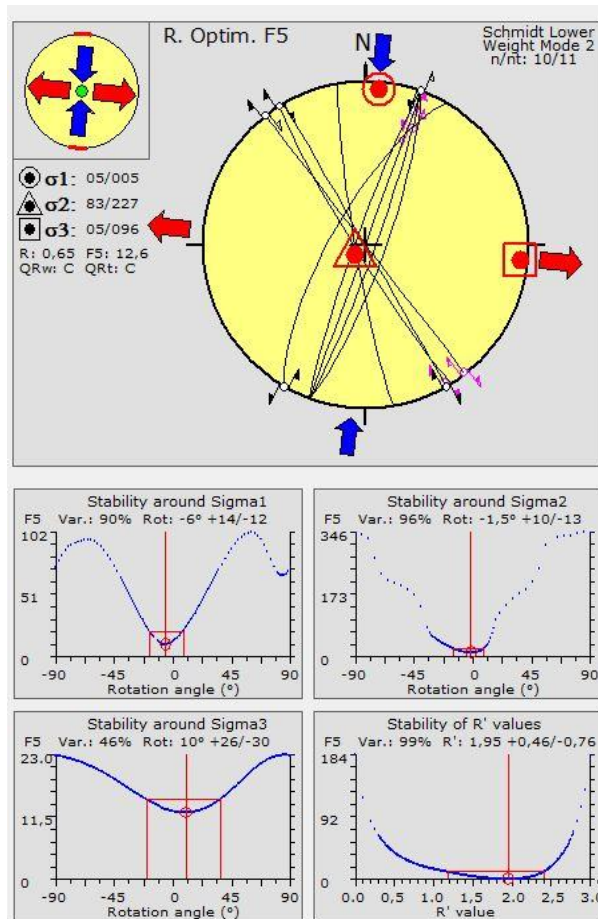


Fig. 24: Above: Results from the Rotational optimization method for station 1 and 2. Blue arrows represent  $\sigma_1$  and red arrows are  $\sigma_3$   
Below: Stability of the stress axes and of  $R'$ .

### Station 3

Station number 3 is characterized by  $\sigma_1=07/004$ ,  $\sigma_2=79/231$ ,  $\sigma_3=08/095$ ,  $R=0,64$ ,  $R'=1,24$  and a good stability of the three axes. The result is very similar to station number 1, 2 suggesting again a general N-S compression and a dominant strike-slip regime.

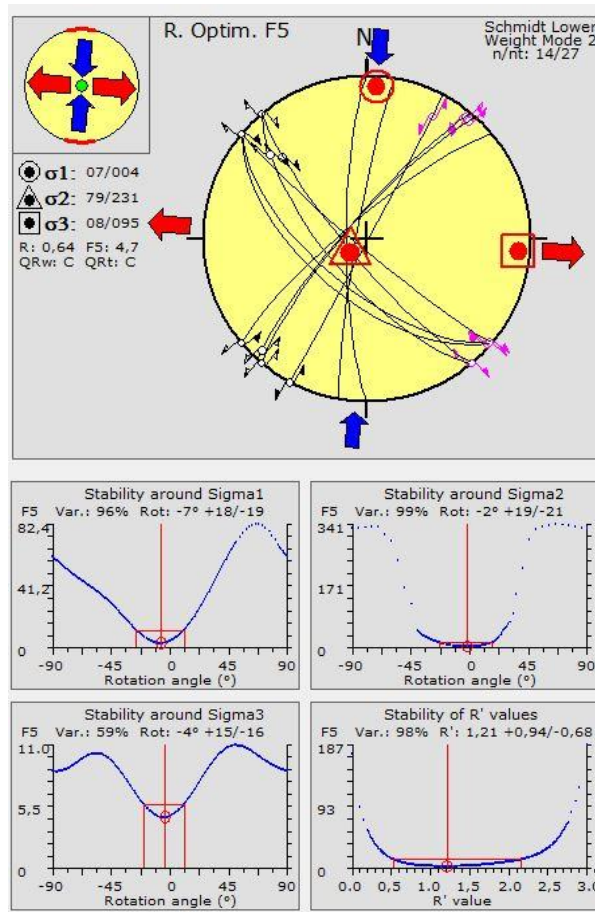


Fig. 25: Above: Results from the Rotational optimization method for station 1,2 and 3.  
Below: Stability of the stress axes and of  $R'$ .

A N-S contraction is in agreement with the classic interpretation of the paleostress acting on the Southern Alps during the Alpine tectonic event (e.g. Castellarin et al. 2010).

## **3. Porosity analysis**

### **3.1 Porosity in reservoir**

Porosity is one of the most important characteristic of a hydrocarbon reservoir and highly differs between carbonate and silicoclastic rocks.

In silicoclastic rocks, the primary porosity is quite predictable because it is mainly intergranular and depends from the grain size, sorting and packing of the sediments. In this type of reservoir, a key role in controlling the evolution of porosity is played by compaction and diagenesis. Compaction reduces the size of the pores and, in some cases, closes them completely. During diagenesis clay cement can have important negative (cement filling the pore spaces) as well as positive (chlorite rims on grains inhibiting later quartz cementation and pressure dissolution) effects (Allen and Allen, 2013). On the other hand, porosity can be increased by dissolution of mineral grains.

In carbonates, the pore system is very complex. This is due to the biological origin of the carbonates which can have their own primary porosity and their chemical reactivity which make them prone to the development of secondary porosity during pervasive diagenetic processes, solution and dolomitization (Moore, 2001).

Mud-free carbonate sediments, at the time of deposition, are dominated by intergranular porosity that varies from 40% to 50 % (Moore, 2001). However, the biological origin of the carbonate grains is responsible other porosity types, the more important being: intragrain porosity, framework and fenestral porosity.

The intragrain or intraparticle porosity can be created by the chamber of various organisms such as foraminifera, gastropods, rudists and brachiopods as well as the ultrastructure of organism skeleton or abiotic grains (Robinson, 1967; Loreau and Purser, 1973; Enos and Sawatsky, 1981; Moore, 2001).

Carbonate sediments bearing mud have a porosity that goes from 44% to 75%. As we can see in figure 26 sediments with a high content of mud have a higher porosity (60%-78%) this is due to the effect of the shape and fabric of the particles.

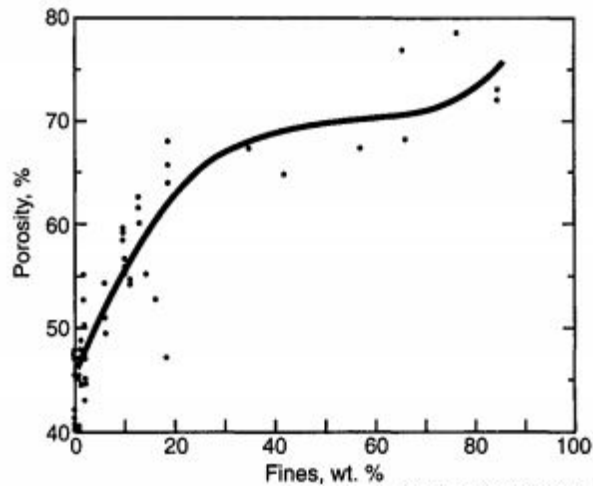


Fig. 26: Variation of porosity in carbonate sediment bearing mud (Enos and Sawatsky, 1981).

On the other hand, permeability in mud-supported carbonate sediments is very low while in grain supported sediment it is very high (Fig. 27) (Enos and Sawatsky, 1981).

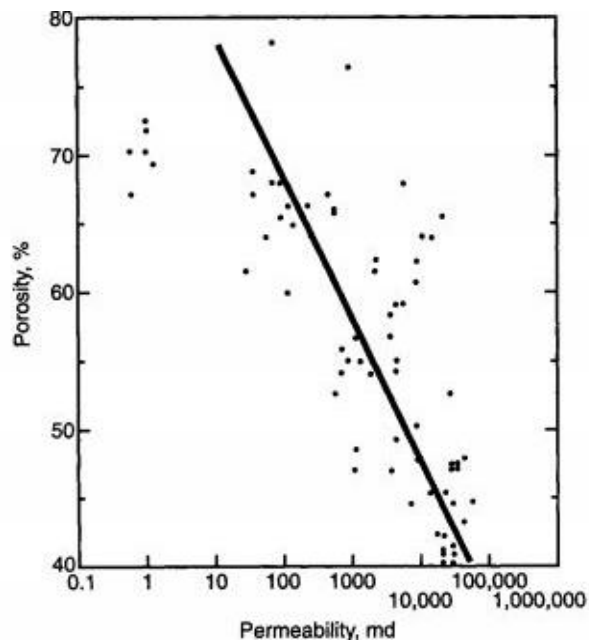


Fig. 27: The relationship between Porosity and permeability in Holocene carbonate sediments (Enos and Sawatsky, 1981).

Framework porosity develops in reef environment for the activity of reef-building organism. The volume of pores depends from the type of the building organism: on one hand coral constructs an open framework reef creating high porosity, on the other hand algae and sponges create a closer framework with a lower porosity. This type of porosity was for long time a main target for the hydrocarbon exploration (Moore, 2001).

Fenestral porosity can have a porosity up to 65% and it can be associated with supratidal, algal-related mud dominated sediments (Shinn, 1968; Tucker and Wright, 1990; Moore, 2001). During burial, diagenetic process tends to close the pores through compaction and precipitation of cements (fig. 28).

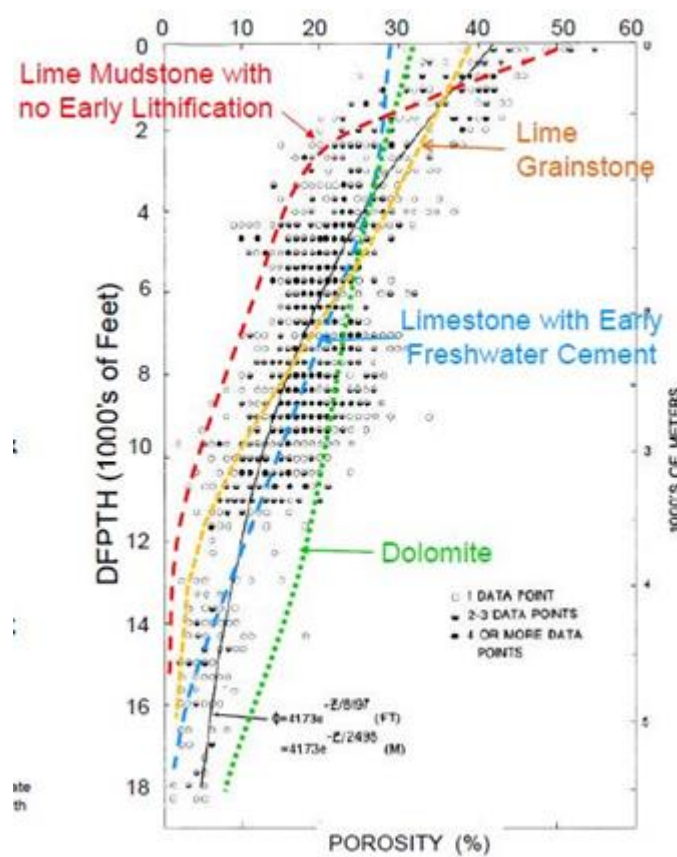


Fig.28: Evolution of porosity during burial in different type of carbonate rocks (Shmocker and Halley, 1982; Saller, 2013).

However there are two diagenetic processes that can improve the porosity during burial: 1) porosity generation by dissolution and 2) porosity and permeability



improvement through dolomitization. Another process is fracturing that increases the permeability rather than the porosity (Moore, 2001).

Dissolution in limestones and sediment occurs when the pore fluid suffers a significant change in its chemistry. Usually it occurs during the first part of the burial history, when a meteoric water system can develop (eogenetic stage). Also hydrocarbon maturation and shale dewatering can lead to formation of aggressive fluids bringing to dissolution after high burial. Important dissolution processes are karst processes that can occur anytime during the burial history when a rock sequence is exhumed and might enter in contact with meteoric waters (Loucks and Handford, 1992); Saller et al. 1994; Moore 2001).

Dolomitisation can improve porosity creating large pores when the CO<sub>3</sub> is sourced from the rock, in addition this process leads to an abrupt increase in permeability or it can lead to cementation if there is a net import of CO<sub>3</sub> with a consequent reduction of porosity (Allen and Allen, 2014).

An interesting work about the relationships between porosity and dolomitisation was realized by Wang et al. 2015. The authors analyzed a case study from the Lower Triassic Feixianguan Formation of the Eastern Sichuan Basin in China. The original grainstone of this formation was affected by micritization, cementation and mechanical compaction before dolomitization. The dolomitization process started at a depth of 760 m. Four stage of dolomitisation were recognized. In stage I (<50% dolomite) porosity slight decrease due to external CO<sub>3</sub> source added. As contents of dolomite increased (from 50% to 90%) during stage II, porosity increases only slightly. This is due to the residual microcrystalline material filling the interstice between the dolomite crystals. This implies that the replacement of limestone by dolomite was not complete due to the insufficient dolomitizing fluids. In stage III, porosity increases significantly due to the dissolution of the remaining calcite. At the end during stage IV dolomite cements precipitated in pores with a decrease in porosity and permeability. Saddle dolomite can be observed in this stage (Wang et al. 2015).

In summary, this work suggests that only few steps during the dolomitization process can create an important improvement of porosity and when these steps are overcome the porosity decreases.

### **3.2 Dolomitization in the Calcarei Grigi group**

According with DiCuia et al. 2011, the Calcarei Grigi group of the Trento Platform underwent two main dolomitization phases: i) an early Mesozoic low temperature and shallow burial event that created an undulatory dolomitized front at the boundary between Dolomia Principale and Monte Zugna Formation and ii) a hydrothermal Oligocene-Early Miocene event that led to formation of fault related dolomitized bodies.

Through petrographical analysis the authors recognized four main facies named from A1 to A4 (fig.30). A1 facies is formed by undolomitized calcareous rocks, fabric preserving dolomites and mixed calcareous-dolomitic facies. A1 is probably related to the early dolomitization event. A2 is characterized by fine to medium unimodal dolostones, with no porosity and an unpreserved original texture. A3 facies shows a developed porosity network with values going from a few per cent up to 15% and saddle dolomite crystals are also reported. A4 presents fine to coarse grained polymodal dolostones with a porosity ranging from 1,5% to 15% and reaching 30% at its maximum. Four generation of cements has been also recognized: three of dolospar (Dc1, Dc2 and Dc3) and one of calcite (Cc4).

Dc1 cement replaced the matrix of the rock and is formed by small dolomite crystal (ca 100um). Dc2 cement filled the pores created by Dc1 dissolution and is typical of A1 and A2 facies. Dc3 fills the secondary porosity and it is considered the latest dolomite generation. Cc4 is a calcite cement forming during the last diagenetic phases; it reduces the residual and secondary porosity filling the remaining pores (DiCuia et al. 2011).






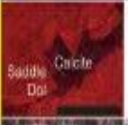


Stages/ timing	Dolomite paragenesis of Calcari Grigi Group			Petrography - Petrophysics				
			Microfacies Association	Thin section/ Cathodoluminescence	Field inclusions of crystal assemblages	Texture	Phi (%)	K (mD)
1 Hettangian Sinemurian	Limestone	Parent limestones $\xrightarrow[\text{Fracturing}]{\text{Dissolution}}$ Mimic (?) Replacement	A1		No data	Mudstone unimodal dolomite	Tight	
2 Lias/ Cenozoic	First dolomitization stage	Dark dolomite nuclei in the matrix $\xrightarrow{\text{Crystal growth}}$ Zoned luminescent dolomite crystals	A1			UNIMODAL	0-1%	Phi/K development $< 10$
3 Oligocene- Miocene	Corrosion and substitution	Dark-blue dolomites accompanying partial corrosion and substitution of previous crystals	A2 A3			POLYMODAL	Intergr. - MUDSTN 0.5-20%	
4 Oligocene- Miocene	Saddle dolomite development	Medium luminescent dolomitic cement filling some fractures. Well developed, strongly luminescent and zoned dolomite rims overgrowing previous crystals	A3 A4		No data		POLYMODAL	Intergr. - MUDSTN 0.5-20%
5 Oligocene- Miocene	Calcite filling macropores	Late-stage dull calcite	A4					$> 10$

Fig.29: Summary of the paragenetic stages, processes and petrophysical properties (Di Cuia et al. 2011).

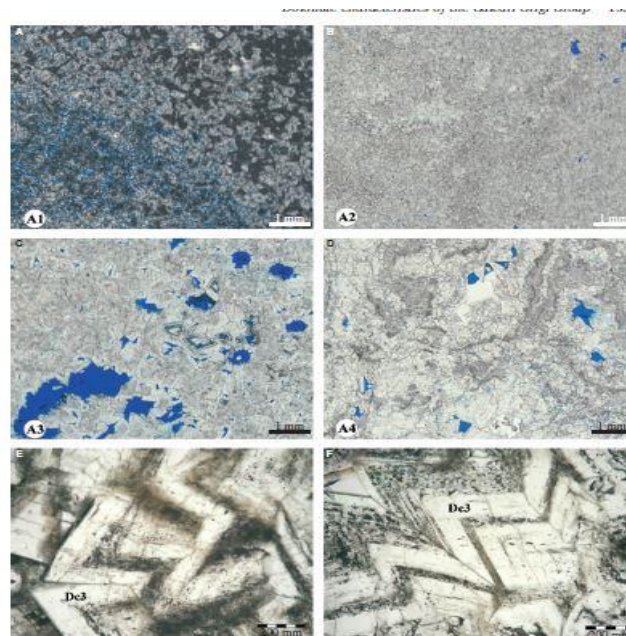


Fig.30: The four main dolomite microfacies of the Calcari Grigi group (Di Cuia et al. 2011).

### **3.3 Image analysis for porosity extraction**

The discrimination of different surface materials in an image is based on their spectral properties. Each material has a particular spectral signature depending on the variation of a material reflectance with the wavelengths. The discrimination between pores and the other part of the samples is made exploiting the color difference between pores (in this work, filled with blue methylene or chromium oxide) and the rest of the sample.

The distinction of different materials can be achieved with two types of classification processes: unsupervised and supervised classifications (Fig.31) (Drury, 1993). The unsupervised classification is used when the operator does not know the possible materials present within the image of interest and it is based on a statistical analysis of the digital numbers (DN) related to the pixels of the image. By contrast, in the supervised classification the operator chooses training areas representing the different spectral classes of interest. In this latter case, the pixels of the training areas are selected and their statistical parameters are used as input data for the classification.

The simplest operator of a supervised classification is the “parallelepiped or box” classification. According to this method, parallelepiped boxes are defined in a  $n$  space where  $n$  are the number of the image bands or channels (the analyzed images of thin sections has three channels: Red, Green and Blue). The limits of the parallelepiped represent the range of DN of the training areas for each considered band. The computer compare the DN of unknown pixels with the values of the reference boxes and when they fall within a given reference box they are assigned to that class, otherwise they remain unclassified (e.g. Drury, 1993).

A more accurate operator is the minimum distance to means classification. This method defines the mean DN for each training area- in each band being used (Drury, 1993). The distances of an unknown pixel from each of these means are calculated and the pixel is assigned to the class with the closest mean. It's possible to define thresholds beyond which the pixel is not assigned to any class.

Finally, another method is the maximum-likelihood classification. Here from training areas, mean pixel position, variance and covariance of each class are calculated. In this way, the shape and position of the cluster that define a given area of a class can be obtained. The obtained cluster can be contoured to show

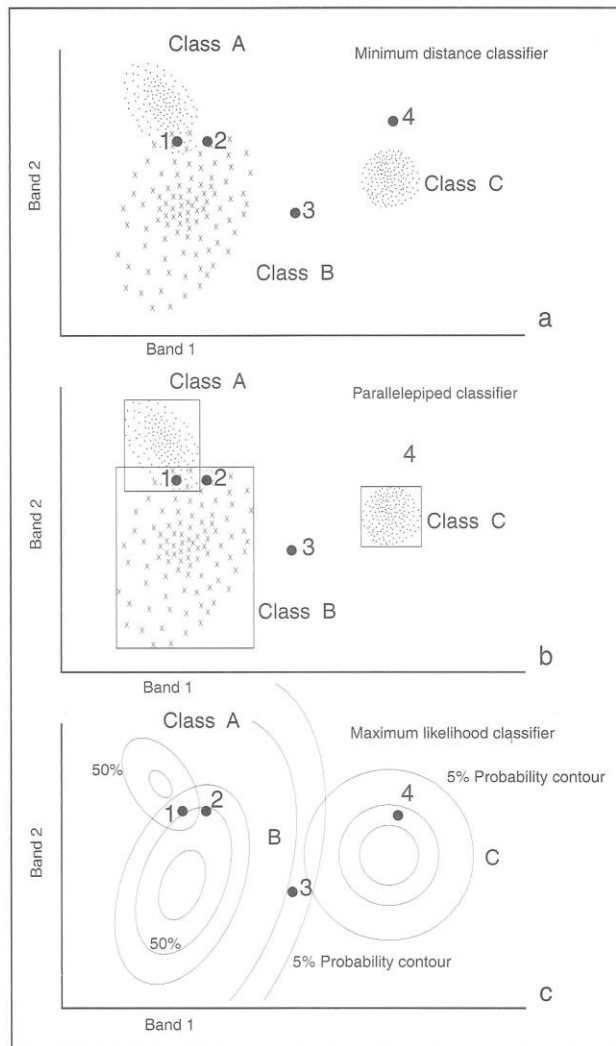


Fig.31: The three main types of supervised classification (P.J. Gibson and C. H. Power, 2000).

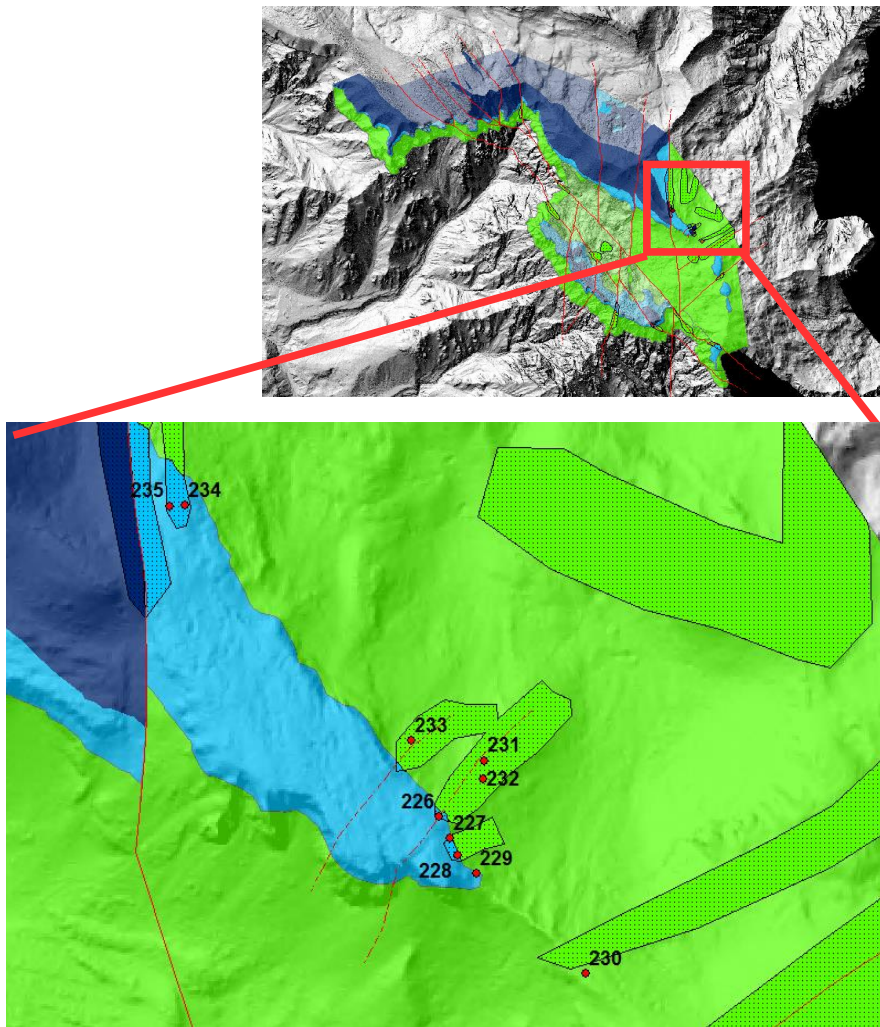
how the probability decreases away from the mean point. The algorithm calculates the probability that a pixel belongs to each of the selected classes and assigns it to the class with the highest probability (Drury, 1993). The user can decide the minimum likelihood value so that a pixel can not be assigned if this value is not reached

A method very similar to the maximum likelihood classification is the Mahalanobis distance in which the variances of the classes are assumed to be equal one to each other.

### 3.4. Porosity analysis of the M.te Testa rocks

#### 3.4.1 Sample collection and preparation

During field work 12 rocks samples were collected for the porosity analysis and numbered from 226 to 237. The dolomitized samples were exclusively collected from the fault related dolomitized bodies of the Loppio and Zugna Formations and not from the dolomitized undulatory front at the boundary between Dolomia Principale and Monte Zugna Formation. 10 thin sections impregnated with blue methylene and 8 cut samples with pores filled by chromium oxide were obtained from these samples, In particular samples number 228 and 231 were cut twice to obtain a better statistic for porosity values (Table 3).



*Fig.32: The geological map with the point where the sample were collected.  
Monte Zugna in green and Loppio in light blue*

The cut sample were prepared by slicing them with a diamond saw and the cut side has been smoothed using silicon carbide with different grids. The pores of the samples were finally filled with the chromium oxide previously micronized.

The thin sections preparation instead required the following steps:

1. The sample is cut with a diamond saw to obtain a slice of a centimeter from where a parallelepiped, called chip, is extracted. (20x30x10mm).
2. The chips is dried in an oven
3. Under vacuum the chip is incorporated in an epoxy resin (araldite 2020) colored with blue methylene
4. The chip is put into an oven at 40°C for one night
5. One side of the chip is smoothed using silicon carbide (grit 600).
6. The chip is dried at 80°C and on the smoothed side is fixed on the carrying slide using an epoxy resin (araldite 2011).
7. The retro-cut of the chip is thinned up to 30 micron using silicon carbide with different grits.
8. As last step the chip is covered with a cover glass and Canadian Balsam

Steps from 2 to 8 were realized by the laboratory of Geoscience Department of University of Padova.

Table 3				
Samples	Thin section	Cut sample	Longitude	Latitude
226 Dolomitized Loppio F.	YES	NO	+11.1710100	+45.8015500
227 Dolomitized Loppio F.	YES	NO	+11.1711200	+45.8013800
228 Dolomitized Loppio F.	NO	2 YES	+11.1712000	+45.8012500
229 Loppio F.	YES	NO	+11.1714100	+45.8011000
230 Monte Zugna F.	YES	NO	+11.1726200	+45.8003100
231 Dolomitized Monte Zugna F.	NO	2 YES	+11.1715400	+45.8019700
232 Dolomitized Monte Zugna F.	YES	NO	+11.1715200	+45.8018300
233 Dolomitized Monte Zugna F.	YES	YES	+11.1707200	+45.8021400
234 Dolomitized Loppio F.	YES	YES	+11.1682200	+45.8040000
235 Dolomitized Loppio F.	YES	YES	+11.1680400	+45.8040000
236 Loppio F.	YES	NO	+11.1565300	+45.8160000
237 Rotzo F	YES	NO	No GPS	No GPS

### ***3.4.2 Image analysis***

The thin section were photographed with a resolution of 72 x 72 dpi, using a Fujifilm XE1 while the cut sample were scanned with a resolution of 3600 x 3600 dpi.

The images were analyzed with ENVI software to obtain porosity maps of each sample. In this way the percentage of porosity for each sample has been calculated.

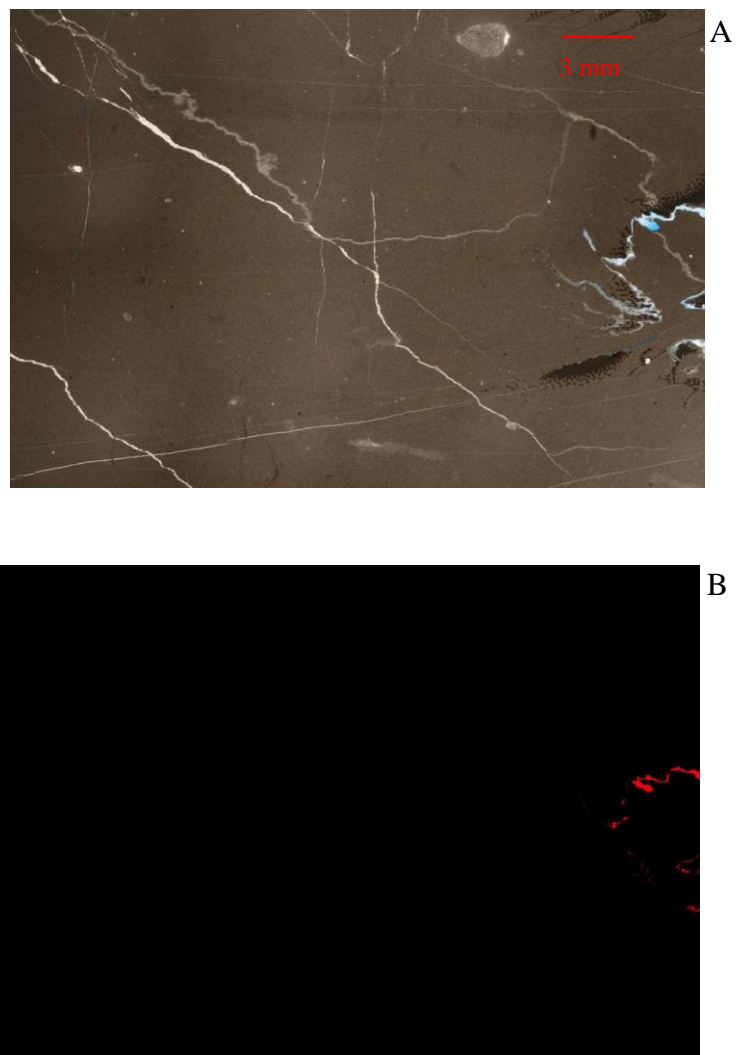
During the scanning of the cut sample, the scanner acquired rectangular images. Being the samples not perfectly rectangular, some parts of the images were with no data and had to be masked. In particular masks were applied on samples 228\_2, 231\_2, 233, 234, 235.



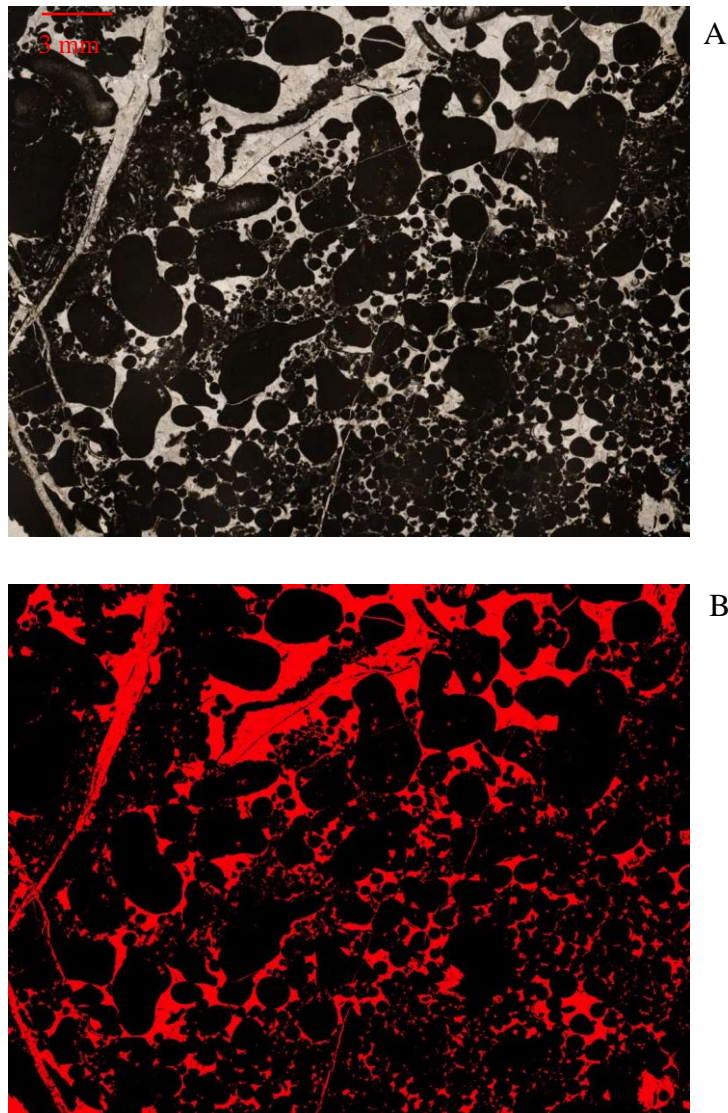
For each samples one (pores) or two classes (pores and rest of the sample) of identification were selected. The Mahalanobis Distance method gave the best results for thin sections, while for cut samples the maximum-likelihood classification was chosen.

At the end through ENVI post processing tool the percentage of porosity of each sample was calculated.

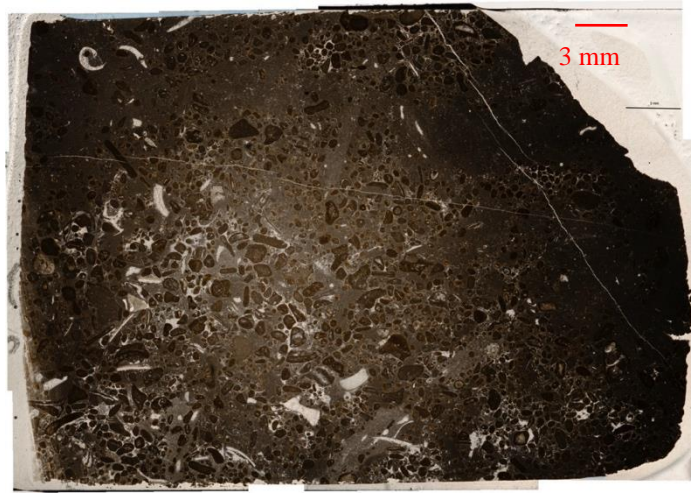
The results are shown in Figures 33 to 49 and synthesized in table 4:



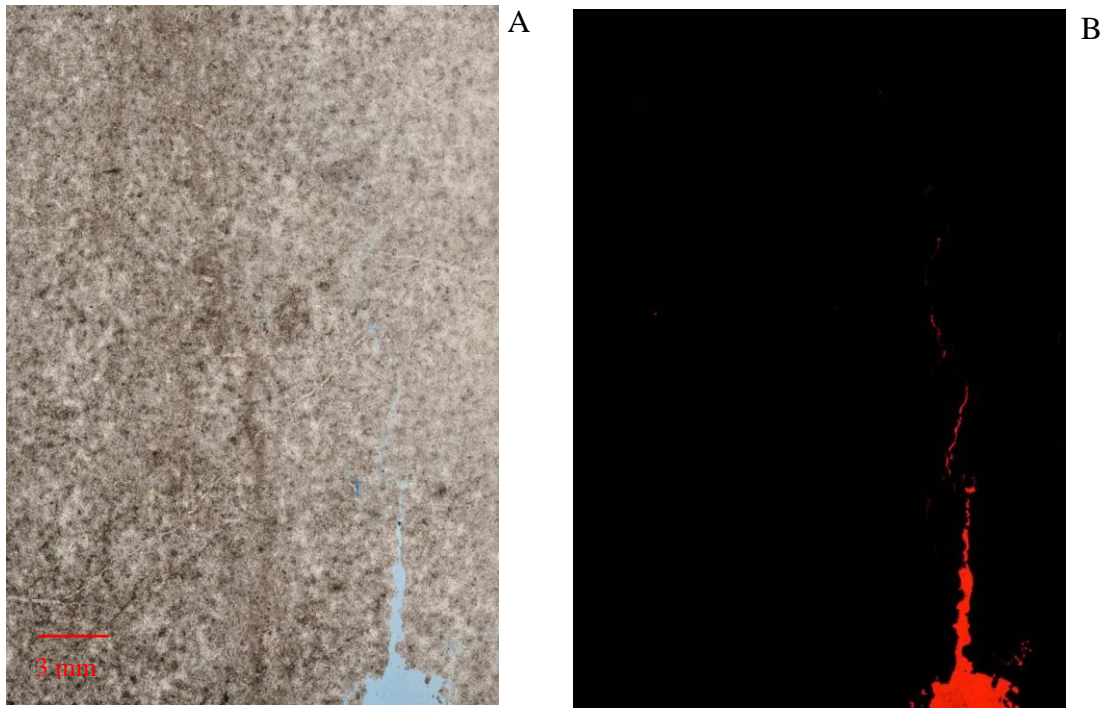
*Fig. 33: Monte Zugna Formation sample 230 (A) and related Mahalanobis Distance method classification (B). This sample is not dolomitized and fractures are filled by cement. There is no porosity at all.*



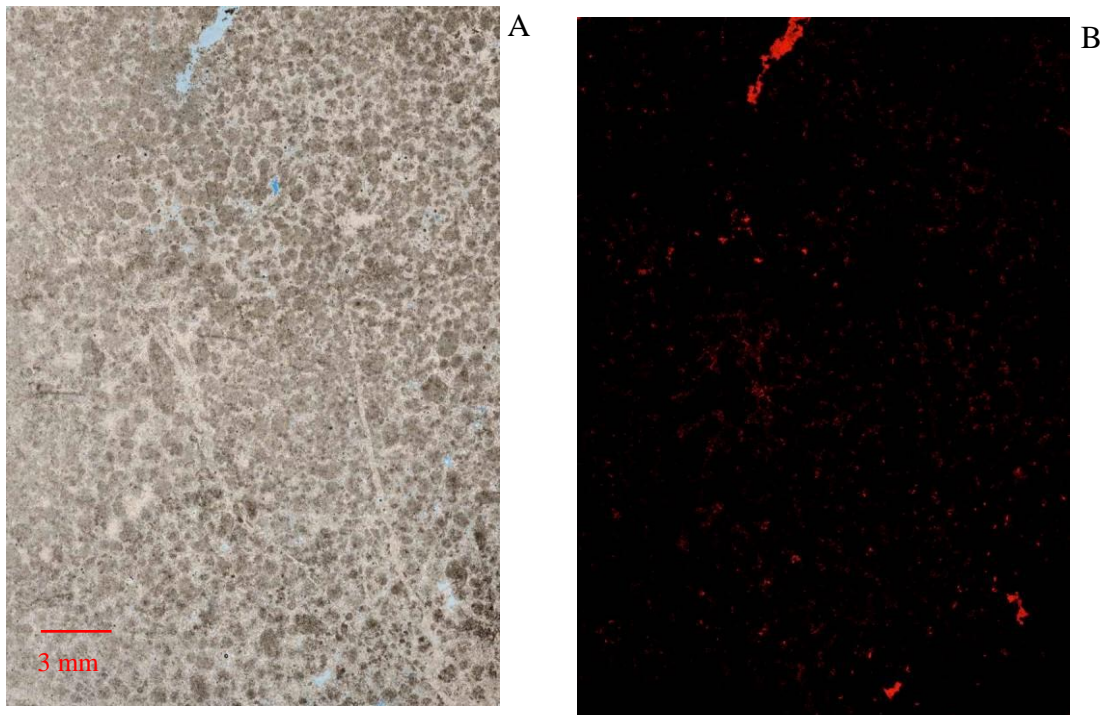
*Fig. 34: Sample of an undolomitized Loppio Formation (sample 236) (A) and Mahalanobis Distance method classification of the image highlighting the cement(B). Ooids and other skeletal parts are visible in A. All the spaces between the grains are filled by cement and actually there is no porosity. Anyway the initial porosity of this Formation had to be very high (20-25% as testify by ENVI classification in B), making it a very good reservoir if the space between the grains were filled by hydrocarbon instead of cement.*



*Fig.35: Rotzo Formation sample 237: remains of organisms are immersed in a mud-matrix with no porosity.*

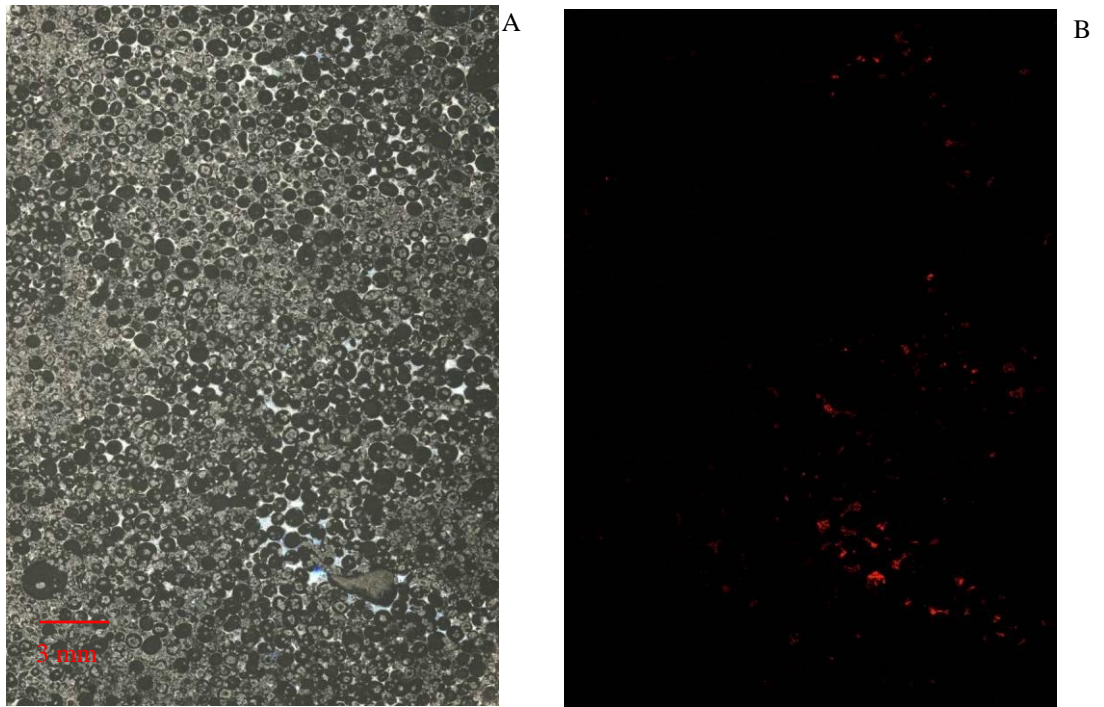


*Fig.36: A sample of deeply dolomitized Loppio Formation (sample 226) (A) where Ooids and skeletal parts are not recognizable any more, porosity is absent as shown by the Mahalanobis Distance method classification (B).*



*Fig.37: Dolomitized Loppio Formation where we can still see shapes of ooids and skeletons (sample 227) (A). This testifies that the sample is less dolomitized than sample 226, but porosity reaches a value of 1,5% as shown in the Mahalanobis Distance classification (B).*





*Fig.38: The dolomitization of sample 229 is very light. Ooids are well preserved and some of them don't present any dolomitization (A); in several part of the section the original cement is still preserved. The porosity is very low with a value of 0,5% as shown in the Mahalanobis Distance classification on (B).*



*Fig. 39: Section of the completely dolomitized Monte Zugna Formation sample 232 with no visible porosity.*

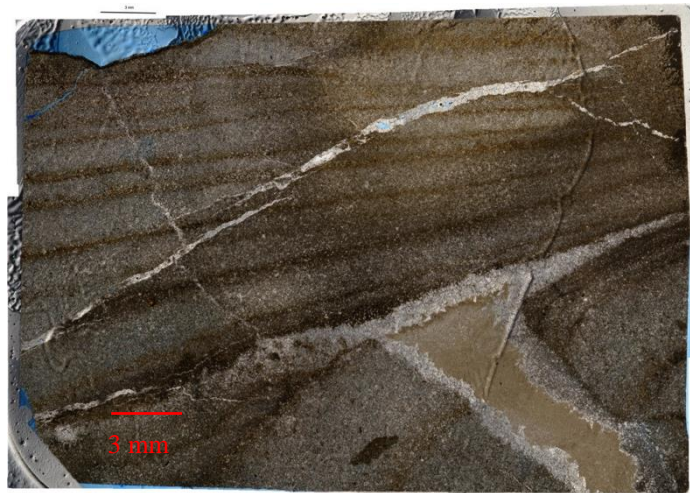


Fig.40: Dolomitized Monte Zugna Formation (sample 233), where no porosity is visible.

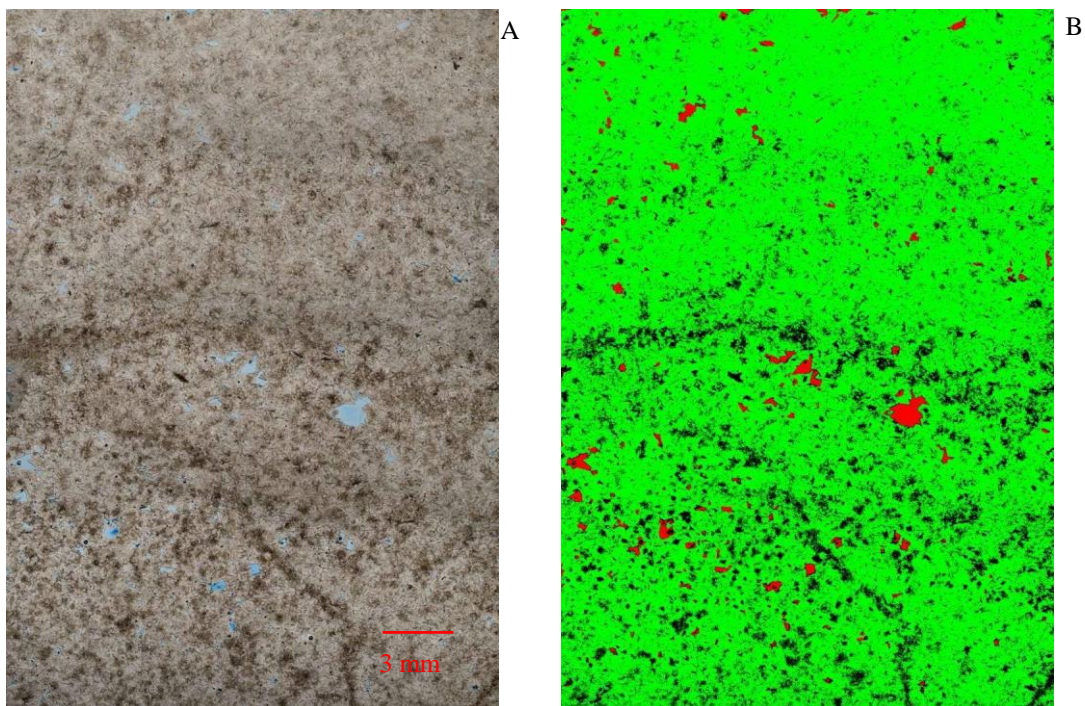
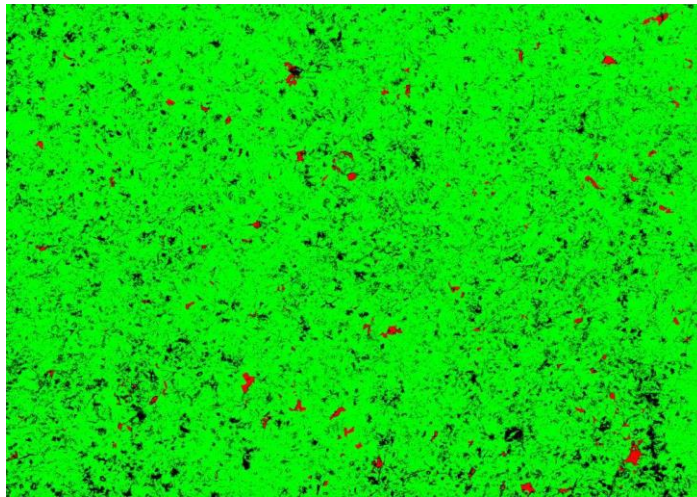
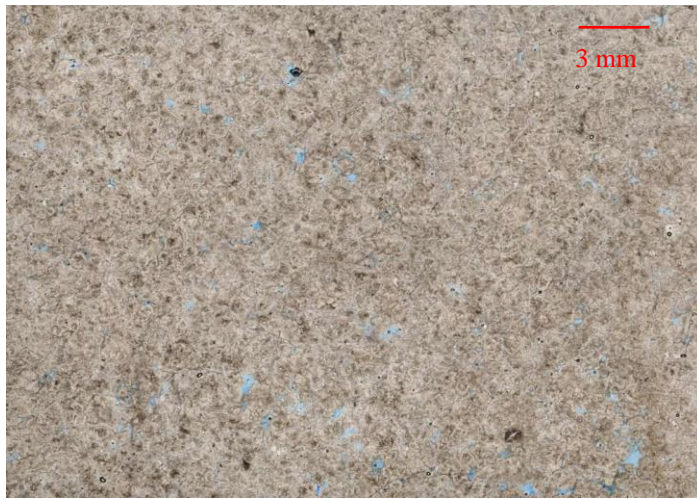


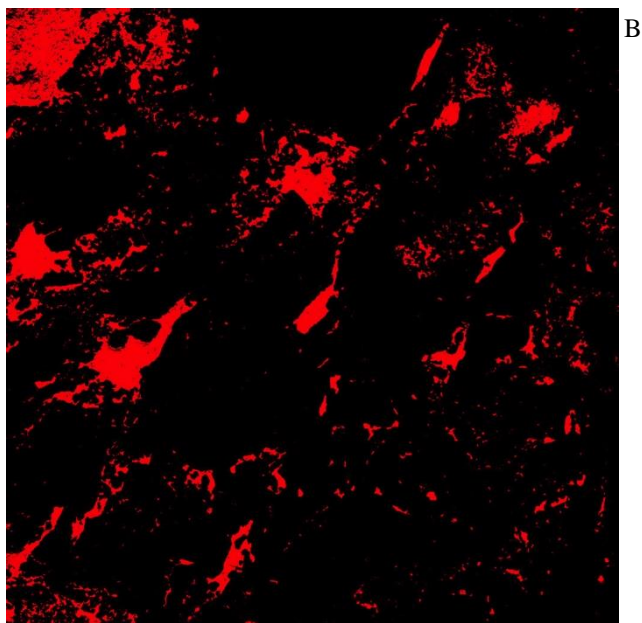
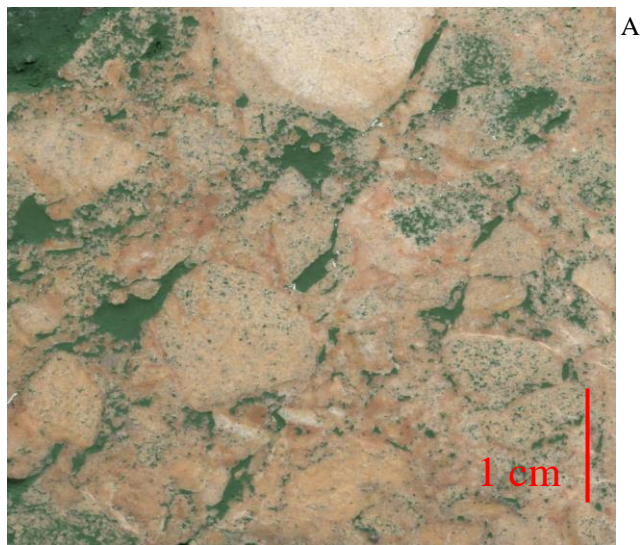
Fig. 41: This section of the dolomitized Loppio Formation sample 234 (A) was analyzed using two class of identification to better help the program during the image analysis . The red class are pores, the green are the rest of the sample and the black areas are not classified (B). The result of the Mahalanobis Distance classification gives a porosity of 2%.



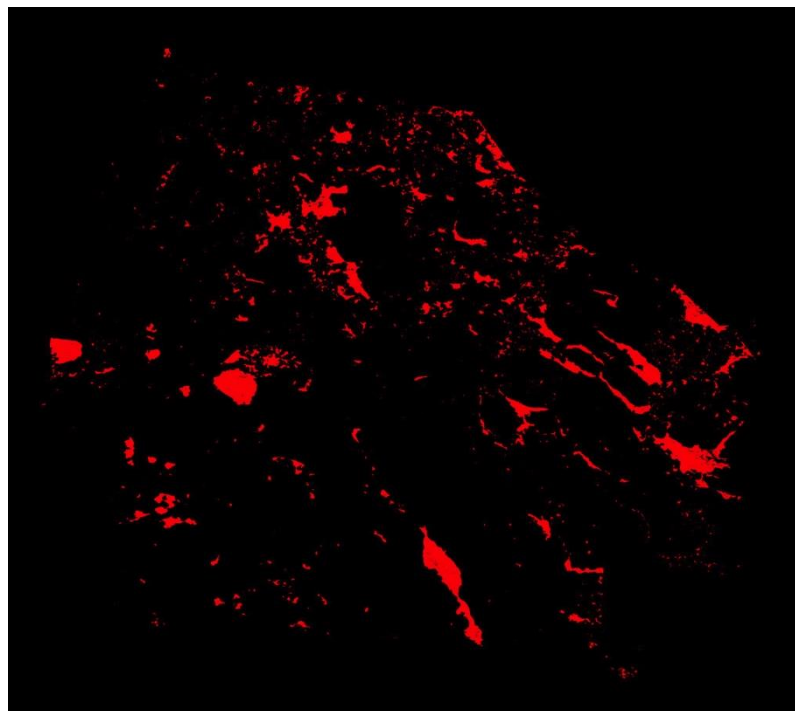
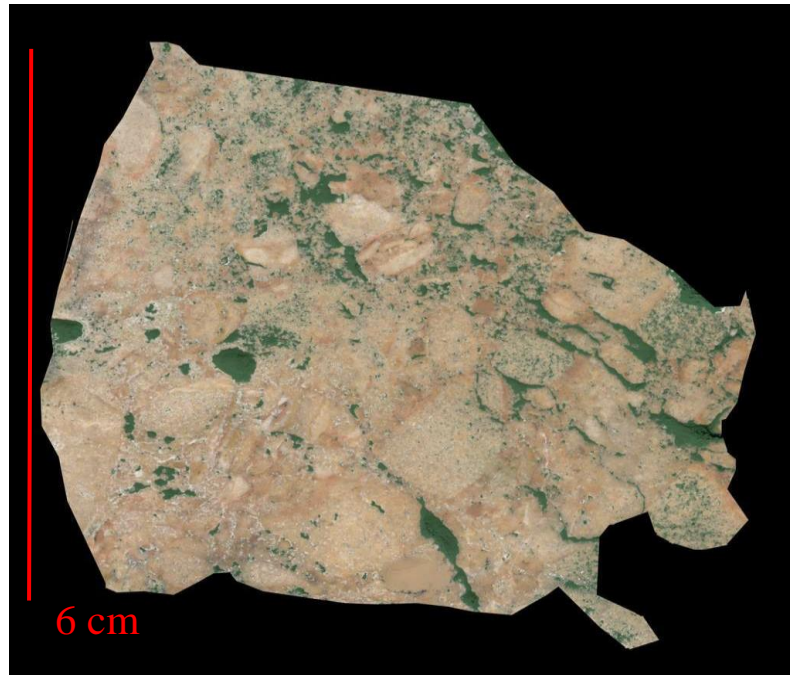


*Fig. 42: Section of the dolomitized Loppio Formation sample 235 was analyzed using two regions of interest and the Mahalanobis Distance classification. Here the porosity has a value of 1%.*

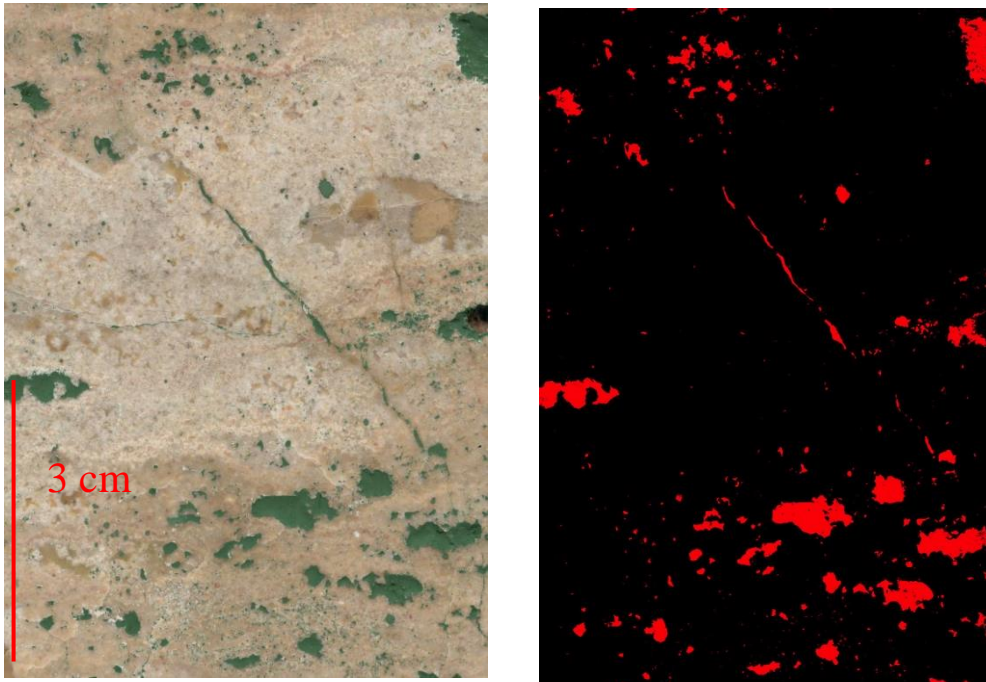




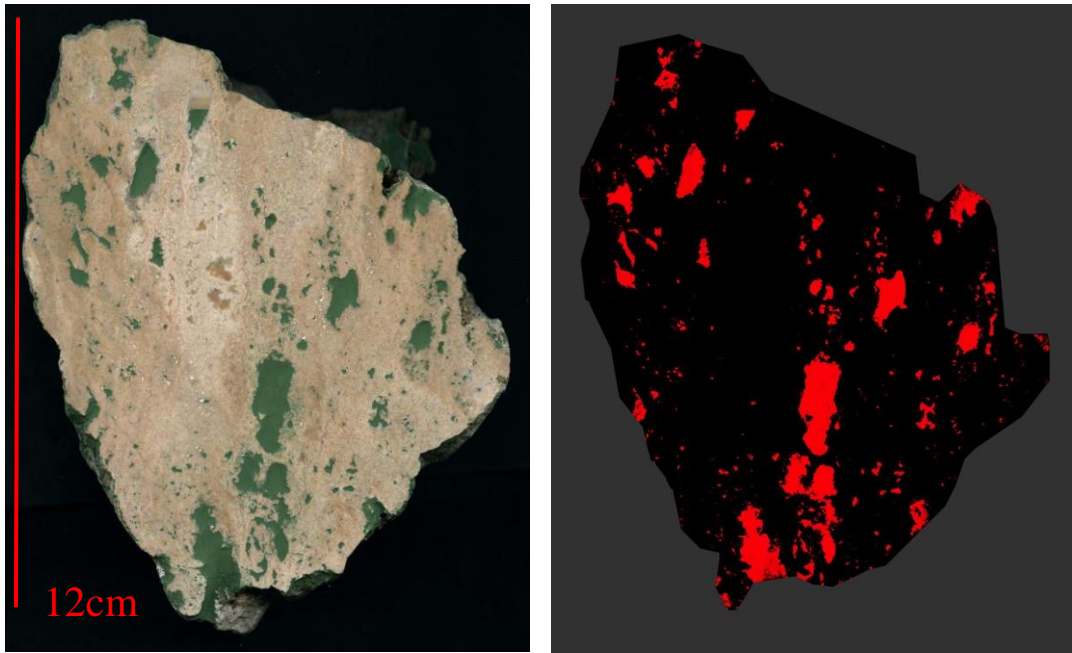
*Fig. 43: Cut sample 228 collected into a dolomitized part of the Loppio Formation is a clearly example of a dolomitized fault-breccia (A). Here the dolomitization created large pores between the clasts and small pore within them. The overall porosity calculated through maximum-likelihood classification reaches a value of 9,38% (B).*



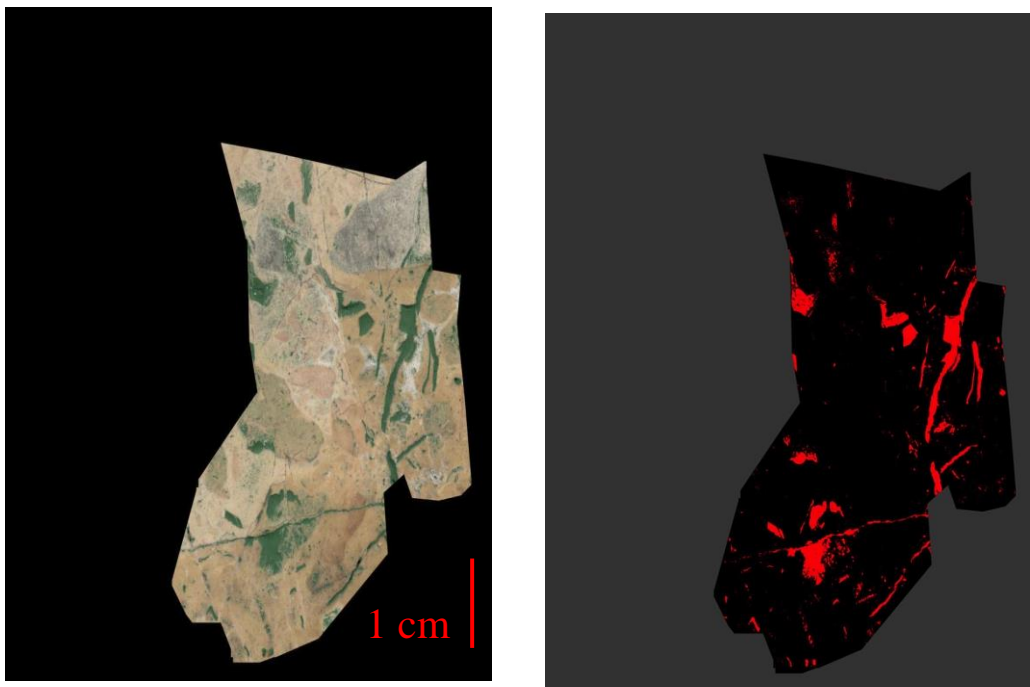
*Fig. 44: Sample number 228\_2 is a different cut with respect to what has been shown in figure 41. The result of the analysis through maximum-likelihood classification give a porosity value of 6,28 %.*



*Fig. 45: A deeply dolomitized sample of Monte Zugna Formation (sample 231). It is a fault-breccia deposit and as in sample number 228 of fig. 41, dolomitization created large pores between clasts. Here porosity value obtained through maximum-likelihood classification is 5,64 %.*

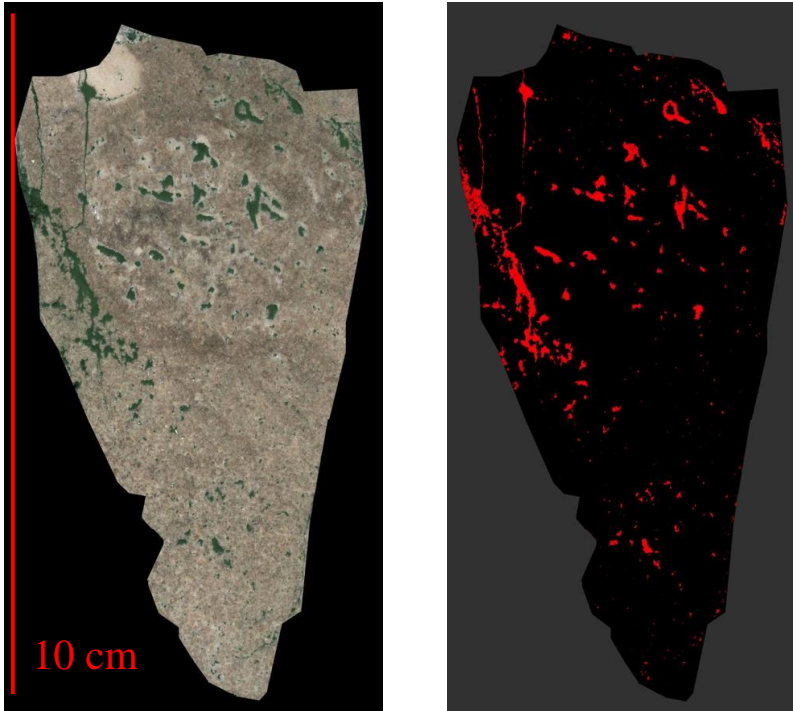


*Fig. 46: The second cut of sample 231 has a porosity of 10,6% calculated using maximum-likelihood operator*

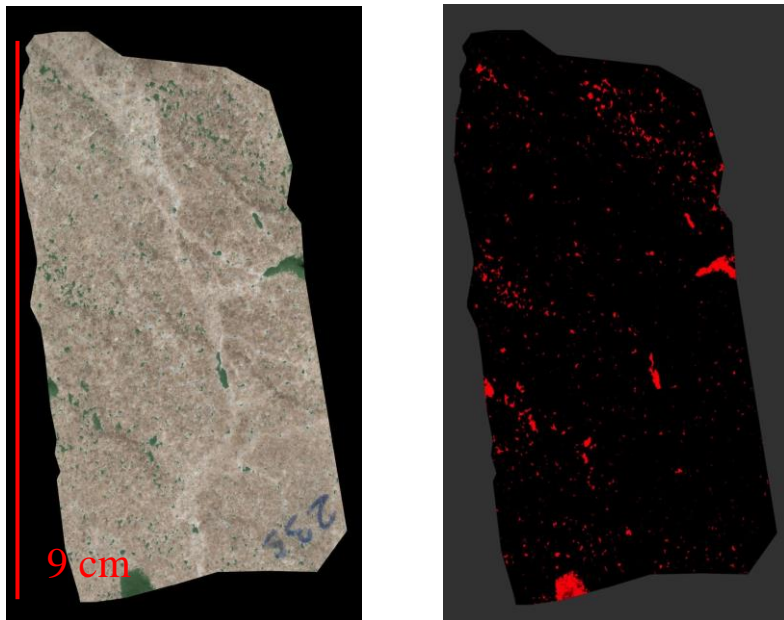


*Fig. 47: Dolomitized breccia of Monte Zugna Formation (sample 233) (A): as the other fault-breccia samples, is characterized by an high value of porosity (7,5%). In this case we can see that the porosity obtained through maximum-likelihood classification is associated with both pores and fractures (B).*





*Fig. 48: Dolomitized sample 234 from Loppio Formation with porosity of 4,5% calculated with maximum-likelihood operator.*



*Fig 49: Sample 235 has been collected close to sample number 234 and show the same characteristics. However, here the pores are smaller and the porosity value calculated with the maximum-likelihood operator is 2,7%.*

Table 4		
Sample	Porosity thin section	Porosity cut sample
226	0 %	/
227	1,5%	/
228	/	1. 9,38% 2. 6,28%
229	0,5%	/
230	0%	/
231	/	1. 5,64% 2. 10,6%
232	0%	/
233	0%	7,5%
234	2%	4,5%
235	1%	2,7%
236	0%	/
237	0%	/

### **3.5 Discussion on porosity**

Our image analysis has shown that the undolomitized Monte Zugna, Loppio and Rotzo Formation have actually no considerable porosity, due to presence of diagenetic cements. Monte Zugna and Rotzo Formation are formed predominantly by mud or very fine grains (fig. 33 and 35). This suggests that the macro-porosity of this formations was very low already before the cementation. For this reason, from the point of view of the petroleum exploration these two formations may be considered as seals. On the contrary the Loppio Formation is formed by uniform strata of ooid grainstones. This type of rocks can have an initial very high porosity that can reach values of 20% (fig. 34). If hydrocarbon fill the pores before cements this type of rocks can form very important hydrocarbon accumulation. For this reason Loppio Formation can be considered a good reservoir before being completely cemented.

The dolomitized bodies show a great variability in porosity. Porosity values changes abruptly in all directions and within the same sample as shown by sample number 233. Indeed the thin section of this sample gives a micro-porosity value near 0% (fig. 40) while macroporosity value obtained from the cut is 7,5% (fig. 47). In general porosity values from thin sections of the dolomitized bodies seem to confirm the observation of Wang et al. 2015 and DiCuia et al. 2011 since poorly (fig 38).as well as very deeply dolomitized samples (fig. 37, 39 ).show the lowest porosity values

The higher porosity values are associated with fault breccias (fig. 43, 44, 45, 46, 47), that probably acted as preferential pathways for the dolomitizing fluids. This suggests that, probably, the best potential reservoir, in bodies involved by secondary dolomitization, must be search into or near the damage zone of faults.

This high porous fault-related bodies are well sealed by low porosity formation since they cut across the Monte Zugna and Loppio Formations but they stop when Rotzo Formation is reached (chapter, 2.1). Indeed the porosity values extracted from the analysis suggest that all these three formations are completely cemented and tight at the sample scale. This is particularly sure also at higher scales for the Rotzo Formation which is mainly formed by mudstones, but, on the other side, we



know from field observations that both Monte Zugna and Loppio Formations are substantially fractured. Porosity from fractures in carbonate rocks usually has a value included from 0,2% and 1% (Weber and Bakker, 1981). For this reason, it is more correct to consider a porosity value of 1% due to fracturing for these formation when fault related dolomitized bodies could have been the main reservoirs.

Theoretically, both structures – i.e. high porosity tilted formation (Loppio) covered by a seal formation (Rotzo) and porous dolomitized bodies surrounded by low porous formation - can be very favorable for hydrocarbon accumulation. However, the accumulation potential depends also from other factors. In the first case it depends from the geometries of the structures, the thickness of the seal and the porosity of the Loppio Formation after the deposition of the seal. For the dolomitized bodies it depends from shape and distribution of the bodies and from the distribution of the porosity within them.

These elements can be verified or predict with the help of a 3D model.

## 4. 3D Analysis

### 4.1 Photogrammetry

As already mentioned a 3D geomodel needs well fixed unit boundaries, reliable azimuth and dip of strata and detailed fault attitudes.

The study area is located in a mountain region where spectacular exposure are hardly accessible. This is the case of the main tectonic structure of the Monte Testa. Here the tilted blocks of the Loppio Formation are impossible to reach and important information about azimuth and dip of strata within the blocks as well as of faults are lacking.

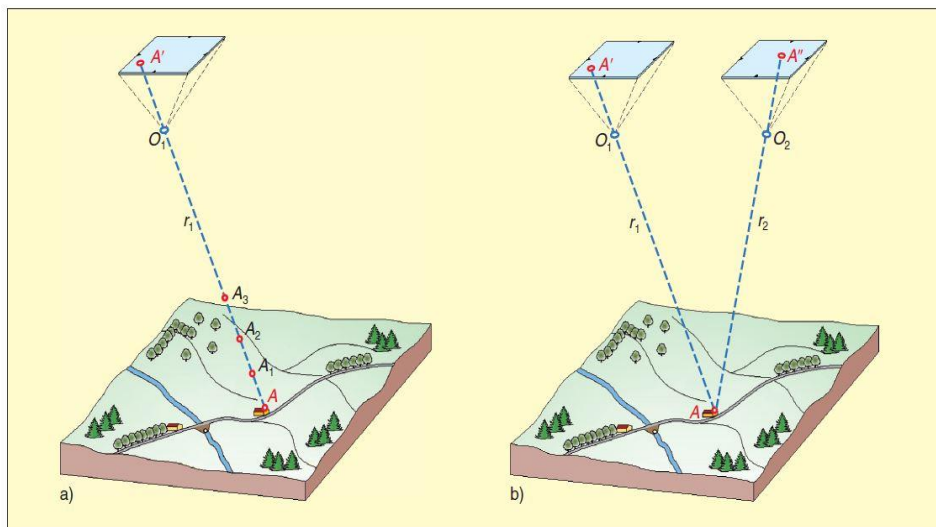
In some cases, this problem can be solved by using a DTM model. If the DTM has a sufficient resolution, the boundary between rock formations can be traced directly on the DTM model and strata azimuth and dips can be easily extracted.

The available DTM of the Provincia Autonoma di Trento was obtained from airborne LIDAR nadir scan of the surface. This means that the obtained point cloud has a high resolution when the surface is almost perpendicular to the laser pulse and badly resolved when the topographic surface is very steep.

The main tectonic structure of Monte Testa is nearly vertical, this makes impossible to trace the boundary between rock units on steep cliffs directly on the LIDAR DTM model and consequently derive strata azimuth and dips. To overcome this issue, the badly resolved steep area of the DTM, can be integrated with a high resolution photogrammetric model.

Photogrammetry is a remote sensing passive technique, that allows to define shape, position and dimension of an object using information obtained from images of the object captured from different points of view.

Photogrammetry is based on the principles of the central perspective. In a photographic camera, lens converge the ray coming from an object in one point called optical centre (O) and then impress them on the CCD or photographic film. Each point of the object (A, B, C...) have a homologous point (A', B', C'...) on the image. From a single image is not possible to extract information about shape and position of an object: since point A' on the image is the homologous point of point A on the object as well as all the points of the ray r connecting points A and A' and passing through the optical centre (Fig.50). Using two images the point A on the object has a homologous point A' on the first image and another homologous point A'' on the second image. Knowing the position of the homologous points A'



*Fig.50 : From a single picture is not possible to define the position of a point (a), while the position of a point is perfectly define by the intersection of r and r' coming from two pictures (Canarozzo et al., 2012).*

and A'' on the images and of the points O and O' from where the images were taken, it is possible to define the position of point A, which is the intersection point of the two project rays r' and r'' (Cannarozzo et al., 2012).

The relationship between these positions (positions of A, A', A'', O and O') is define by the collinearity equations.

$$y - y_0 = -c \frac{R_{12}(X - X_0) + R_{22}(Y - Y_0) + R_{32}(Z - Z_0)}{R_{13}(X - X_0) + R_{23}(Y - Y_0) + R_{33}(Z - Z_0)}$$

$$x - x_0 = -c \frac{R_{11}(X - X_0) + R_{21}(Y - Y_0) + R_{31}(Z - Z_0)}{R_{13}(X - X_0) + R_{23}(Y - Y_0) + R_{33}(Z - Z_0)}$$

where x and y are the coordinates of the homologous points; x<sub>0</sub> and y<sub>0</sub> are the coordinates of the optical centre; X, Y, Z are the coordinates of the object point and X<sub>0</sub>, Y<sub>0</sub>, Z<sub>0</sub> coordinate of the perspective centre; R represent the roto-traslational matrix.

From the equations above, it is clear that collinearity equations can be used only if the coordinates of the principal points (homologous points) and the principal distance (distance between the optical centre and the CCD or film) are known. These two parameters are called interior parameters. Moreover, the exterior parameters which are the coordinates of the optical centres and the rotational angles of the camera with respect to the reference system, must be known too.

The realization of a photogrammetric survey follows three main steps:

1. Image acquisition. During this step different types of cameras can be used: metric cameras, built for photogrammetric purpose with known interior parameters, semimetric camera with not stable interior parameters and a large optical distortion with respect to the metric camera, amatorial camera for which the interior parameters are calculated through a process called autocalibration.
2. Orientation. During this phase, the interior and exterior orientations are defined.
3. Creation of the 3D photogrammetric model

### 4.1.1 Image acquisition

To assure a correct alignment of the images, they must cover the whole object, be taken from different points of view and possibly with the same focal length.

### 4.1.2 Interior orientation

From a theoretical point of view, all the rays coming from an object link the points of the object with their homologous passing through the optical centre. This is not always true because of errors caused by camera imperfections (e.g.: lens distortions) or by external factors such as atmospheric refraction. All these errors can be minimized through interior orientation processes, which establish the position of the point O with respect to the film or CCD.

### 4.1.3 Exterior orientation

The exterior orientation defines the position and the angular orientation of the camera at the time of the capture. Six parameters are necessary to define each frame: the 3 coordinates of the optical centre and the rotational angles of the camera along its 3 major axis.

The exterior orientation establish a relationship between the reference system of the object ( $x, y, z$ ) and that of the camera ( $X, Y, Z$ ), (Fig.51).

Nowadays this operation are performed by computer softwares as for example

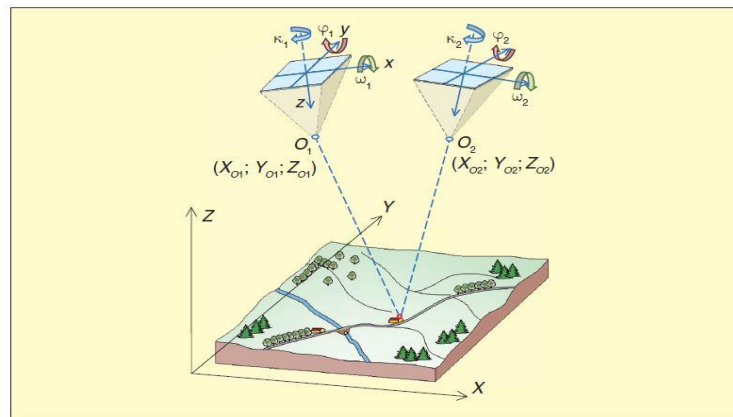


Fig. 51: The exterior parameters necessary to perform the exterior orientation (Canarozzo et al., 2012).

Agisoft Photoscan used during this work. The software calculates the exterior parameters through the determination of the position of the homologous points present on both frames. Moreover, it is possible to use the coordinates of ground control points to georeference the images onto a given reference frame.

The exterior orientation can be performed through three different methods: 1. Independent orientation of two frames; 2. contemporary orientation of two frames; 3. contemporary orientation of two frames in two steps.

The most used is method number 3. Here, a relative orientation of the two frames is retrieved in order to relocate the two frames in the same position they had with respect to the real object at the time of acquisition. However, this procedure allows only a relative relocation in a reference system ( $X'$ ,  $Y'$ ,  $Z'$ ) different from the object one, hence the reconstructed 3D object will be similar to the real one but located in a generic position of the space.

For this reason, a second step called absolute orientation is needed. During this step, the generic model created during the relative orientation is thus moved to the reference system of the real object and it is converted to the correct scale. This operation is facilitated by Ground Control Points.

#### **4.1.4 3D photogrammetric model**

When the exterior orientation is performed is possible to create the 3D photogrammetric model. The model will have the same reference system and scale of the real one and it is thus possible to extract any quantitative information (Cannarozzo et al. 2012).

#### **4.1.5 3D photogrammetric model of the Monte Testa main structure.**

The photogrammetry reconstruction of the M. Testa syn-sedimentary structure was realized in collaboration with the SMART3K company of dott. Alessandro Rizzi through two main phases:

1. Image acquisition
2. Creation of the 3D photogrammetric model through the use of Agisoft Photoscan software.

##### ***4.1.5.1 Image acquisition***

403 photos were acquired using a Nikon D800E camera integrated with a GPS system. The focal lengths ranged from 28 mm to 250 mm. Hence, we have obtained either images with a large field of view and a low resolution and images with a narrow field of view but a higher resolution.

Due to the impervious topography the available points of view were limited to 11, acquired at a distance ranging from 250 m to 1500 m from the cliff where the main structure of the Monte Testa is exposed (Fig.52). This did not guaranteed an optimal photographic coverage and created problem during the following search of the homologous points necessary for the alignment of the images.



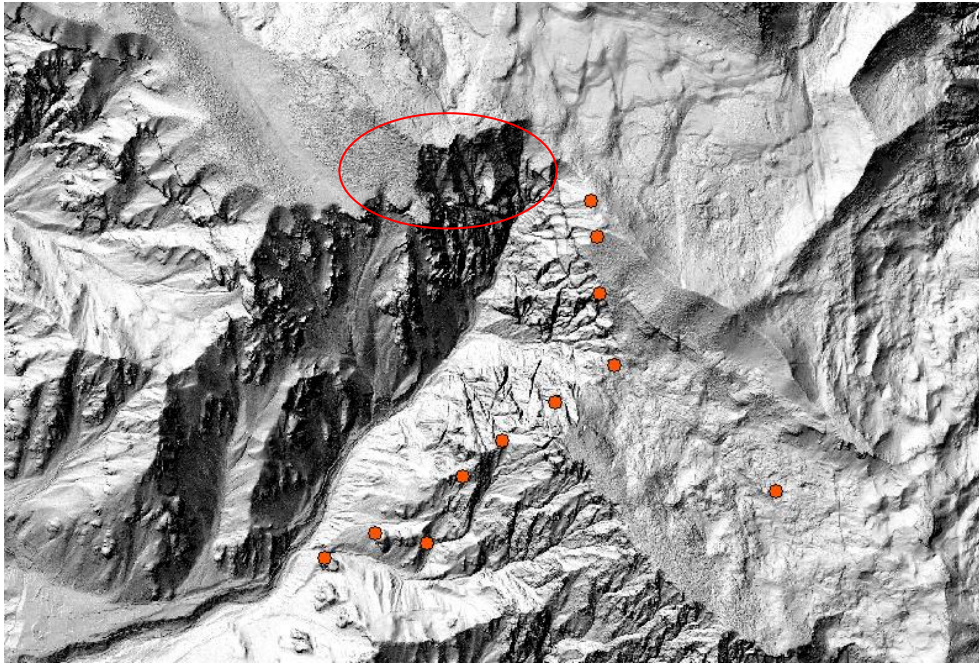


Fig.52: The 11 point where the pictures were taken In the red circle the photographed area

#### ***4.1.5.2 Creation of the Photogrammetric 3D model***

The 3D photogrammetric model was realized using Agisoft Photoscan software, which can calibrate and orientate the images either automatically or with the user supervision. By contrast, the realization of the 3D photogrammetric model is completely automatic.

The creation of the model in Agisoft has followed these steps:

1. Import of selected images with eventual homologous points visually recognized;
2. alignment of the images and creation of a sparse point cloud.
3. If the alignment is good extraction of a dense point cloud;
4. generation of a triangulated mesh;
5. application of a texture derived from the imported images.

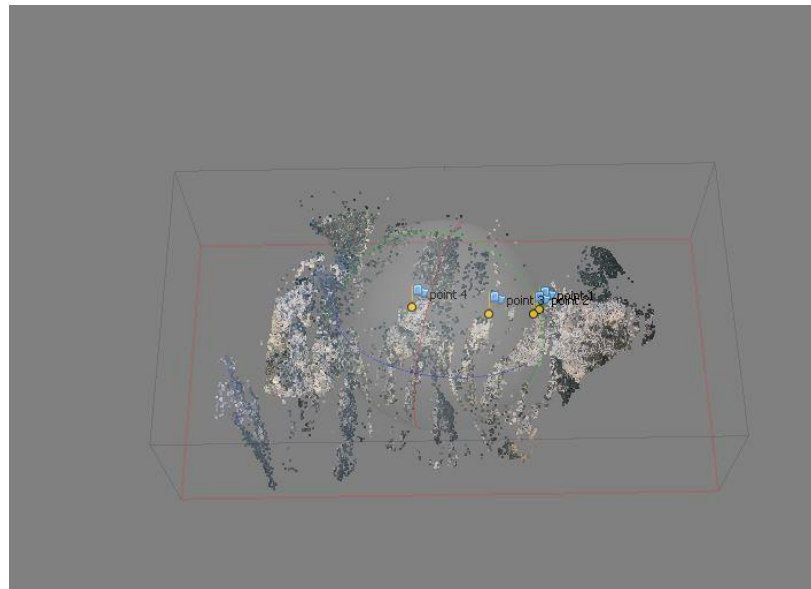
The first step for the realization of a 3D photogrammetric model is the selection of the photos. The photos were divided into two groups: the first one includes photos with a lower focal length (131 photos; f. length: 28-100mm); the second one contains those with a higher focal length (282 photos; f. length 100-300mm ).

This subdivision is required because photos with considerable difference in the focal length are difficult to align during the 3D modeling process because of their different resolutions. All images were then imported in Photoshop to improve brightness, contrast and saturation which should be as much similar as possible to allow the image alignment and facilitate automatic homologous points detection. After this preliminary stage, we have created the 3D photogrammetric model in Agisoft. This software can find the correct alignment among images automatically searching the homologous points. This operation was the most difficult one since the image coverage of the area was not optimal.

This issue forced us to repeated attempts for image alignment and at the end only 12 photos with low focal length from 28 mm to 300 mm and taken from six different points of view were finally selected.

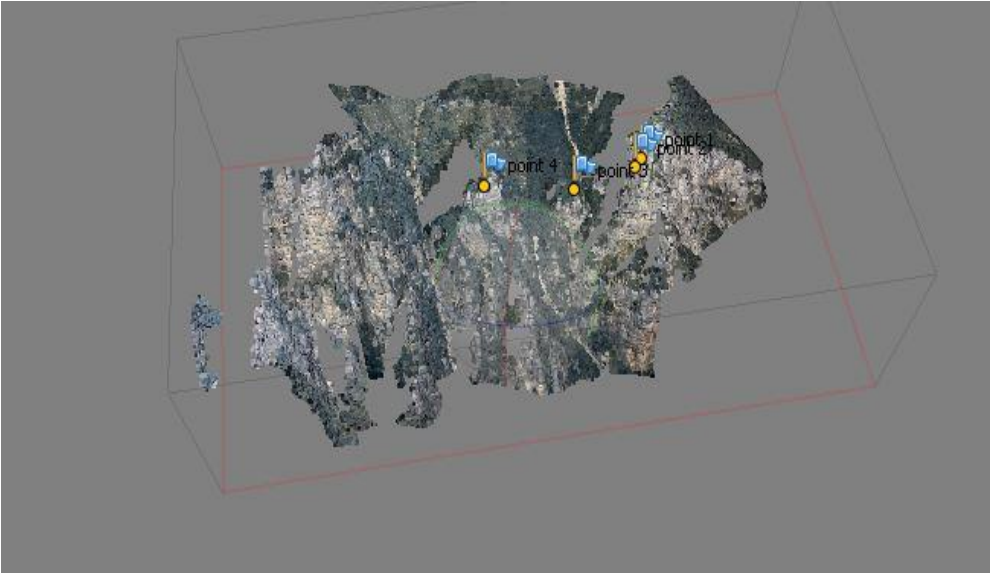
Also the homologous points were hard to find automatically and I had to manually insert four of them (markers) during step 1.

After this, it was possible to start the alignment of the images and the software generated the sparse point cloud (fig.53).



*Fig.53: The sparse point cloud with the homologous points added manually*

Considering that the alignment of the images was good enough the dense point cloud was also extracted. (fig.54)



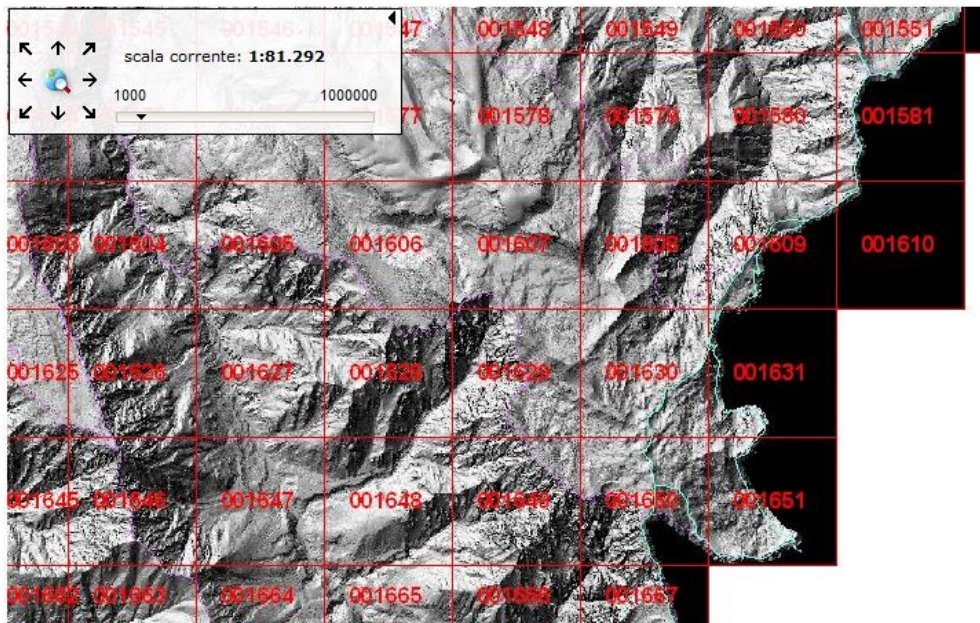
*Fig.54: The dense points cloud*

## 4.2 3D topographic model

### 4.2.1 Lidar DTM and topography

The data used in the realization of the 3D model of the Monte Testa synsedimentary structure are essentially surface data. They were derived from field mapping and from the tracing of relevant geologic features (unit boundaries and faults) on the 3D model of the topographic surface of the area.

The airborne Lidar point cloud of the Provincia Autonoma di Trento was used to prepare the topographic base. It is composed by 1753 blocks of 2x2 km of side covering the entire Province.



*Fig. 55: The DTM of the Provincia autonoma di Trento. In green the Lidar blocks using in this work*

For this work, we used the block showing in fig. 55.

Every block is formed from about 4 millions of points and all together, the blocks used in this thesis have 64 millions of points. The workstation used for this study was not able to work with such as great amount of data, hence the point cloud was decimated.



The blocks were imported in Cloudcompare, a free software that allows to decimate the point cloud and to merge the blocks in a unique point cloud. A point-set formed by only 600000 points was created (fig. 56), imported in skua gocad, and triangulated to create the surface topography (fig.57).

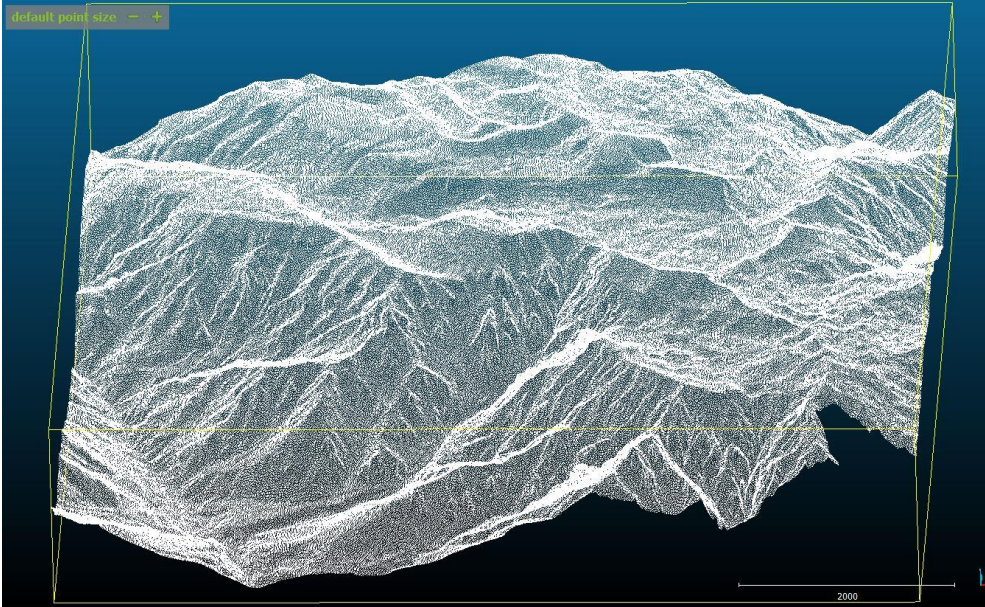


Fig.56: The decimate point cloud in cloudecompare software

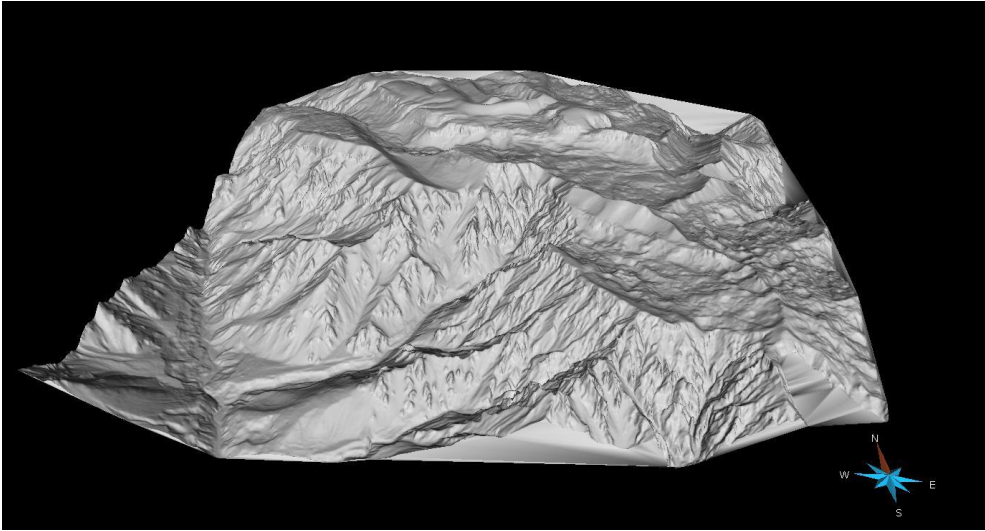


Fig.57: The triangulated mesh created in Skua-gocad

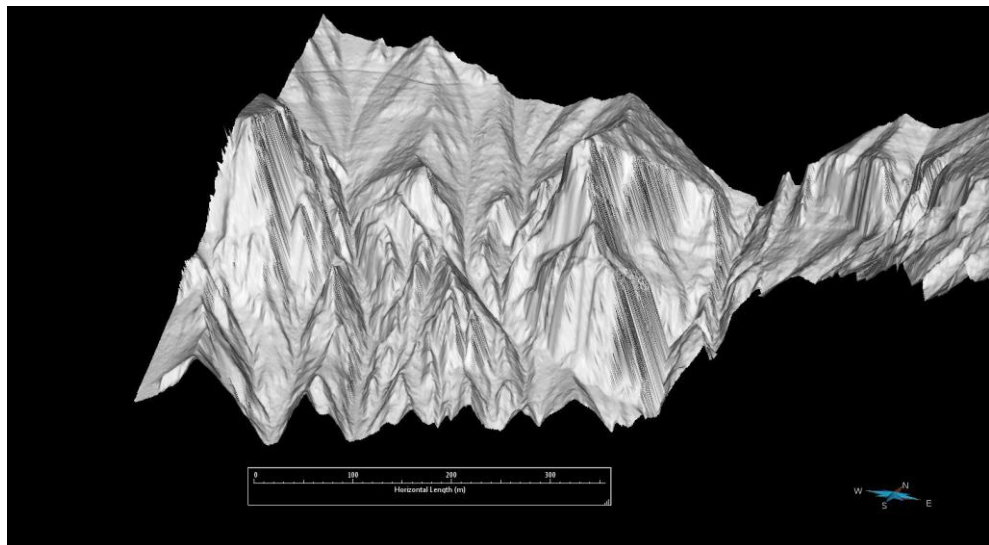
#### 4.2.2 Integration of the Photogrammetric model with the DTM

In order to edit boundary and faults of the main structure of the Monte Testo we have integrated the photogrammetric model with the Lidar DTM.



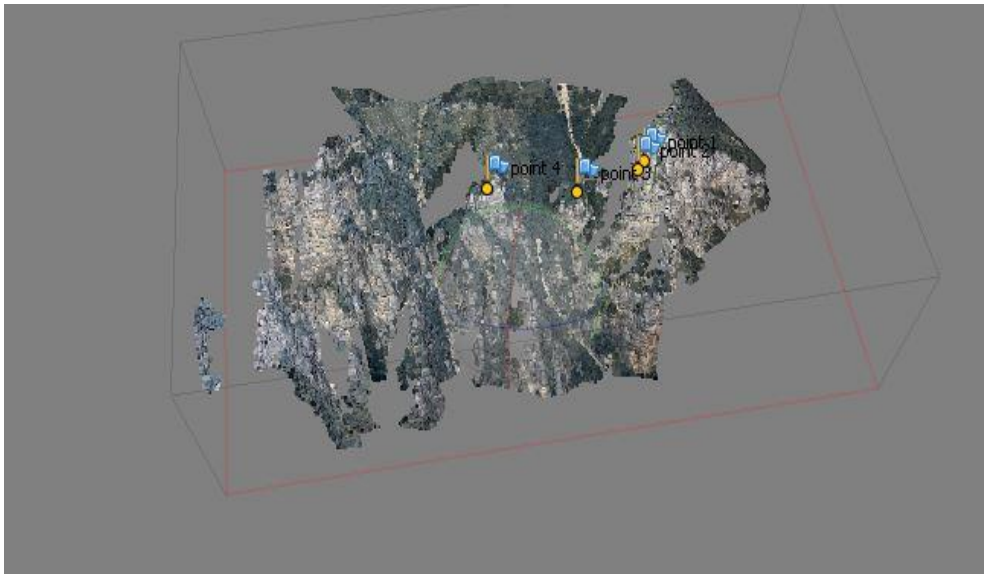
*Fig.58 : The main tectonic structure of the Monte Testo*

To perform this operation, the photogrammetric point cloud must be texturized and improved.



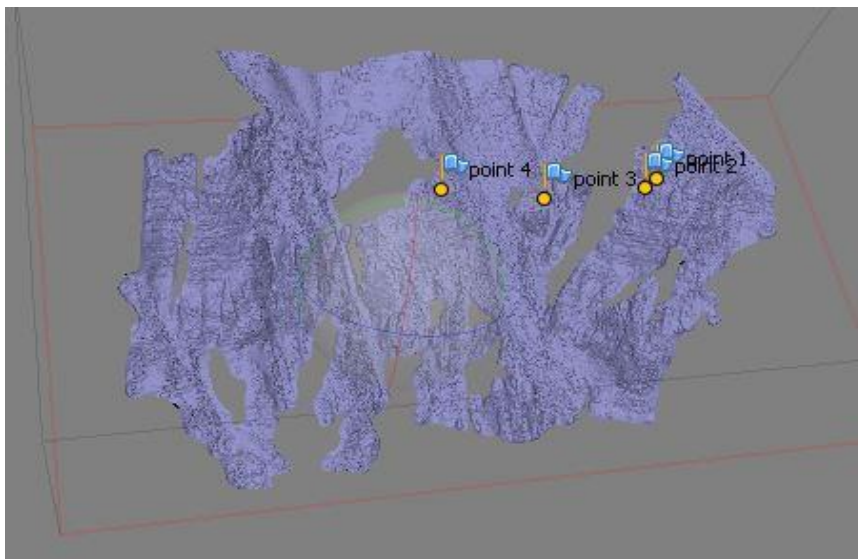
*Fig.59: The triangulated mesh of the structure. We can see that the resolution is very low.*





*Fig. 60: The photogrammetric point cloud*

As we can see in fig. 60, the point cloud is not completely filled and it has some holes due to occlusion effects, inevitable for such a rough area and so few available images. To solve this problem is possible to use Polyworks software. This software has a specific tools called “fill holes” that permits to fill automatically the holes of a mesh



*Fig. 61: The mesh created in Agisoft Photoscan*

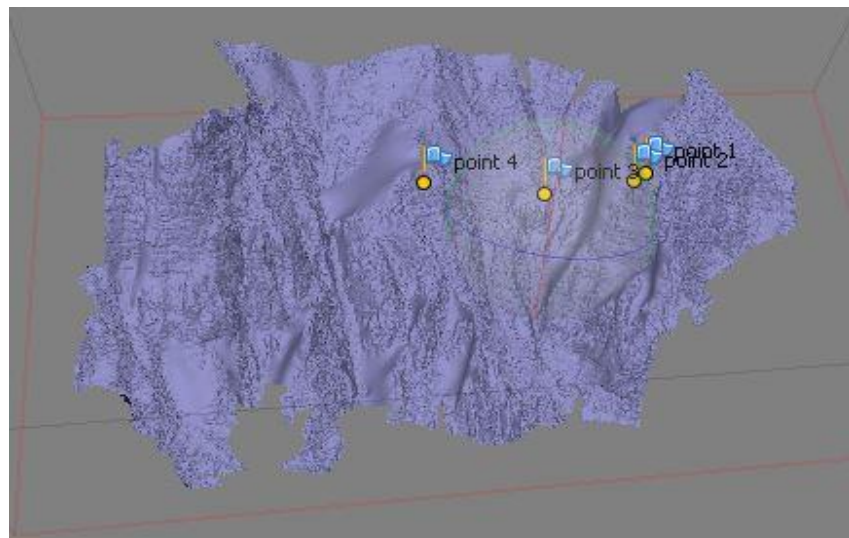


For this reason, after having automatically generated the mesh in Agisoft (fig. 61), we imported it into Polyworks.

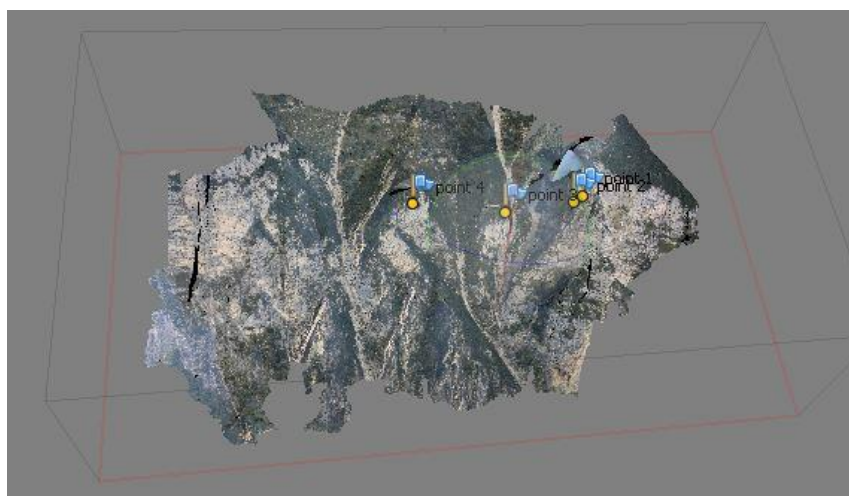
Here the holes were filled using the tool “fill holes” and the photogrammetric model was georeferenced using the Lidar DTM.

In particular choosing three or more homologous point on the two model, Polyworks overlapped automatically the photogrammetric model on the Lidar DTM generating the roto-traslation matrix for the georeferencing process.

The georeferenced mesh of the photogrammetric model was once again imported in Agisoft (fig.62) and covered by a photographic texture obtained by the 12 selected photographs (fig.63).

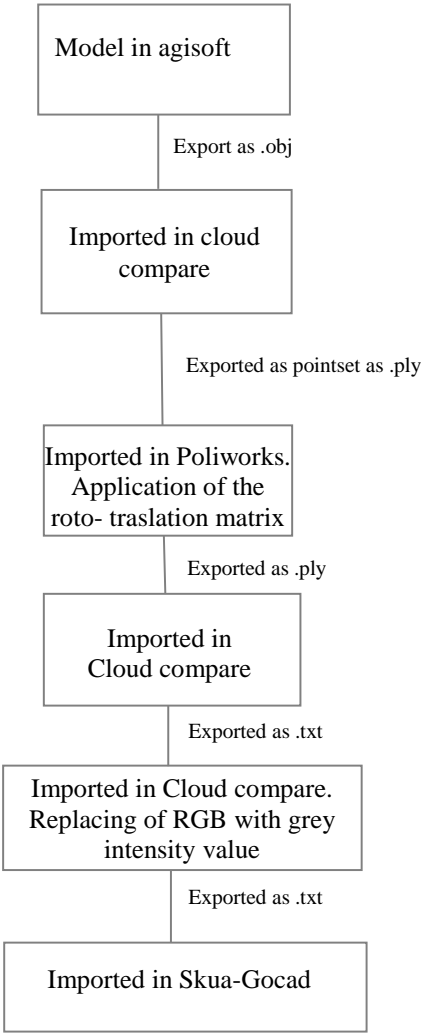


*Fig.62: The mesh after the filling of the holes and georeferentiation*

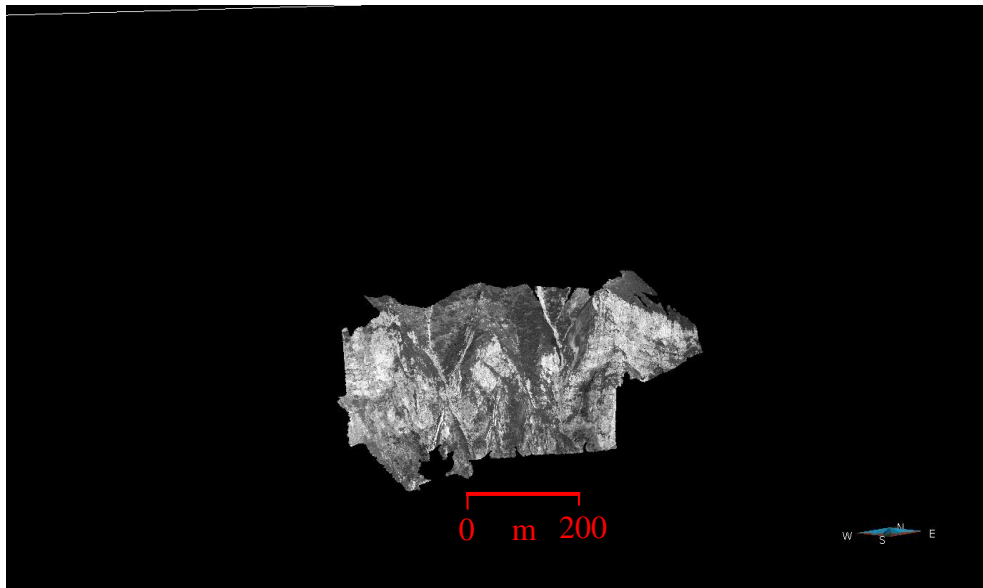


*Fig.63: The texturized mesh*

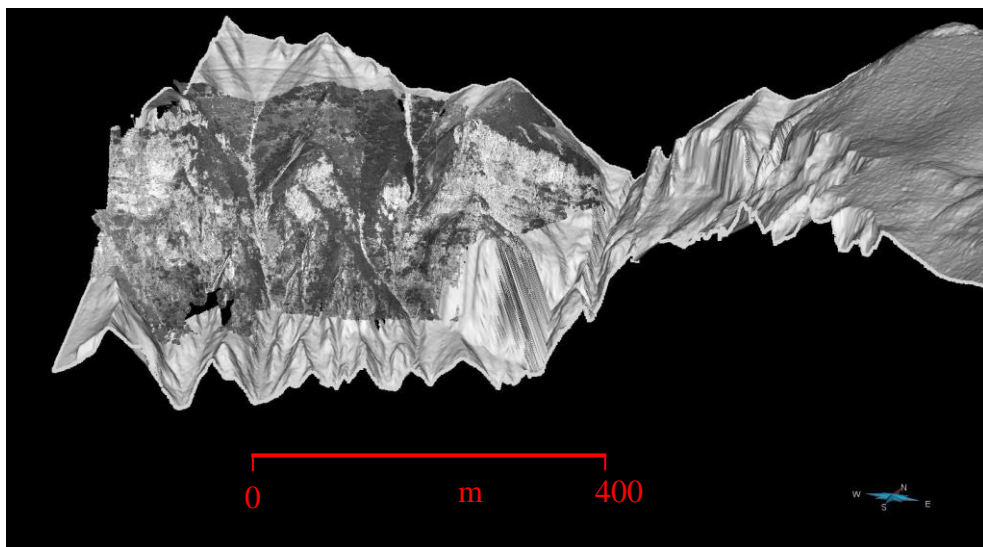
Hence, at each point of the model are associated the X, Y, Z and RGB (colour) values. Unluckily, Skua software is not able to visualize RGB. The RGB values that must be replaced with a value of grey Intensity following the workflow of fig. 64.



*Fig.64: The Workflow followed for the integration of the photogrammetric model with the DTM*



*Fig. 65: The photogrammetric model imported in Skua-Gocad*



*Fig.66: The photogrammetric integrated with the DTM*

## 4.3 3D geological modeling in Skua/Gocad

### 4.3.1 General remarks

3D geologic modelling is widely used in hydrocarbon exploration for the characterization of reservoirs. In particular, the main goal for which it is applied is the realization of flow simulations and distribution of petrophysical properties. The information that can be obtained are essential in the analysis of the possible reservoirs production scenarios (Skua 2009.2 User Guide).

In extreme synthesis, 3D modelling goes through the following phases:

1. Modelling of the geologic surfaces that define the geologic object under investigation (these may include: geologic boundaries between formations/units, faults, etc.).
2. Discretization of the volumes defined by the modelled geologic surfaces. In the discretization the volumes are transformed into grids of normally squared cells.
3. Distribution of petrophysical properties in the grids through the attribution of values to the grid's cells. This can be done using several geostatistical techniques that are chosen if function of the property that has to be distributed.

Nowadays, standard modelling workflows apply pillar-based approaches (Petrel, Gocad) (fig.67). A pillar is a straight line that ties cells together from the top to the bottom of the grid (Structurally complex reservoirs, 2007). In this method, faults are the first geologic surfaces that has to be modelled, because they represent the basis for the generation of the 3D grid. The cells must be parallel to faults and cannot be truncated by them. This method may not be suitable in modeling complex geologic objects, for instance in the presence of complex tectonic structures, oblique faults and thin layers. This is due to the fact that faults' and horizons' geometries are linearly approximated and this can create gaps and cells overlaps (Paradigm, Structure and stratigraphy, 2011). Moreover, pillar-based techniques may generate deformed cells in the grid, this can affect the distribution of petro-physical properties and the reliability of flow simulation results.

A way to minimize this problem is to keep the geo-model as simple as possible, especially from the structural point of view. Obviously, the simplification must be done carefully, and the degree to which it can be pushed depends on the studied object and on the ultimate goal of the modelling. On the other side, the pillar-based method can be very fast and can be easily modified as needed (Structurally complex reservoirs, 2007).

Skua-Gocad uses a different modelling approach. This method generates *geologic grids* and was developed in the attempt of solving some of the limitations of the pillar-based techniques. The geologic grid cells perfectly fit horizons and faults and are not deformed in the geological space and can be split across the faults (Paradigm, Structure and stratigraphy, 2011). In this way volumes and distances in the surface model are preserved with no distortion (fig.67).

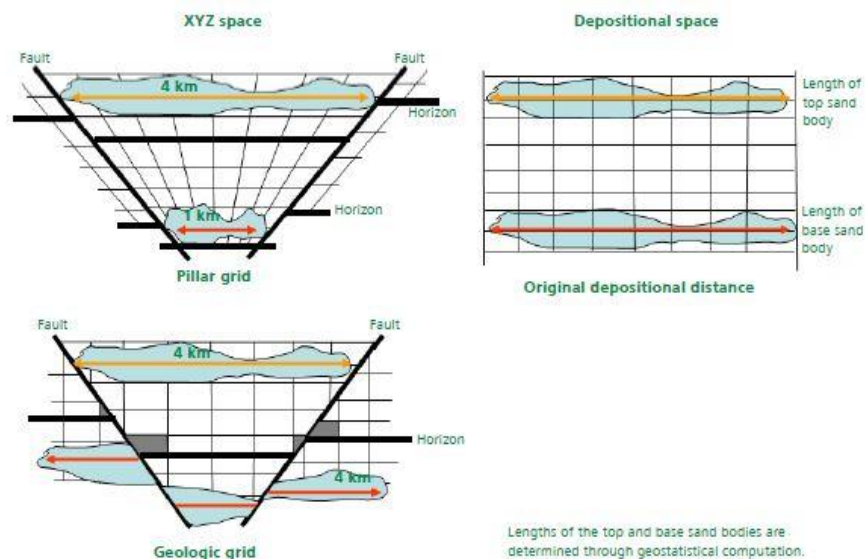


Fig. 67: The difference between pillar grid and geological grid (Skua 2009.2 User Guide).

### 4.3.2 Geologic modelling in Skua/Gocad

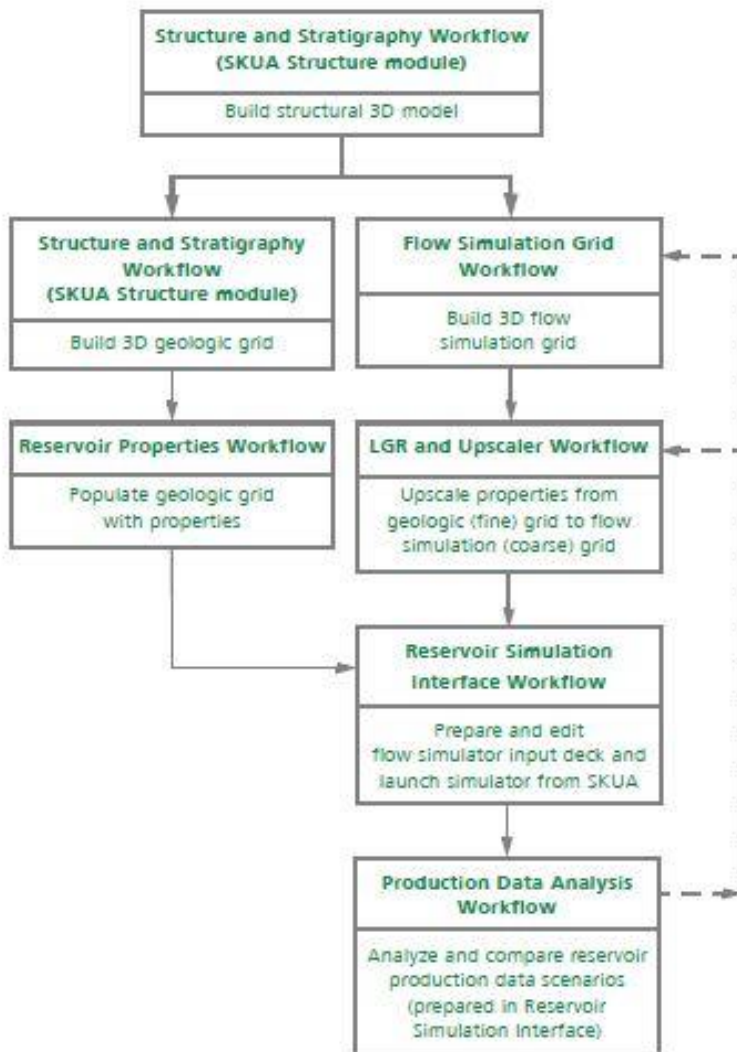
The realization of a 3D geomodel with Skua-Gocad software passes through two main steps. 1. The realization of the structural model that includes geologic boundaries and faults. 2. The generation of the geologic grids.

In the first step data for modelling the geologic boundaries (for instance seismic lines, cross sections, DTMs, wells, etc.) are imported. As mentioned, the first modelling phase aims at reconstructing the geologic surfaces (boundaries, faults) that will define the model's volumes. Obviously, the type of imported data will depend on the kind of geologic object that is going to be modelled. In case of a buried reservoir, most data will refer to the subsurface (seismic, wells), while, in case of an exposed object, like in the case considered in this study, data will be mostly surficial (e.g. DTMs, geologic maps) and/or derived from the interpretation of surficial data (geologic cross sections).

The 3D reconstruction of the geologic surfaces at Monte Testa started from the digitalization, as 3D polylines, of the mapped geologic boundaries and faults on the DTM derived from the integration of LiDAR and photogrammetric model. In-depth constraints were provided by geologic cross sections drawn using the Skua editing tools. Geologic surfaces fitting the digitized polylines were then reconstructed in 3D as triangular meshes using SKUA surface generation tools.

When horizon and fault surfaces were ready, they defined volumes that were discretized by generating the 3D geologic grid.

Modelling in Skua-Gocad is done through various work-flows (fig.68) that differ in their final output. In this thesis, the Structure and Straigraphy workflow was used.



*Fig. 68: Modelling in Skua-Gocad can be approached with workflows that allow generating geologic structural models and reservoir production scenarios. In this work, the Structure and Stratigraphy workflow was used (Skua 2009.2 User Guide).*



### 4.3.2.1 Polylines and surfaces in Skua/Gocad

In this paragraph, general considerations about the generation and editing of polylines and surfaces in Skua/Gocad are reported.

A polyline is formed by a set of points grouped in connected or disconnected (Fig.69). Curves can be used to edit fault polygons, contour lines, horizon boundaries and well log data.

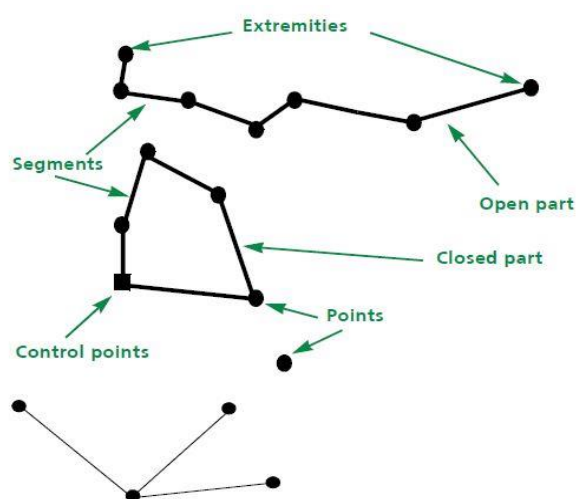


Fig. 69: The main components of a curve (Skua User guide).

In SKUA, curves can be directly digitized on an object (ex. On a DTM or geological section), using the digitization tool. Single segment curves, open multi segment curves or close multi-segmented curves can be created. (SKUA User-Guide).

Furthermore, curves can be created starting from existing object: points, curves, curves parts, surfaces borders, well log and well paths.

A surface is made up of connected (and/or disconnected) triangles; each triangle is limited by three points (vertexes). No more than two triangles can share an edge (fig.70) (Skua-User-Guide).

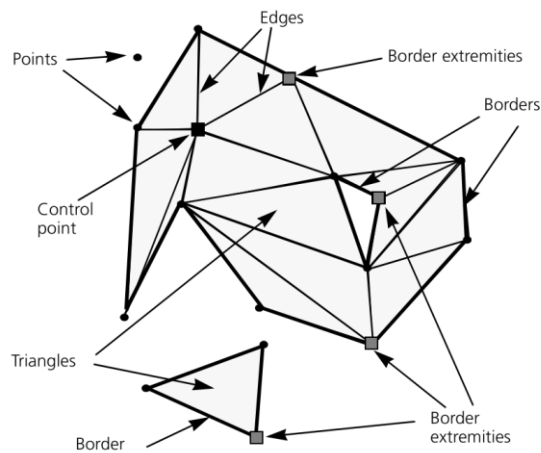


Fig. 70: The main characteristics of a surface (Skua-User Manual).

It is possible to create a surface in several way for example from point sets (point-set, point-set and curves, point set medium plane), from curves (close curves, two curve parts, borders...) or from existing surfaces.

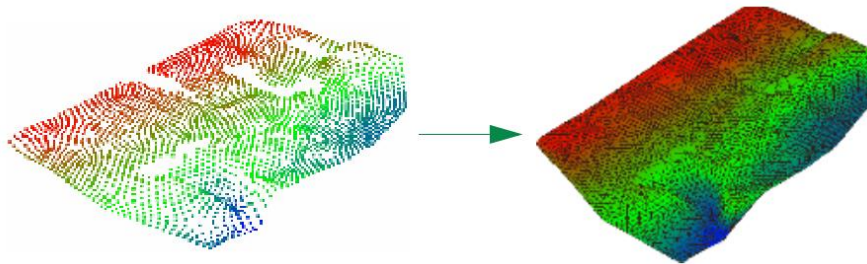
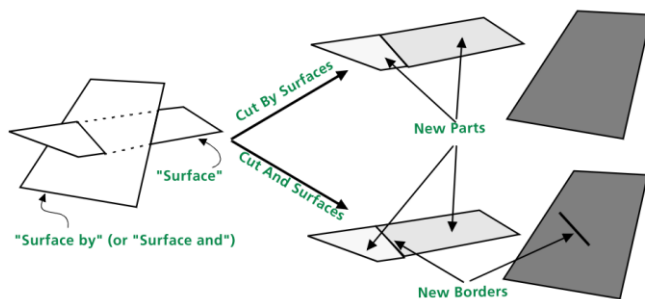


Fig. 71: A surface created from a pointset (Skua User Manual).

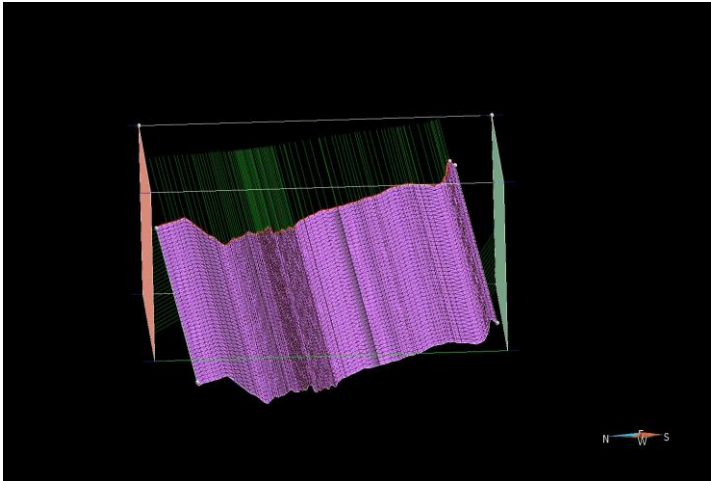


After the editing, the quality of the mesh can be improved working on the triangles forming it. In particular it possible to reduce the number of triangles, split them or

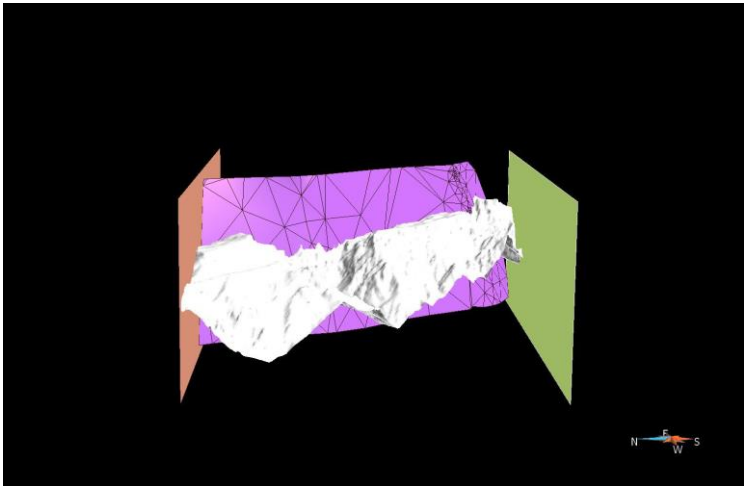
Fig. 72: A surface can be cut in several way (Skua User Guide).

beautify the mesh. Moreover, it is possible to change the position of the vertexes (point) of the triangles moving, translating or dragging them. If only one part of the surface must be improved or moved it is possible to select it creating a region. If a given surface is too long, it can be cut when it intersects another surface using the tool cut a “Surface by/and other Surface” or cutting “surface mutually among surface” (fig. 72).

If it is too short, it is possible to extend or move the surface borders. Another possibility is to set some constraints from the surface to a target surface (fig.73), (usually the bounding box of the model or another fault) after that the software can perform an interpolation that extend the surface following the direction of the constraints (fig.74).



*Fig.73: The surface (purple) has to be elongated and for this reason constrains (green lines) were setting going from the surface to the top of the model.*



*Fig. 74: The surface after the interpolation. Moreover, it was cut using the bottom surface of the model*

### 4.3.2.2 Structural and Stratigraphy workflow

The Structure and Stratigraphy workflow allows creating a structurally coherent model of the object, defining the geometric relationship between all the geologic boundaries. After all the contacts between faults and horizons are sealed, a geological grid can be realized.

Skua/Gocad Structure and Stratigraphy workflow is described in the following points (see Skua User Manual):

1. Creation of the stratigraphic column. It defines the stratigraphic order, relative importance and clipping relationship of the horizons in a model..
2. Assignment of geological features. All the data that will be used for the realization of the model must be assigned to a specific geological feature. For example a fault surface must be assigned to the feature *fault* and a surface representing a boundary between formations must be assigned to feature *horizon*.
3. Data selection. Here the data that will be used for the model are selected. Three main categories of data are comprised in the workflow: horizons, faults and seismic. The data available for building the model can be of several types (point sets, polylines, surfaces, seismic data etc.).

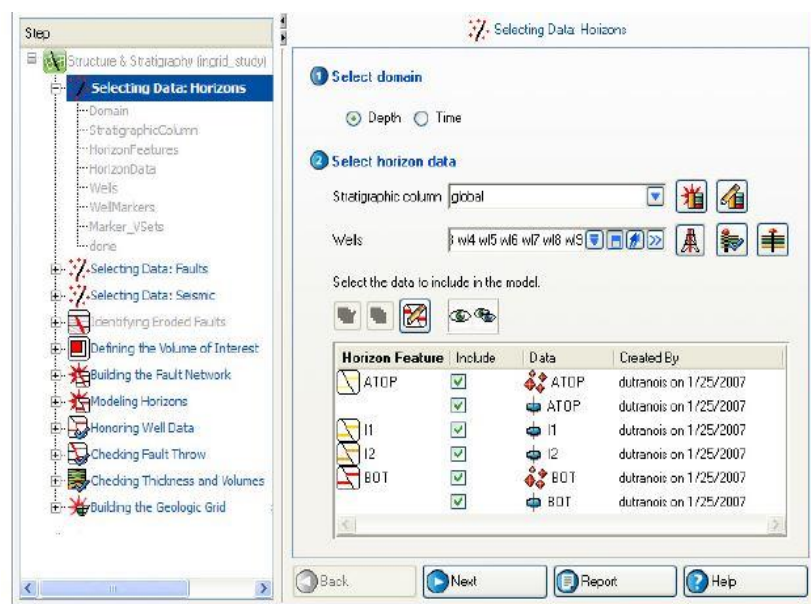


Fig. 75: The panel of Skua 2009 where the horizon data can be selected (Skua User Manual).

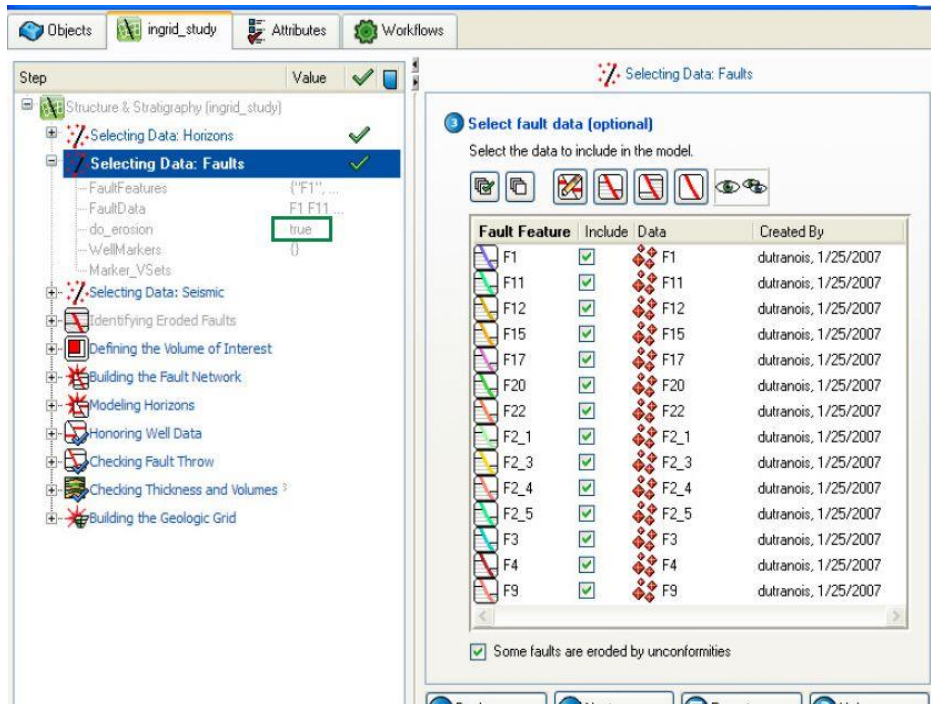


Fig.76: The panel of Skua 2009 where the fault data can be selected (Skua User Manual).

4. Definition of the volume of interest, (VOI). Here the 3D volume that will be considered in the modelling can be chosen. The VOI defines the space where the data will be used by the software. It should be defined making sure that it contains only the essential data in order to reduce the computation time.

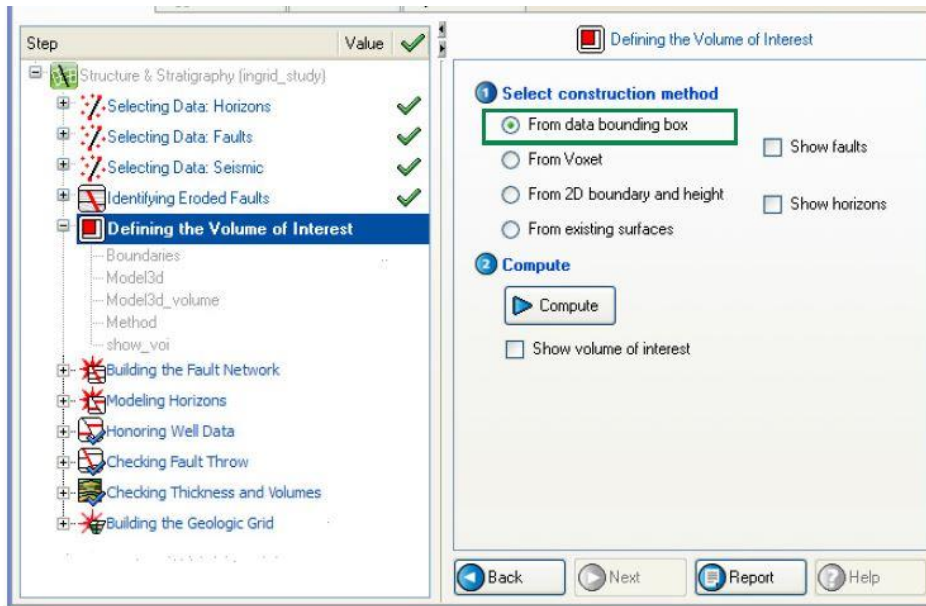


Fig.77: The panel where the VOI can be define.

- 5 Building the fault network. Here the fault network is created. The main result of this step is the subdivision of the original VOI in fault blocks. All the faults are generated simultaneously. It is possible to edit the faults once they have been generated. For instance, it is possible to define the type of contact between two faults (setting it branching, cross-cutting, etc.). When a change is made on a fault, all the fault network is updated. The resolution distance (distance between the points of each faults), the distance under which two faults must be connected and the degree of fitting with the data (smoothing) must be specified.

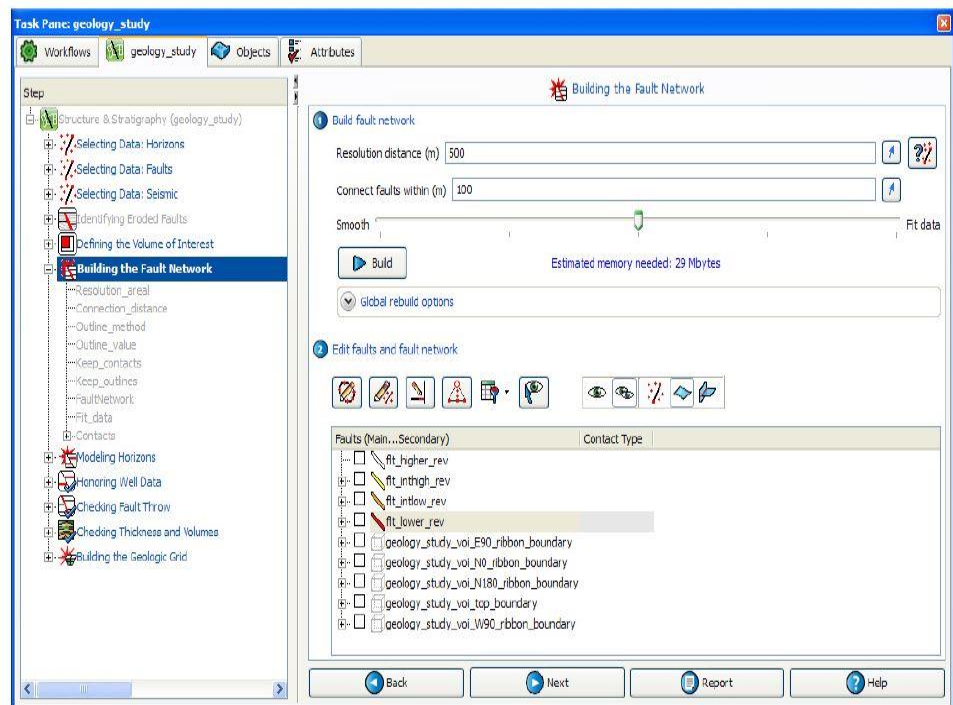


Fig.78: The fault network panel (Skua User manual).



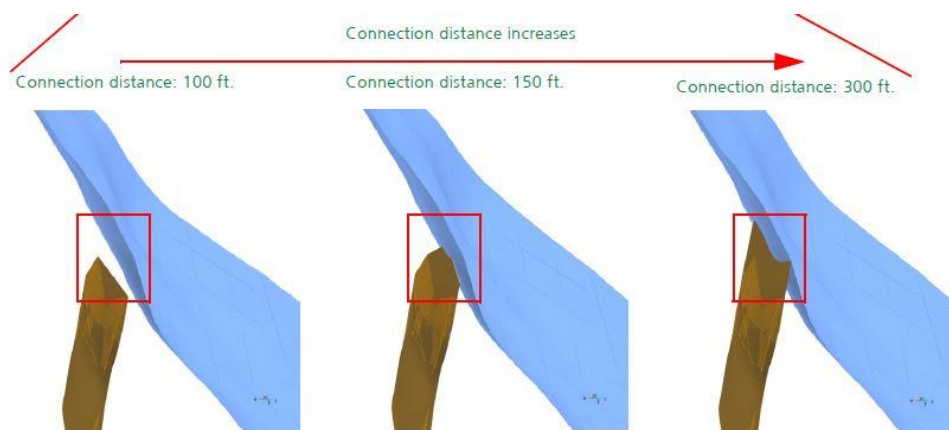


Fig. 79: The results give from three different connection distance (Skua User Manual)

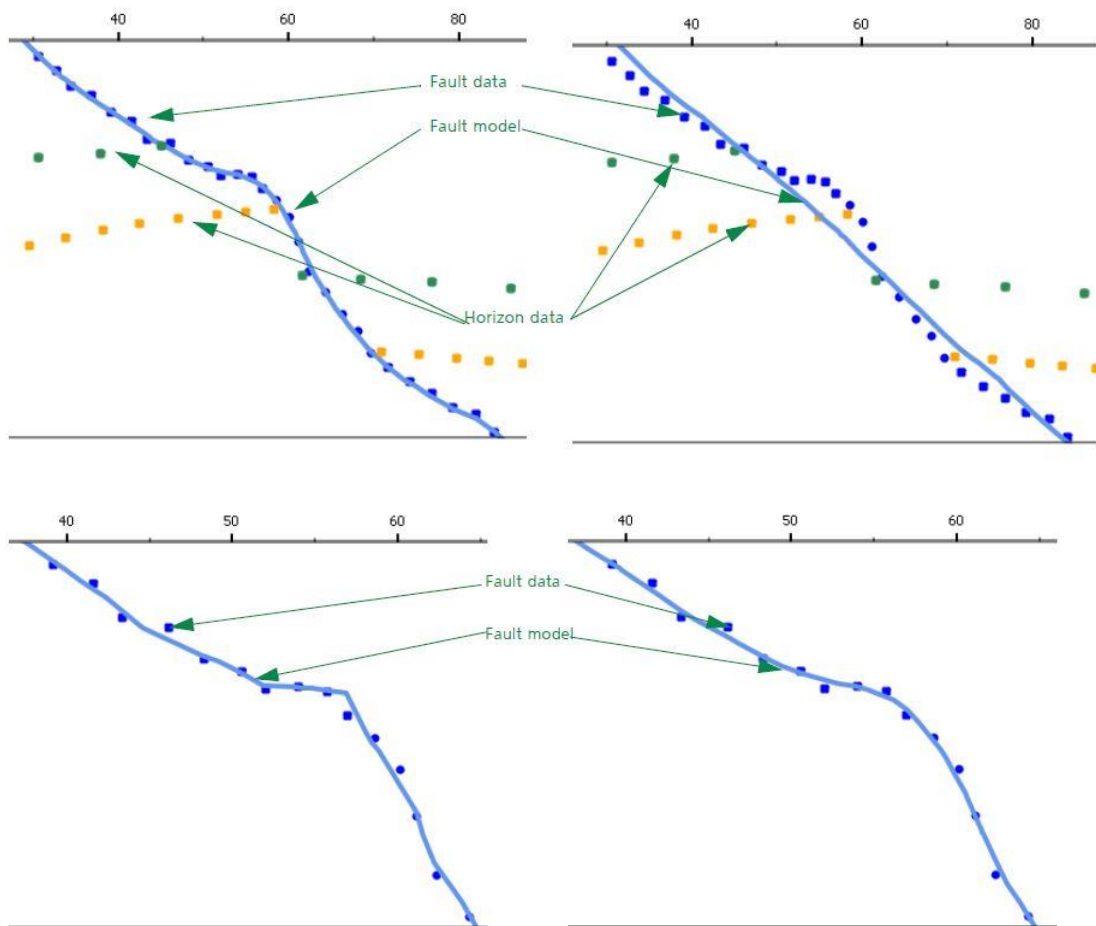


Fig.80: Two examples of different degree of smoothing (Skua User Manual).



- 6 Modelling of the stratigraphic horizons. As in the fault network building step, all the stratigraphic horizons are built at the same time, considering the input data, the stratigraphic relationships defined in the stratigraphic column and fault throws (if defined).

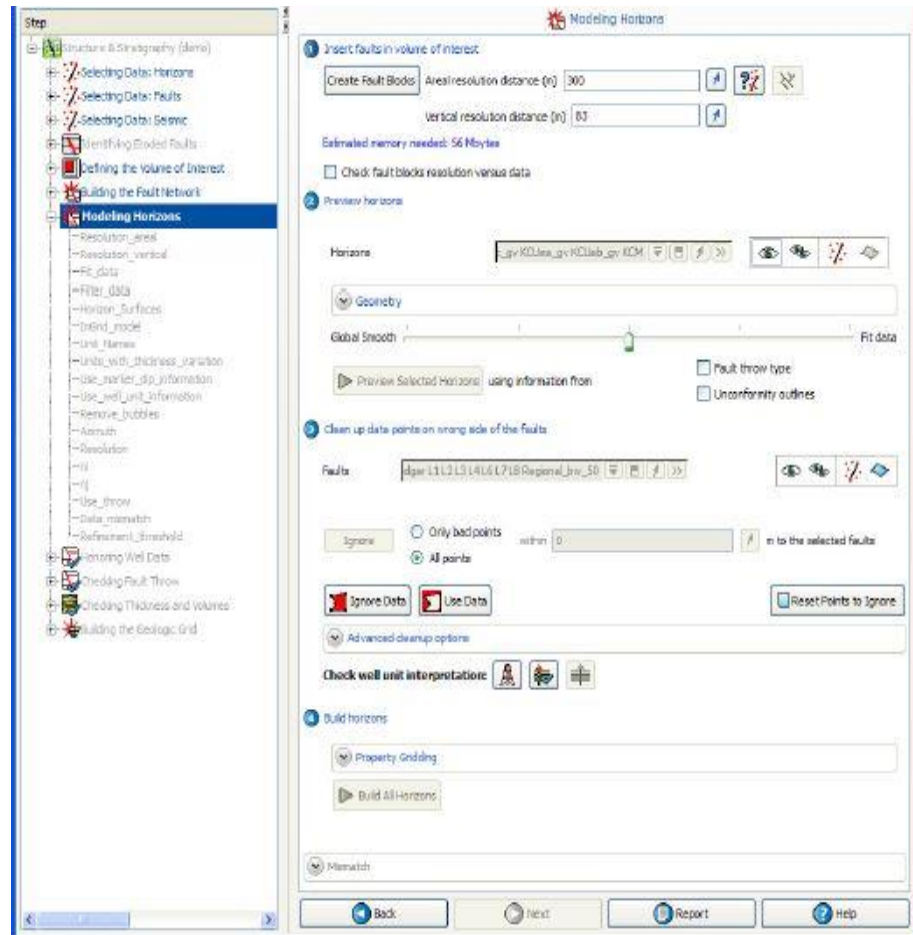


Fig.81: The modeling horizons panel (Skua user manual).

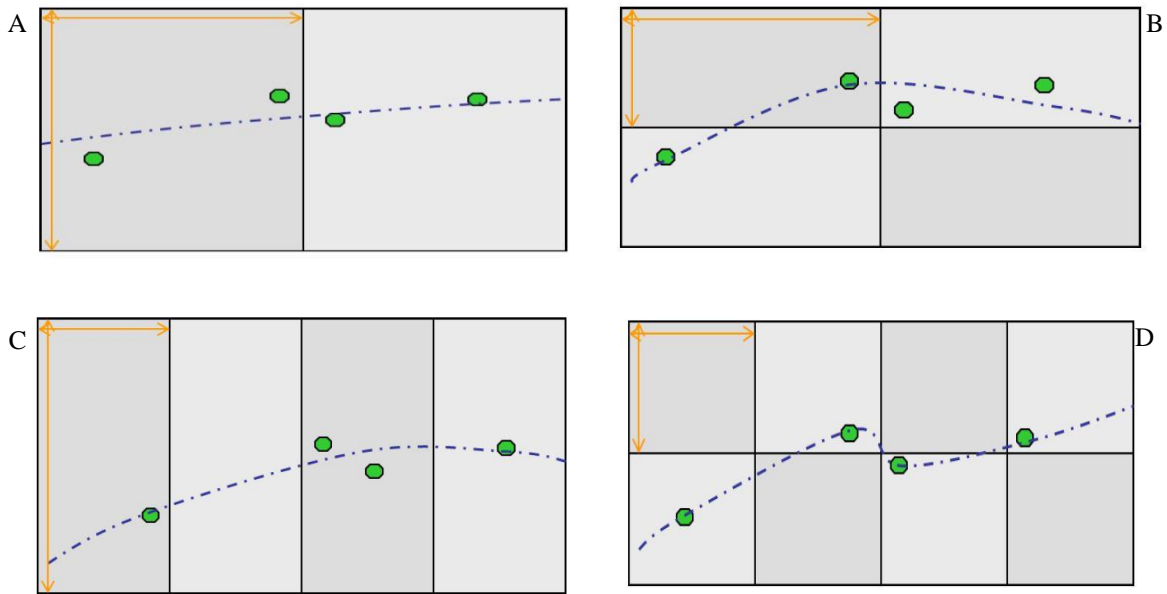
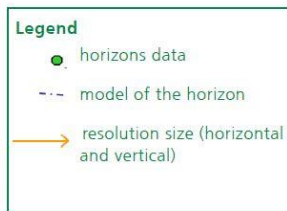


Fig. 82: Differences between coarse and fine horizontal and vertical resolution  
 Coarse vertical and horizontal (A), Coarse horizontal and fine vertical (B),  
 Coarse vertical and fine horizontal (C) Fine horizontal and vertical (D)  
 (Modified from Skua User Manual).

Usually, at this point a certain degree of editing is required. For this reason the workflow allows to first preview the selected horizon to check the consistency of the surface modelled by Skua and the input data. The most common problem is that, after the fault generation step, some of the input data (normally point) that should be used for the horizon modelling fall in the wrong fault block (fig.83).

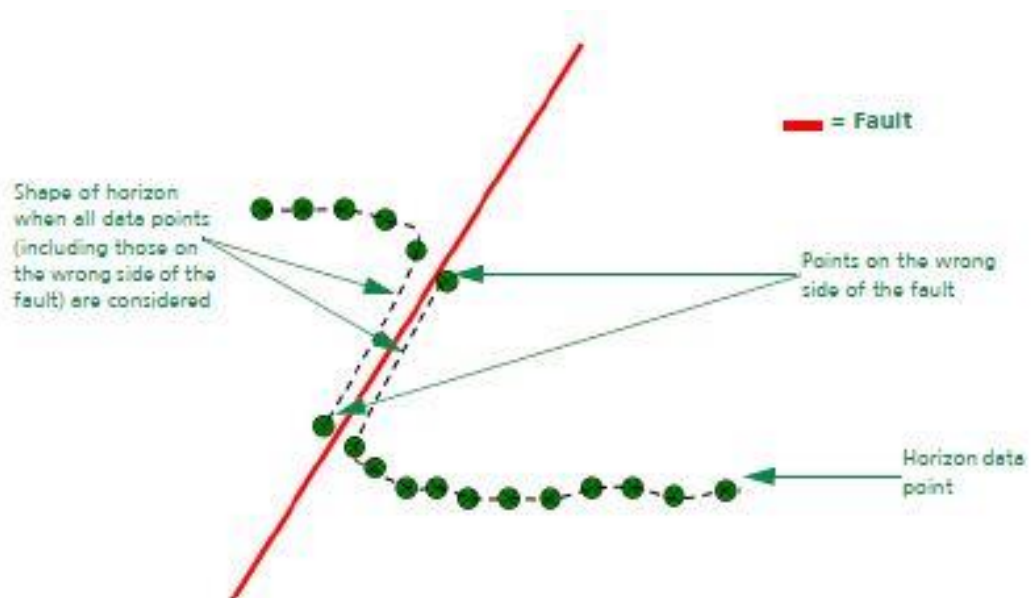


Fig. 83: Point on the wrong side of the faults create problem during modelling  
 (Skua User Manual).

Other sources of inconsistency in the horizons generation can be inconsistency between the fault throw type and the horizon data, wrong input data and resolution of fault blocks.

A number of editing options are possible to solve the mentioned issues. For instance, it is possible to modify the degree of fitting to the data. If low degree of fit is selected the horizons will tend to be smoother and may not always exactly follow the input data or all the way around (fig.84). It is possible to filter the data, in order to exclude a part of the dataset that may induce inconsistencies in the horizons (fig.85).

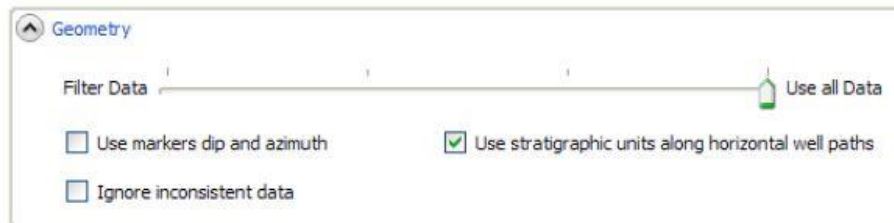


Fig.84: It possible to choose how smoothly the horizons are fit to the data.

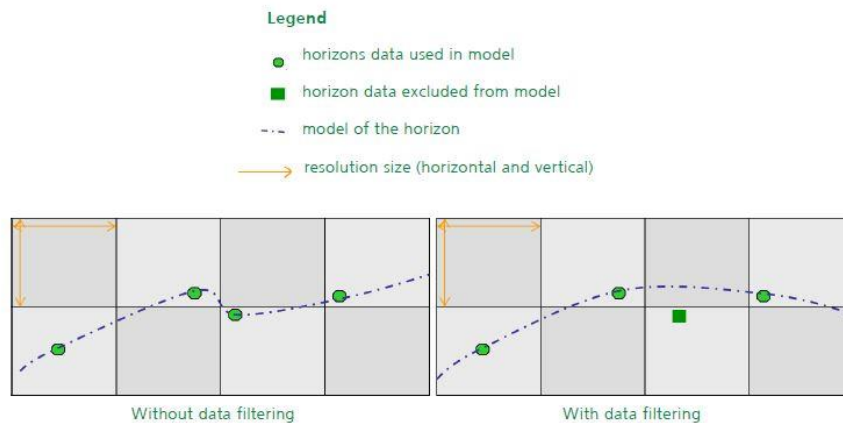


Fig. 85: A filter can be applied to eliminate bad data.

- 7 Honoring well data. This step is intended for the use of well data only, when available. It allows to improve the fit of the generated horizons with the well input data. In this thesis, no well data were used.
- 8 Checking and editing fault throw. In this panel the user can look for possible inconsistencies in the structural model by highlighting the displacement of horizons across the faults.

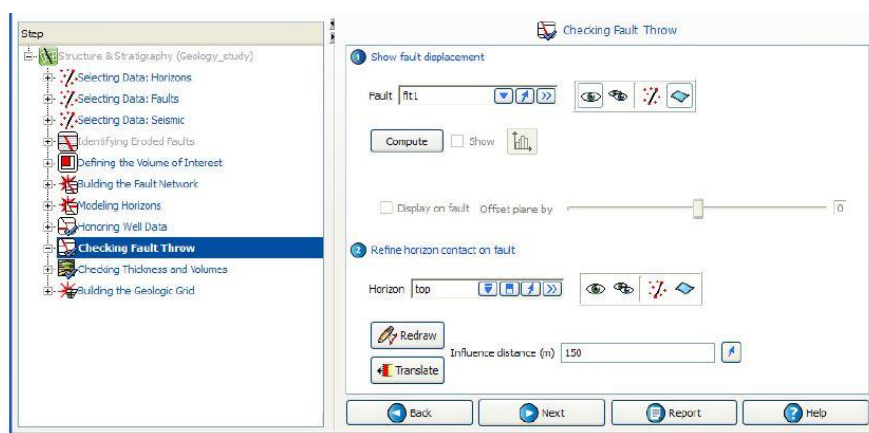


Fig. 86: Checking fault throw panel (Skua User Manual).

- 9 Checking stratigraphic thicknesses and volumes. In this step volumes and thickness maps of the modelled stratigraphy are computed. This information will be used in the generation of the geologic grid

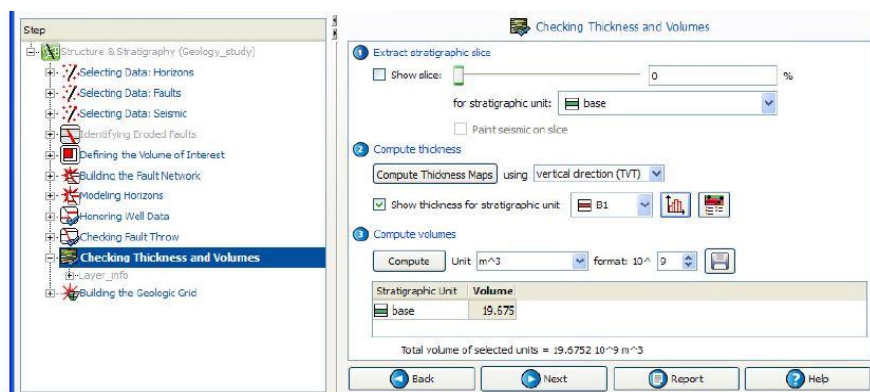


Fig. 87: Checking thickness and volumes panel (Skua User Manual).

10 Building the geological grid. In this last step of the workflow the geological grid is created using the information derived from the SKUA structural model. Volumes defined by faults and horizons are discretized into cells of user-defined size.

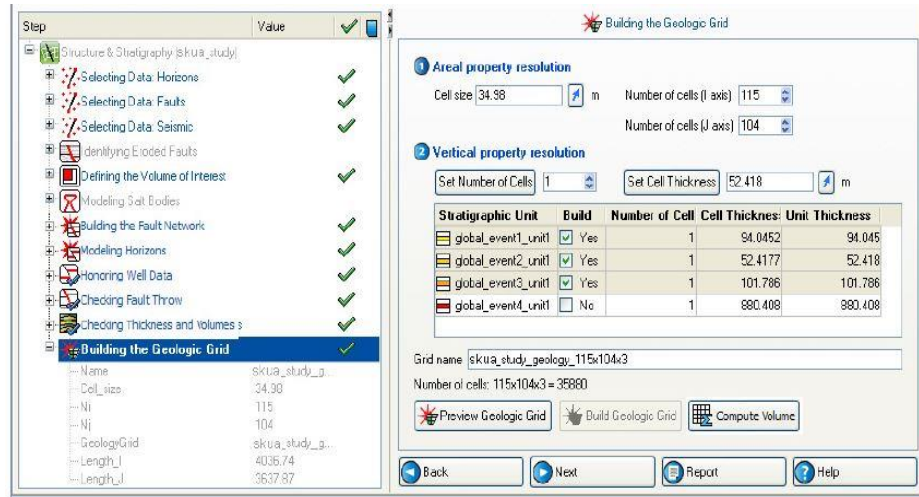


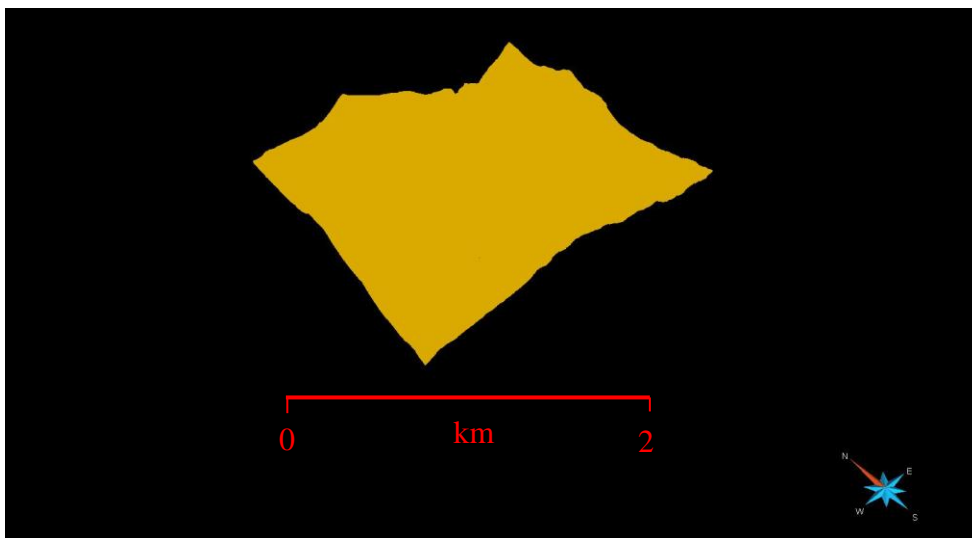
Fig. 88: The geological grid building panel (Skua User Manual).

### *4.3.2.3 Digitizing formation boundaries*

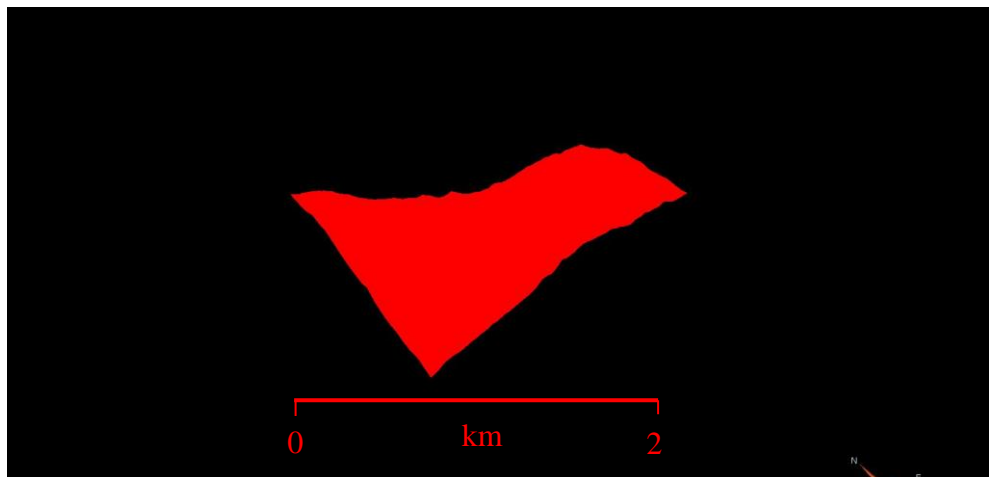
The 3D mesh of the LiDAR topography was uploaded in Skua to be used as a base to digitize relevant geologic features (unit boundaries and fault traces). In order to have the maximum possible precision in digitizing the features, the DTM was kept at the maximum possible resolution.

This process was performed on sheets 1605, 1606, 1607, 1628, 1629, 1630, 1649 and 1650 of the LiDAR DTM. Since loading the entire DTM altogether this operation was carried out on smaller regions that can be selected and isolated from the whole dataset.

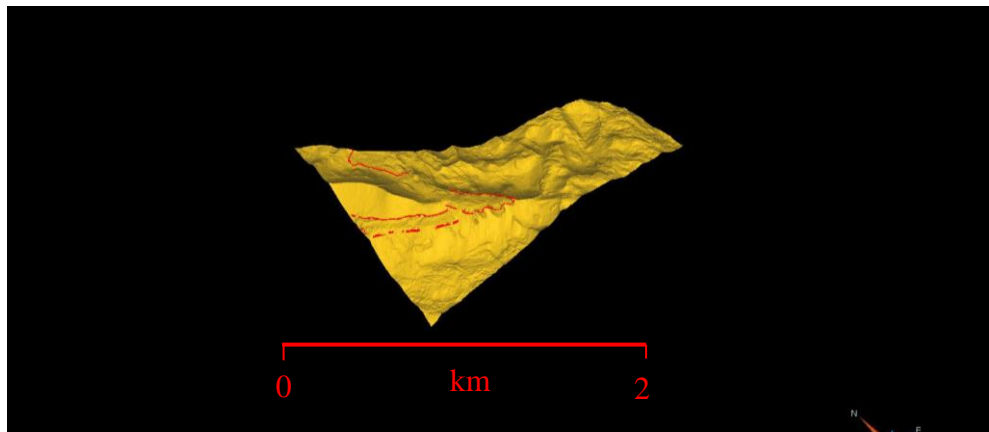
As an example, fig. 89 shows the complete point set of sheet 1630 while fig 90 shows the smaller region selected for the digitization. The 3D mesh generated from the region is shown in fig 91 with some formation boundaries digitized as polylines highlighted in red. .



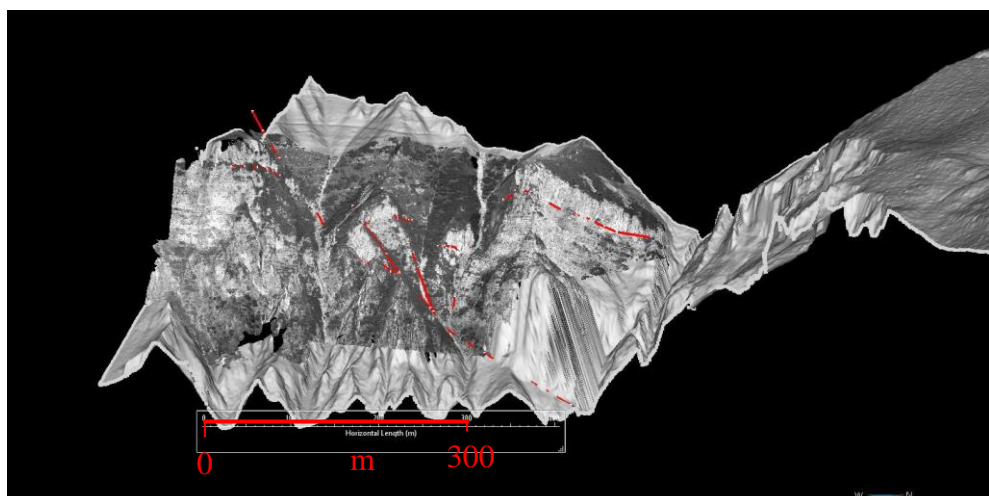
*Fig. 89: The complete point cloud of block 1630*



*Fig. 90:: The selected region*



*Fig. 91: The high resolution triangulated mesh obtained from the selected pointset region with the formation boundaries.*

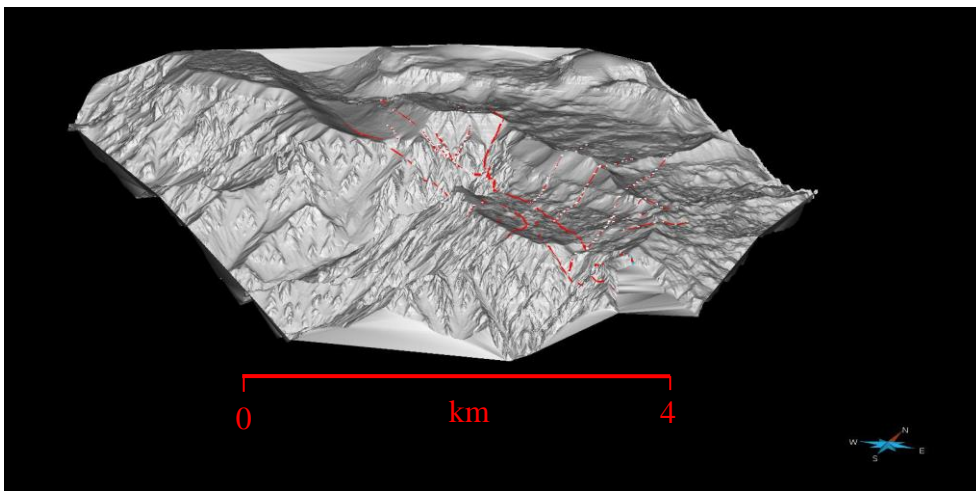


*Fig. 92: The 3D photogrammetric model integrated with the DTM with the formation boundaries*

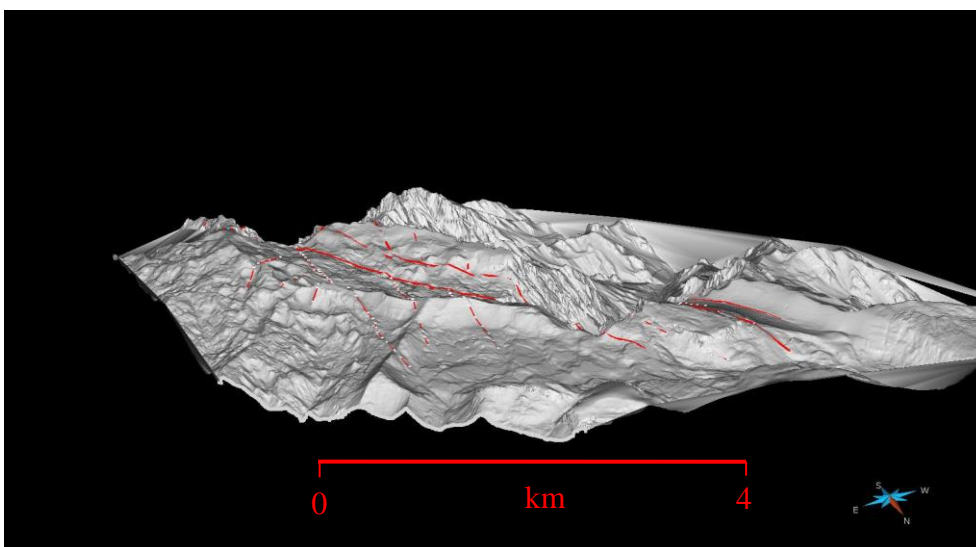


#### 4.3.2.4 Digitizing fault traces.

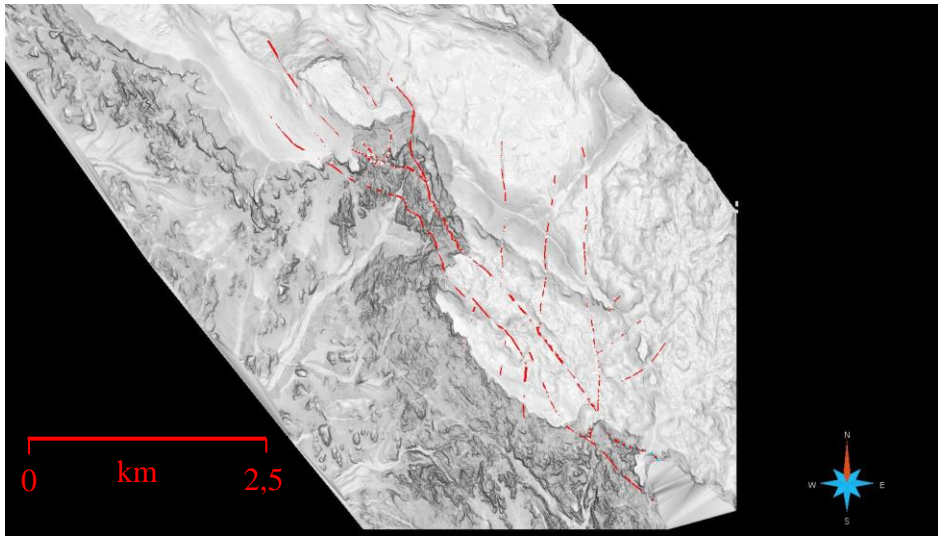
Fault traces were digitized as curves. As reference for this operation, the 3D polyline of the faults in the geological map (Chapter 2) was used. Since lower resolution was needed for tracing the faults, it was possible to carry out this operation on a complete low-resolution 3D mesh of the area (fig. 93, 94, 95). Where necessary, fault traces imported from the geologic map were modified to better fit the three dimensional topography.



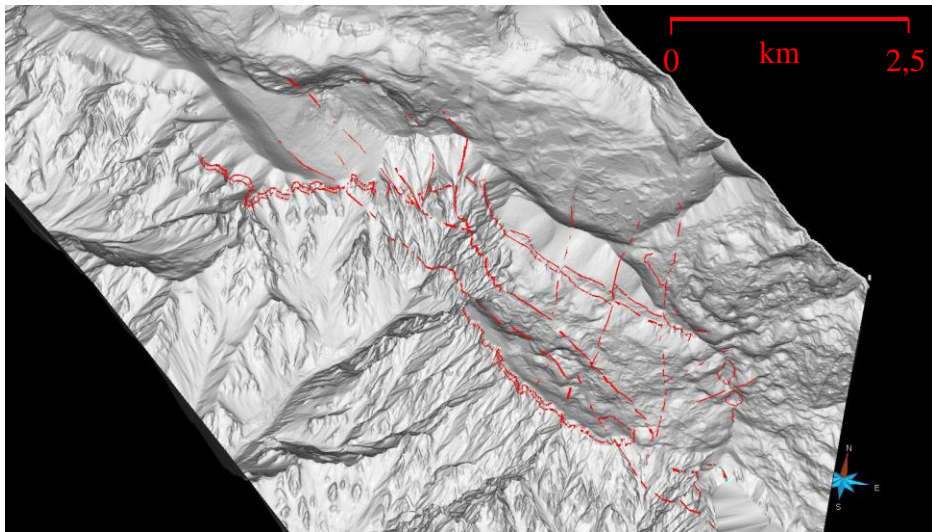
*Fig.93: The DTM with the faults traces (red) view from SE*



*Fig.94: The DTM view from NE*



*Fig.95: The DTM and faults lines view from top*



*Fig.96: The DTM with faults and formation boundaries (SE view).*

#### 4.3.2.5 Creation of the bounding box

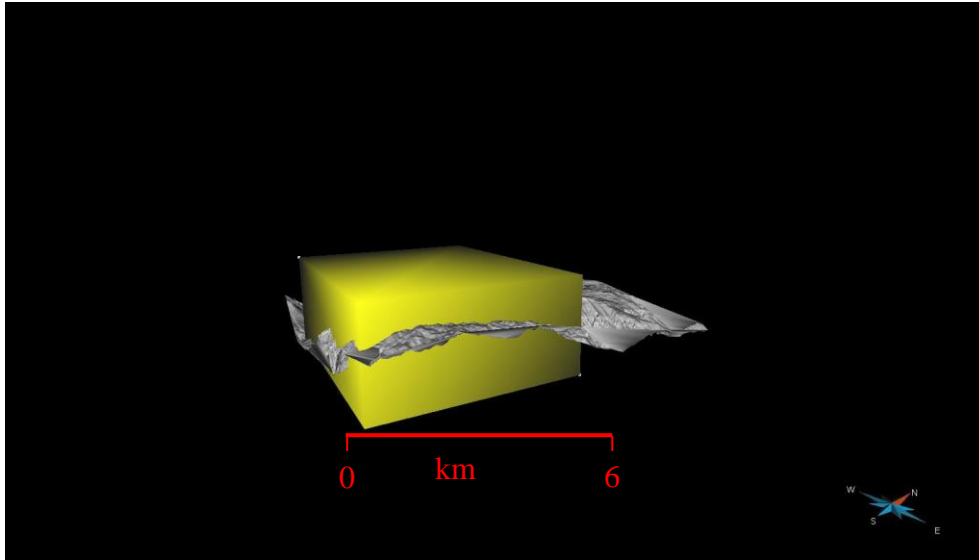


Fig.97: The bounding box created to define the boundaries of the model

#### 4.3.2.6 Generation of fault surfaces

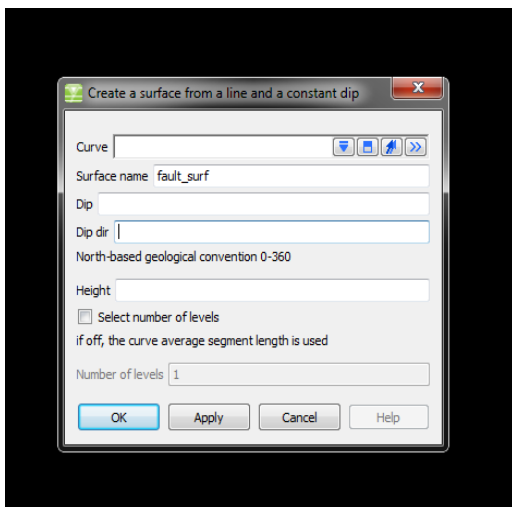
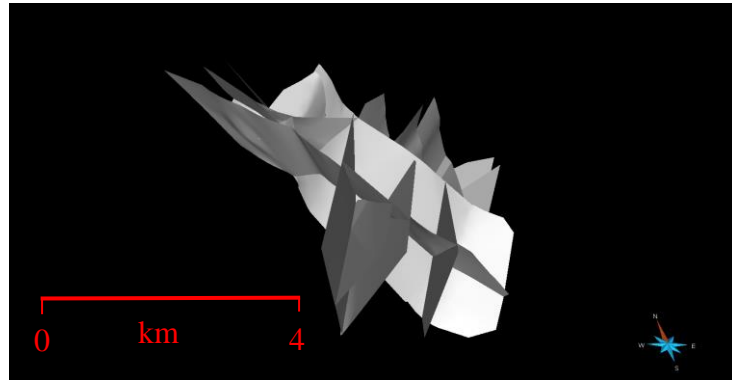


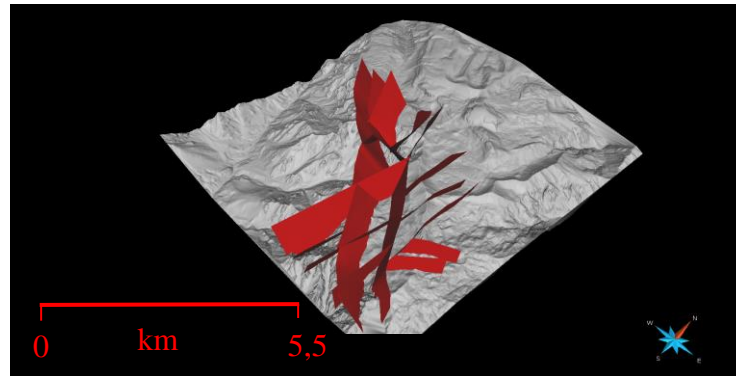
Fig. 98: The Geological toolbox

As the digitized fault traces alone did not permit to create fault surfaces consistent with field structural data by simply generating a surface that fits them, the Geological toolbox was used. This tool allows creating fault surfaces using both polylines and dip values. In particular, as highlighted in fig. 98 dip and dip direction of the fault must be

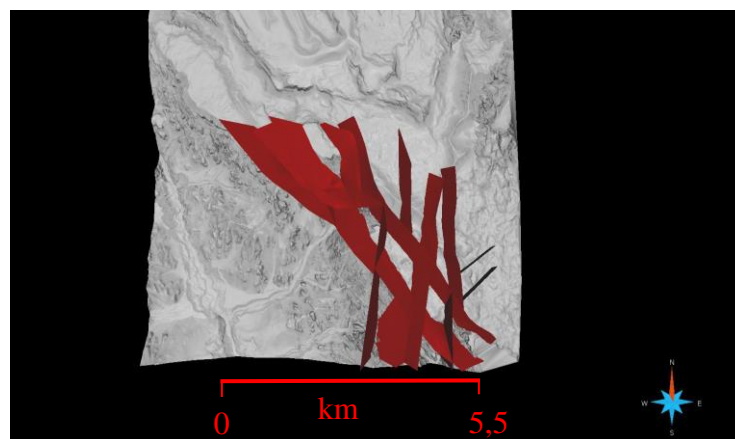
specified. This information derived from the structural analysis described in chapter 2.2. This procedure was applied to model all the relevant faults mapped in the study area. Results of fault modelling are shown in fig. 99, 100, and 101.



*Fig. 99: The edited fault network view from S*



*Fig. 100: The fault network view from SE*

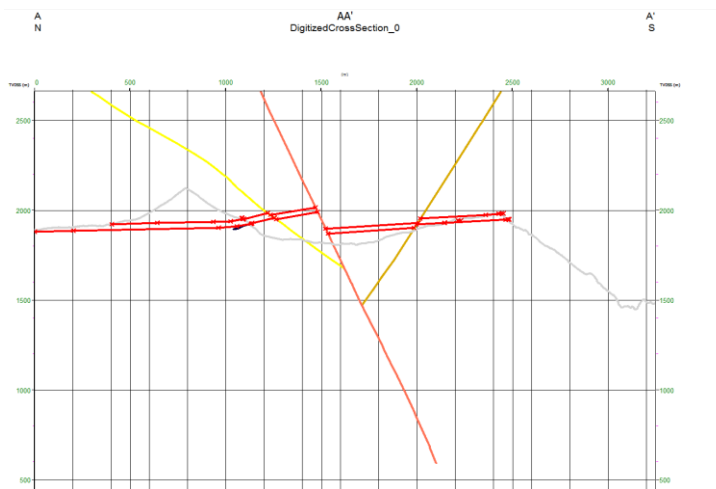


*Fig. 101: The fault network view from the top*

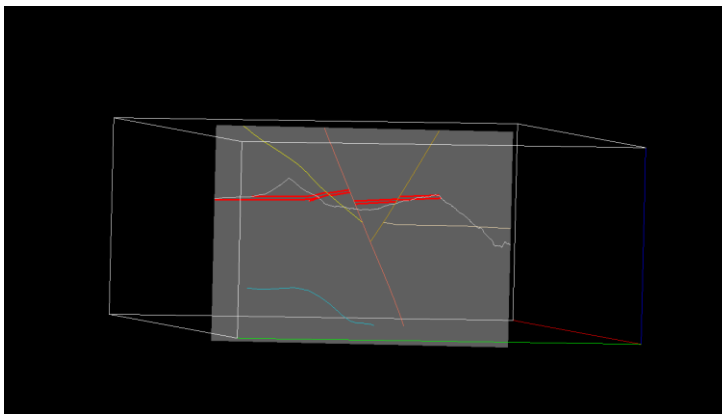
#### 4.3.2.7 Generation of horizon surfaces.

The 3D horizons comprised in the Monte Testa structure model are, from top to base the top of the Rotzo formation, the Loppio/Rotzo boundary, the Monte Zugna/Loppio boundary and the Dolomia Principale/Monte Zugna boundary.

The correspondent horizon surfaces were generated using polylines digitized both on the 3D topography and on cross-sections. Cross sections were drawn using Skua specific tool (fig 102, 103).



*Fig. 102: An example of a cross section created for this work using the tool of Skua*



*Fig. 103: The cross section of fig. 102 visualized in the 3D viewer.*

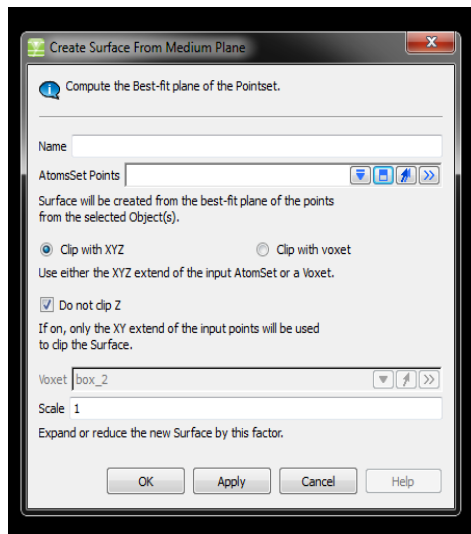


Fig. 104: the pointset medium plane tool

A first 3D reconstruction of the horizon surfaces was realized by using the “create surface from pointset medium plane” tool. This tool generates a 3D plane that fits the selected point-sets.

The most widely outcropping formation boundary is the Monte Zugna/Loppio boundary. The corresponding 3D horizon surface was modelled separately in each fault block defined by the fault surfaces.

To obtain better constrained surfaces at least one cross-sections was drawn across each fault-block. In this way of each fault-bounded portion of the horizon was constrained by the boundary polyline digitized on the topographic base and by polylines traced on the correspondent cross-section. In total 28 cross sections were drawn across the study area. Each fault-bounded portion of the modelled horizon had perfectly sealed contact with the faults. This was achieved by extending each horizon portion across the surrounding faults and then using the “mutual cut among surfaces tool” to cut the horizon surfaces.

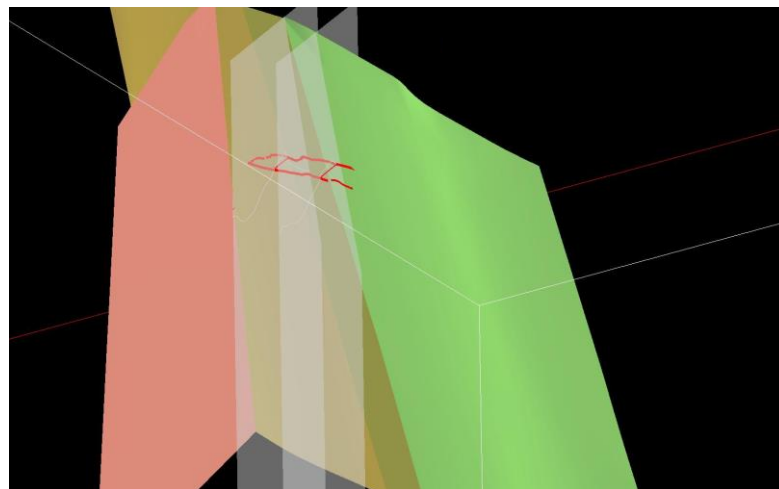
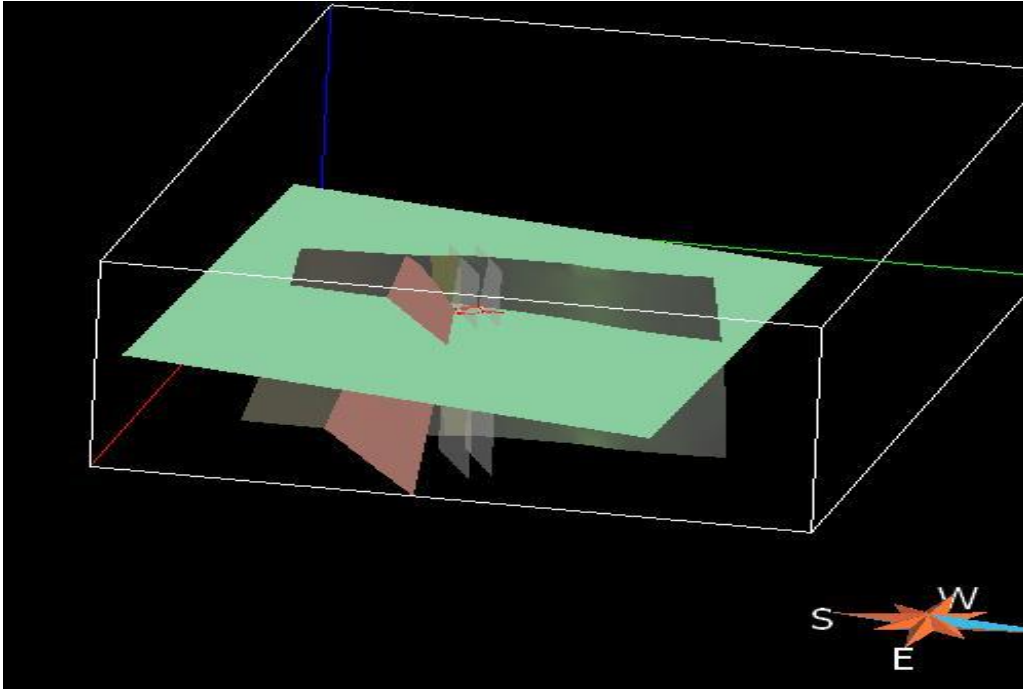
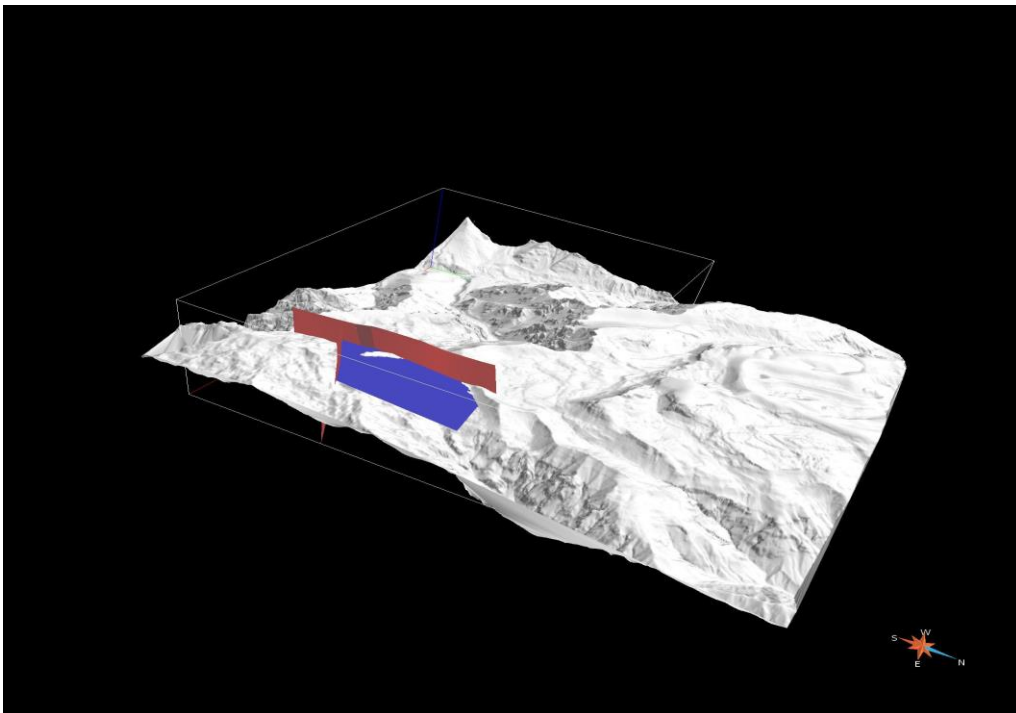


Fig. 105: The first step for the horizon modelling. We can see three fault surfaces and the curves (red) of the limits and cross sections.

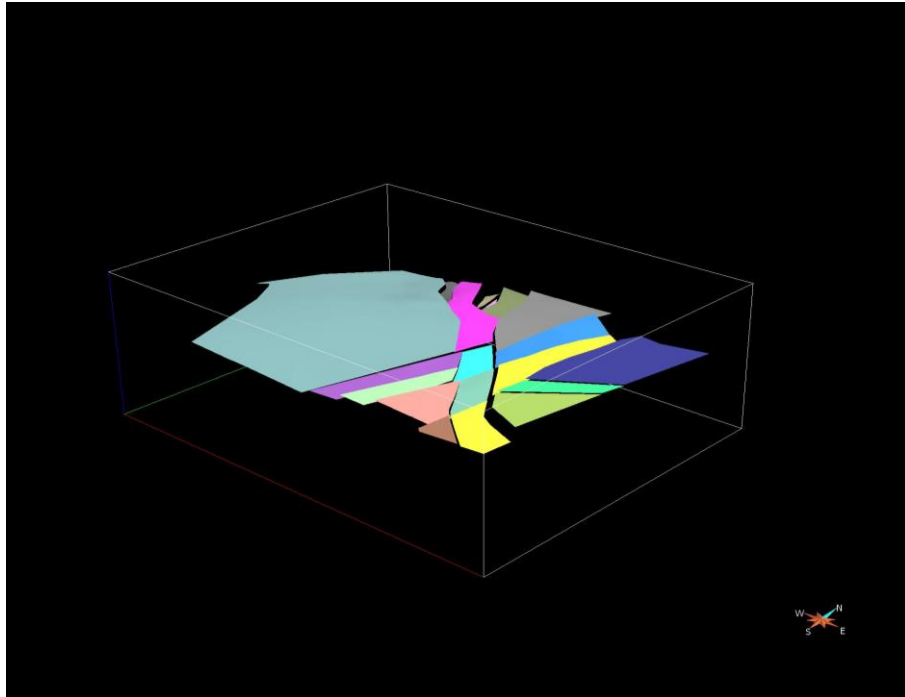




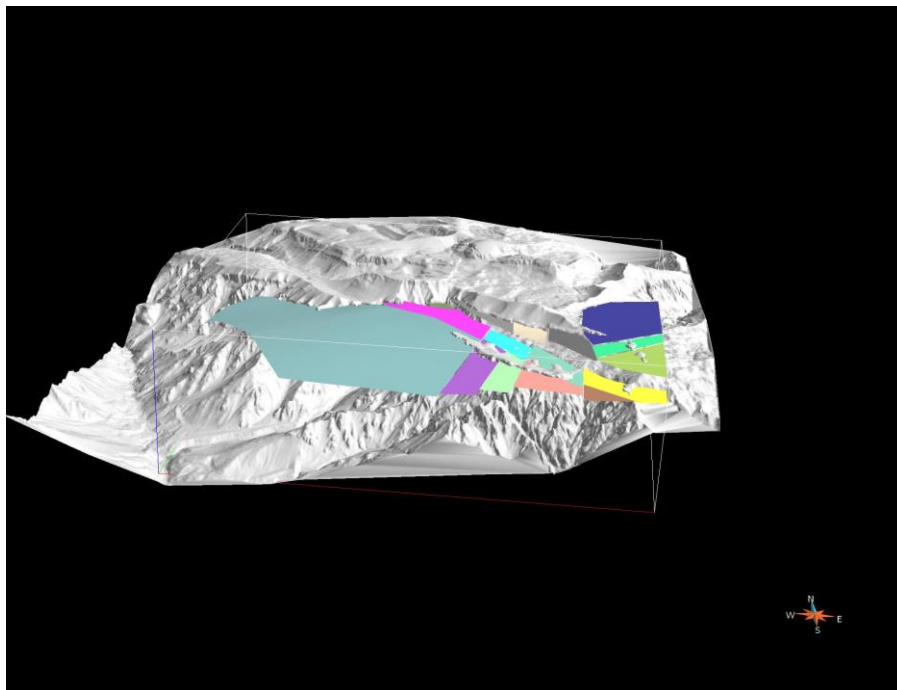
*Fig. 106: The horizon surface created using the "pointset medium plane" tool*



*Fig. 107: The last step: the horizon is cut against the three faults that define the block*



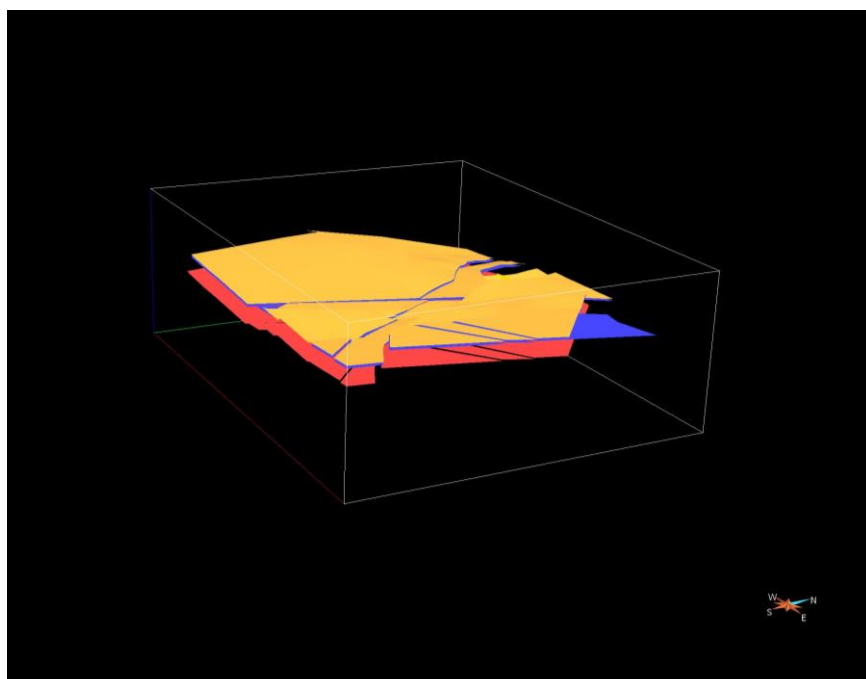
*Fig. 108: All the other surface are edited using the same process. Here we can see the complete surface forming the Zugna-Loppio horizon*



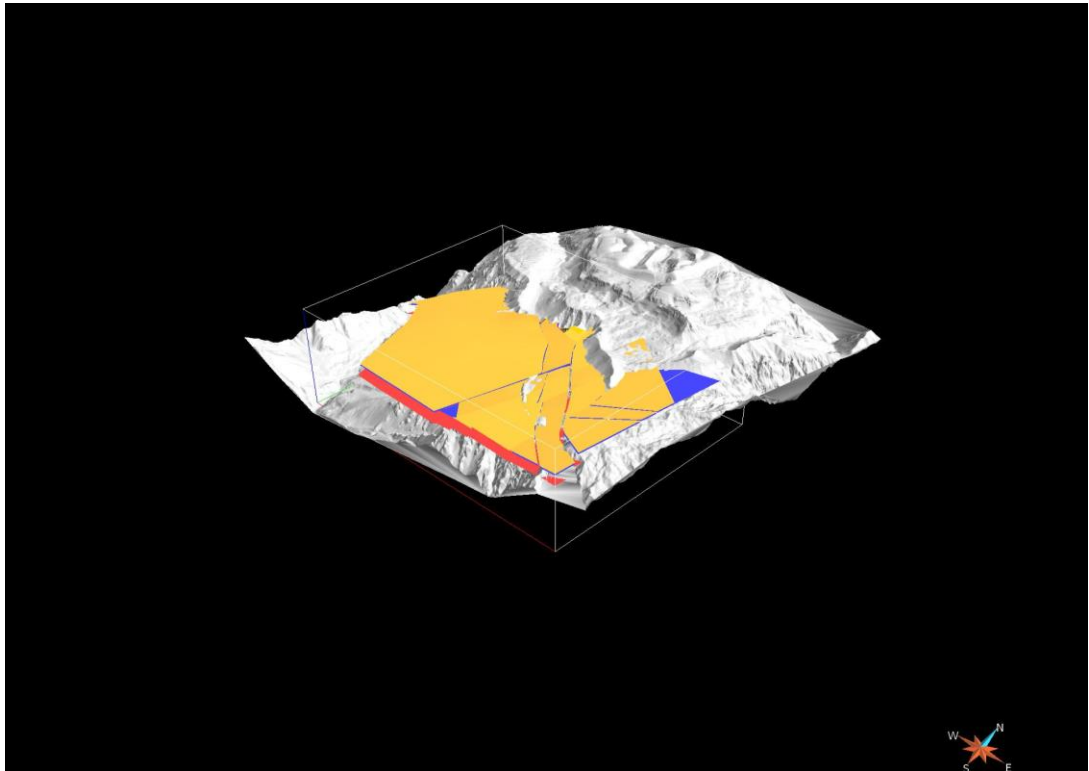
*Fig. 109: The Zugna-Loppio horizon with the DTM*

The Loppio/Rotzo boundary outcrops less continuously in the study area. For this reason, this horizon was modelled on the basis of stratigraphic considerations. Since the thickness of the Loppio formation is approximately 30 m throughout the mapped area its base was modelled by copying the Monte Zugna/Loppio surface parts and translating them up of 30 meters (fig.110).

A similar approach was used for the base of the Monte Zugna formation (Dolomia Principale/Monte Zugna boundary) because it is difficult to recognize and cannot be traced on the 3D topographic base (see Chapter 1). The correspondent horizon was modelled by translating vertically (along the z axis) a copy of the Monte Zugna/Loppio horizon. The translation was of -200 meters (fig.110) that correspond to the average thickness of the Monte Zugna formation in the area.

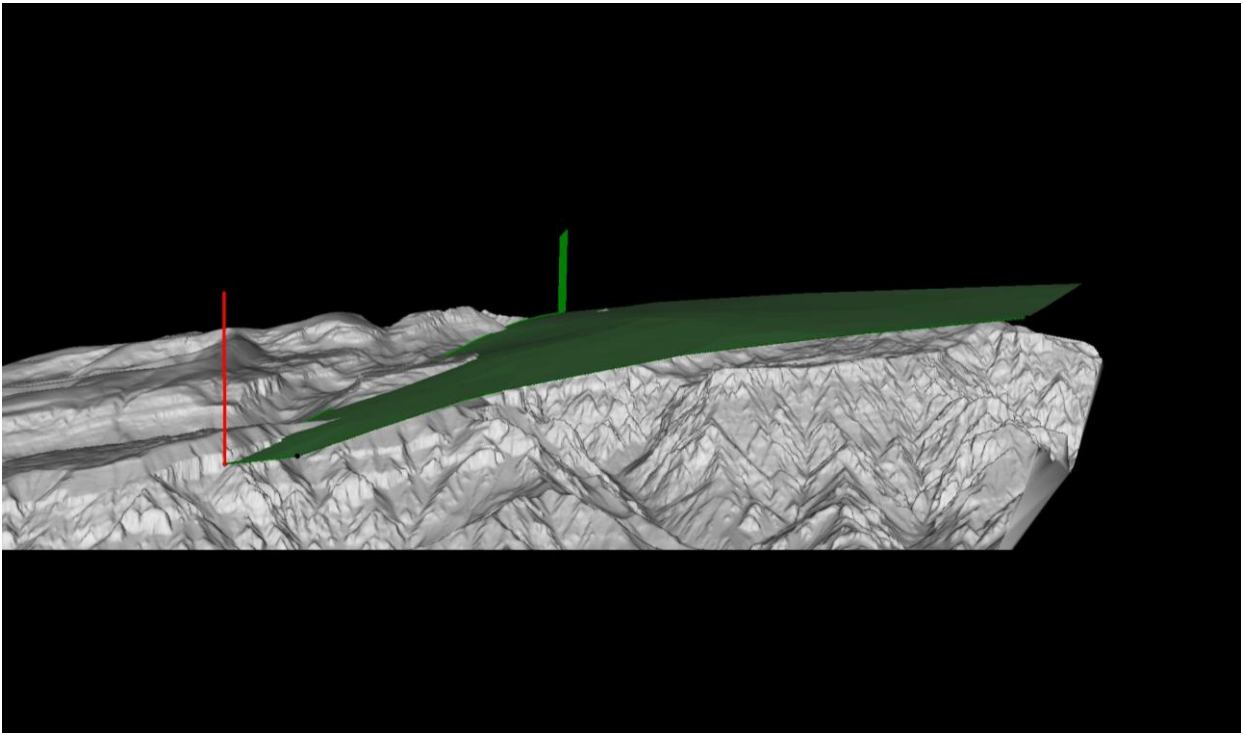


*Fig. 110: The three horizons representing the formation boundary. Lower boundary of Monte Zugna (red), Monte Zugna-Loppio (blue) and Loppio-Rotzo (yellow).*

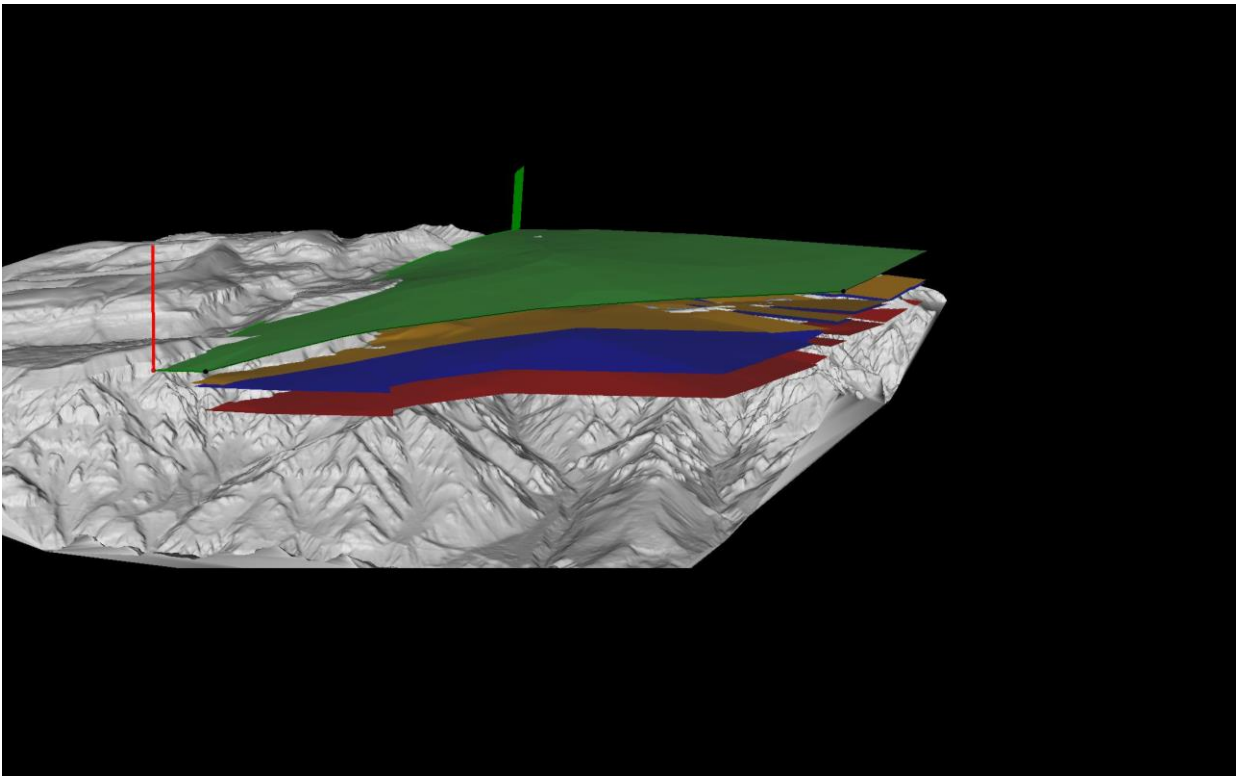


*Fig. 111: The three horizons with the DTM*

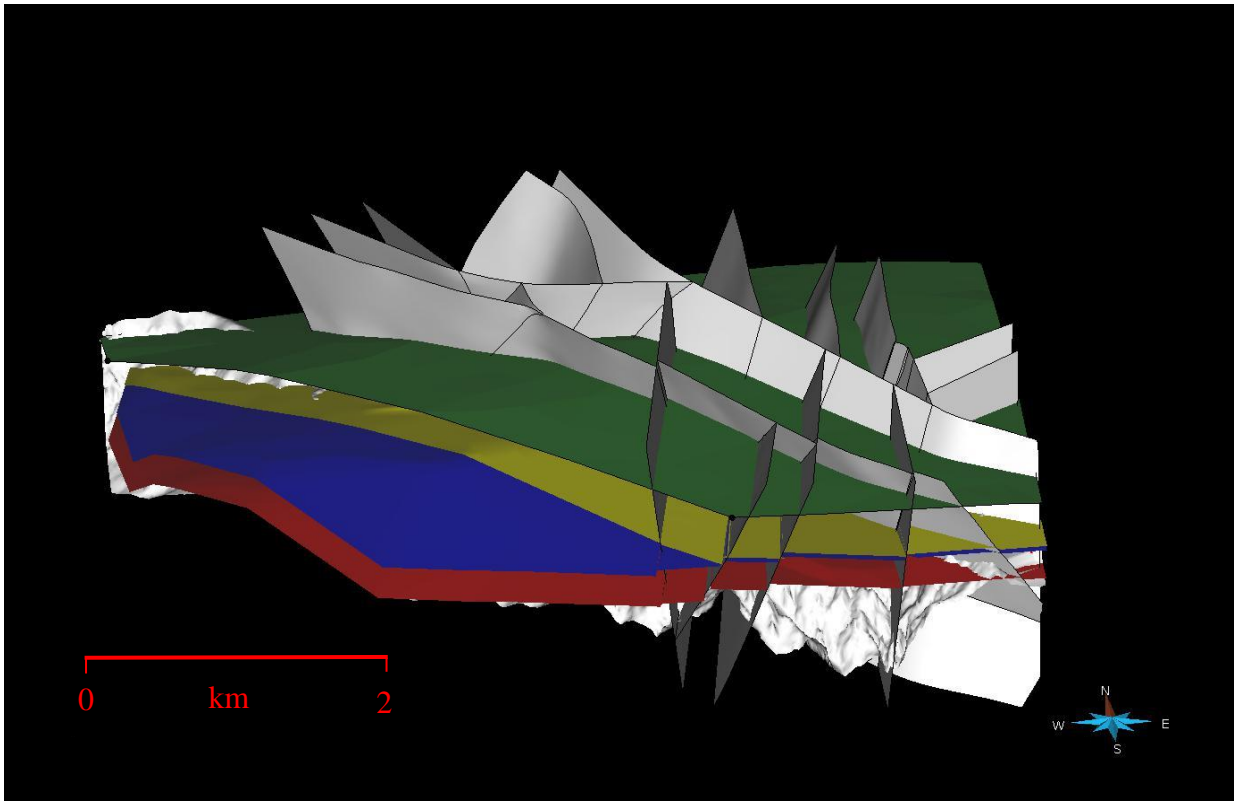
The last horizon surface to be modelled was the top of the Rotzo Formation. This formation was not affected by Jurassic tectonic during the last part of its deposition and that its upper part seals the Jurassic normal faults of the Monte Testa synsedimentary structure, however it is gently folded by the Alpine tectonics. The top surface of the model was reconstructed by selecting a layer not interested by syn-depositional deformation and modelling it in 3D following the regional attitude variation in the area of interest (fig.112).



*Fig. 112: The top boundary of the Rotzo Formation. The surface has been bent in order to follow the fold shape*



*Fig.113: The four boundary formation horizons*



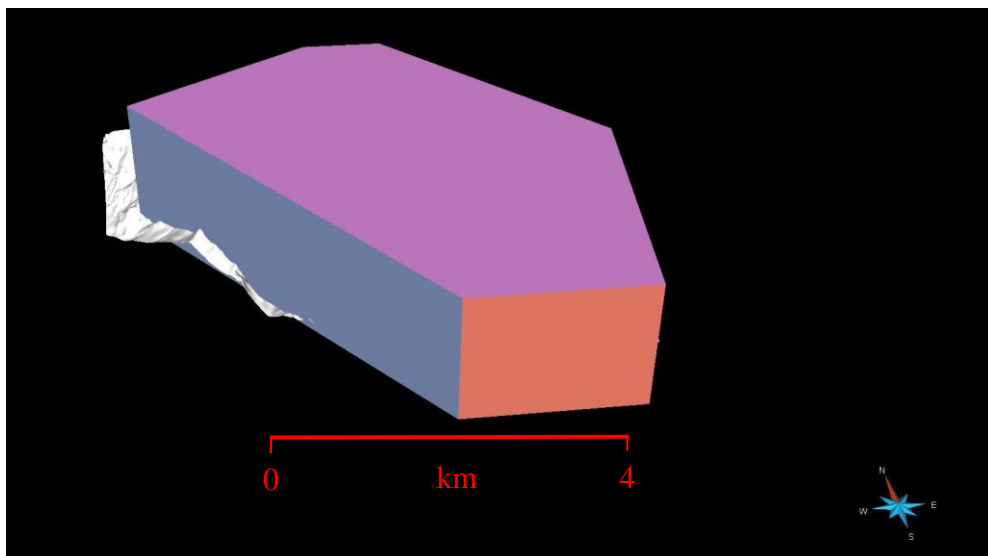
*Fig. 114: The complete structural model*



#### ***4.3.2.8 Modelling the Monte Testa structure in the Structural and stratigraphy workflow***

Once all faults and horizons were modelled it was possible to enter the Structure and Stratigraphy workflow with the final goal of producing a geologic grid of the Monte Testa synsedimentary structure.

The grid was realized considering a VOI that comprises only the relevant elements of the model (fig 115).

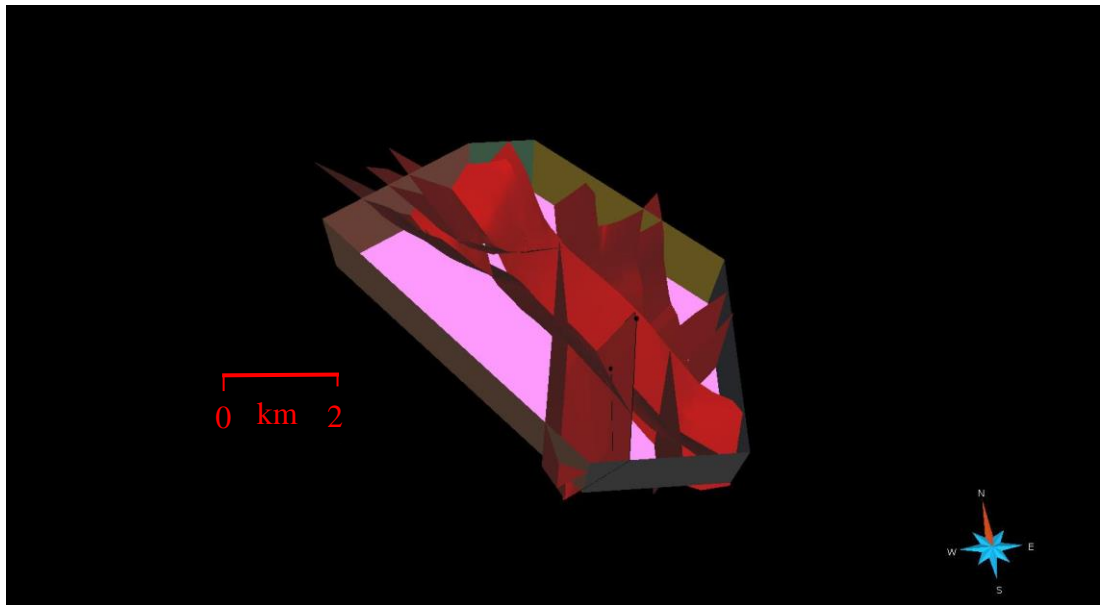


*Fig.115: The VOI used in this work*

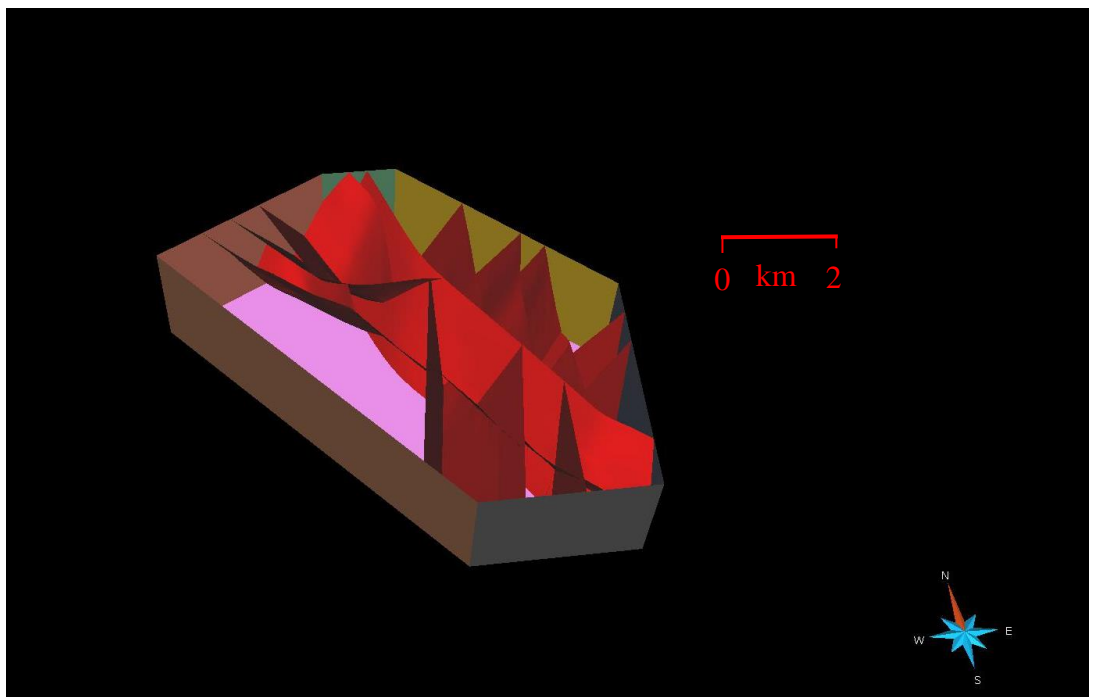
The general aspects of the Structure and Stratigraphy workflow are described in Chapter 4.3.

After creating a stratigraphic column, the horizons and faults, whose modelling was described in the previous paragraph, were selected as input data.

The fault network was created with a resolution distance of 50 meters. All faults of the fault network were extended to the bounding box and, where necessary, the faults were edited to obtain perfectly sealed contacts. The workflow automatically cut the input data within the volume of interest and connected the fault in order to obtain perfect sealed fault contacts.

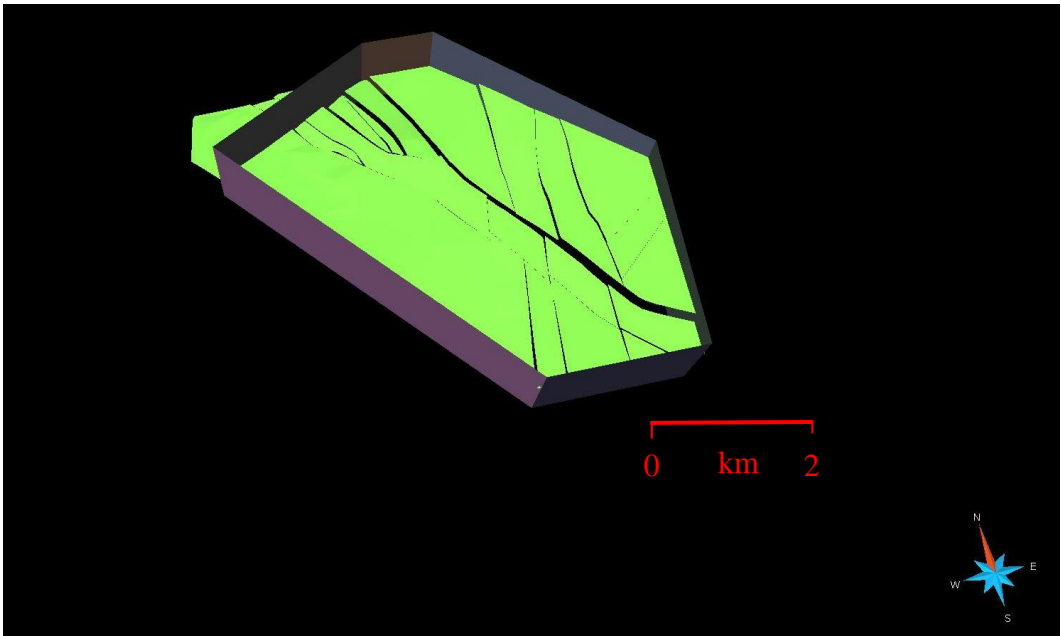


*Fig. 116: The fault network input data*

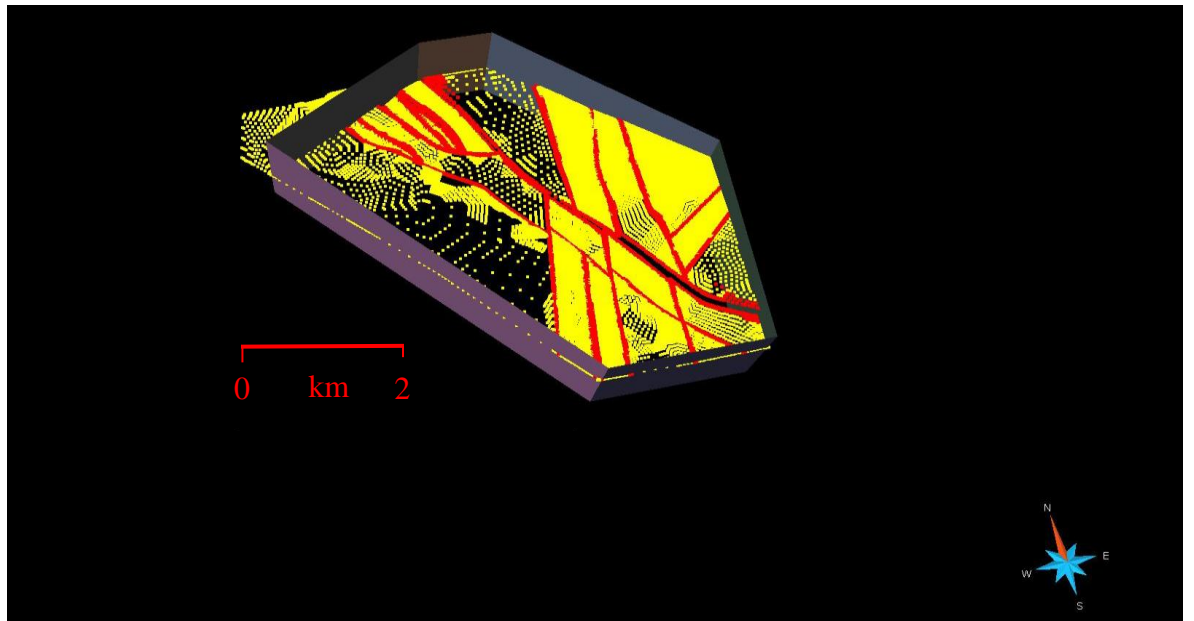


*Fig. 117: The final fault network. We can see that the faults are cut within the VOI.*

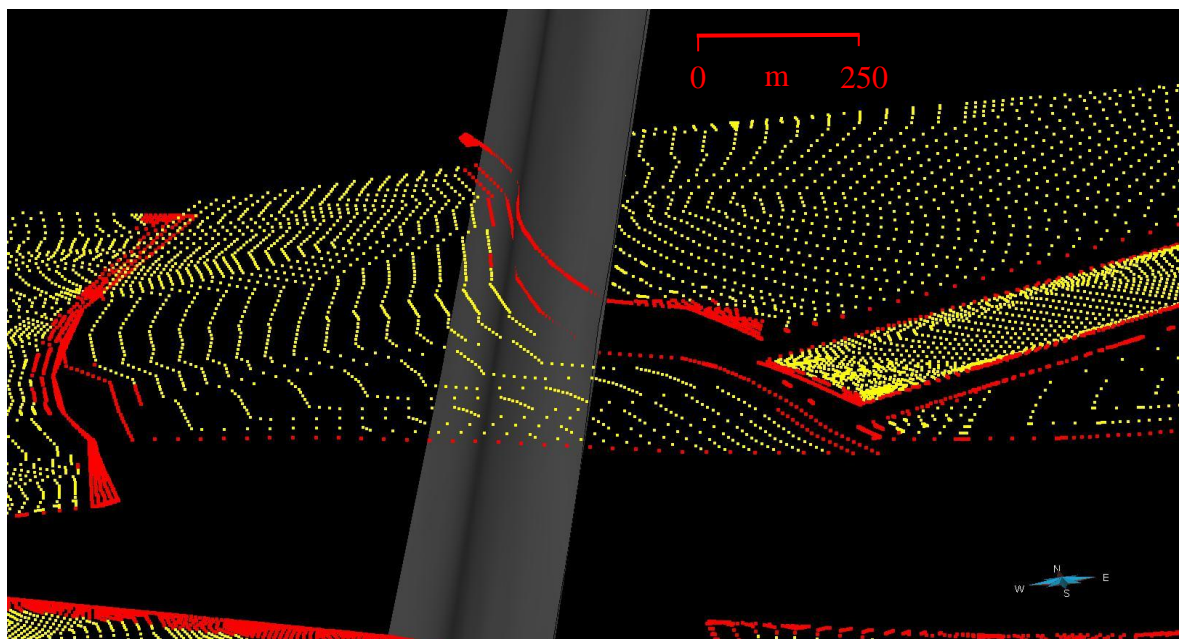
After creating the fault network, the fault blocks were generated with an areal resolution distance of 50 meters and a vertical resolution distance of 29 meters. Horizon surfaces preview revealed inconsistencies that derived from points located on the wrong side of the faults. These “*bad points*” were individuated and removed with careful manual editing and by putting fault-distance constraints that excluded points located at distances from faults smaller than a defined threshold (Fig.119 and 120). This time consuming operation assured the generation of perfectly consistent stratigraphic horizon surfaces (Fig.121).



*Fig. 118: The input data for the Horizon modelling process*



*Fig.119: The surface visualized as pointset (yellow) and the selected bad points in red*



*Fig. 120: Here it is possible to see the bad points (red) located on the wrong side of the fault (grey)*

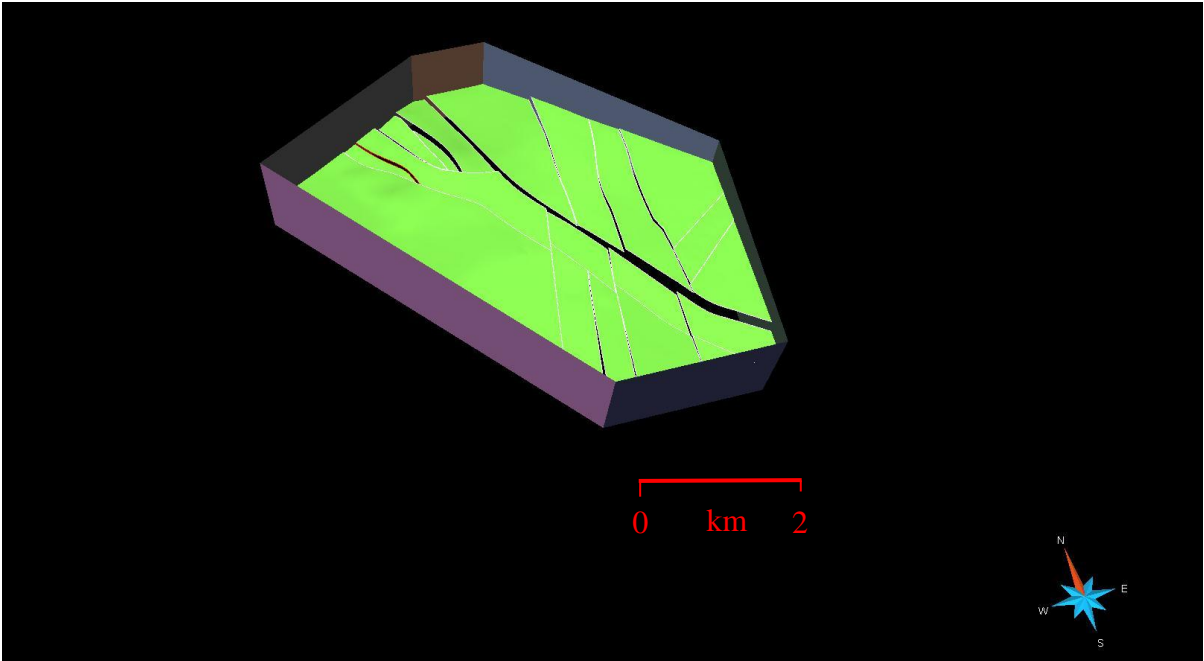


Fig. 121: The finale horizons cut within the bouding box

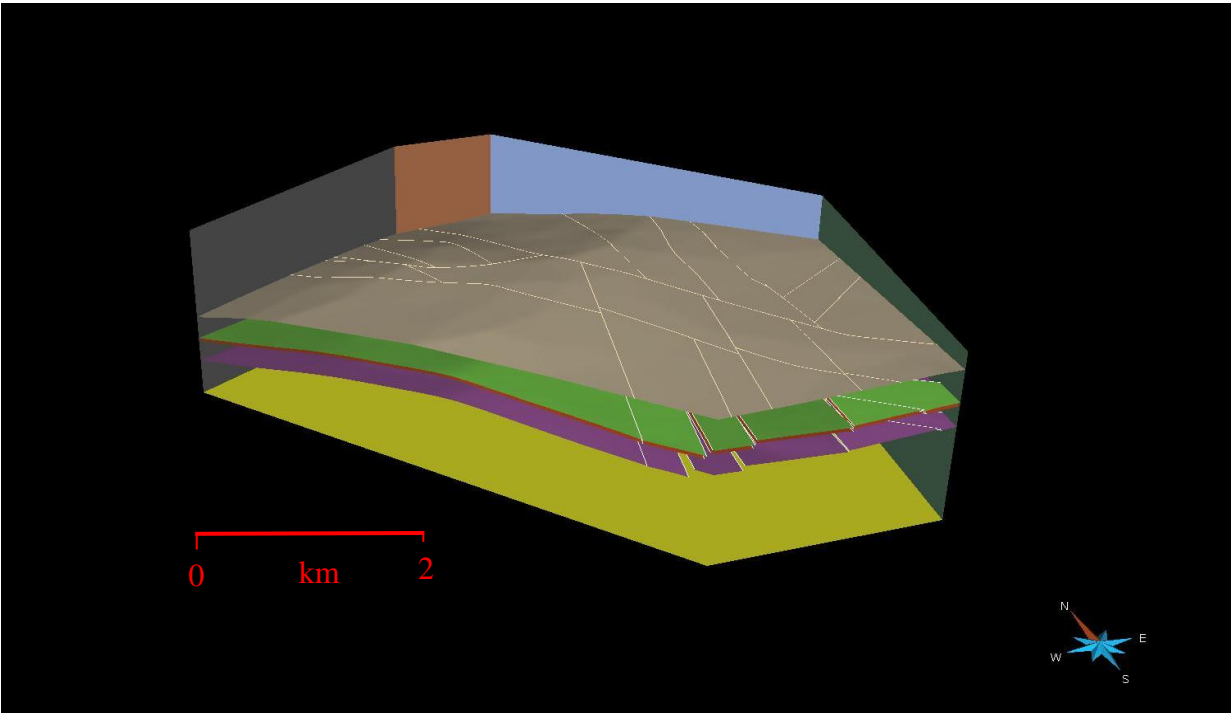
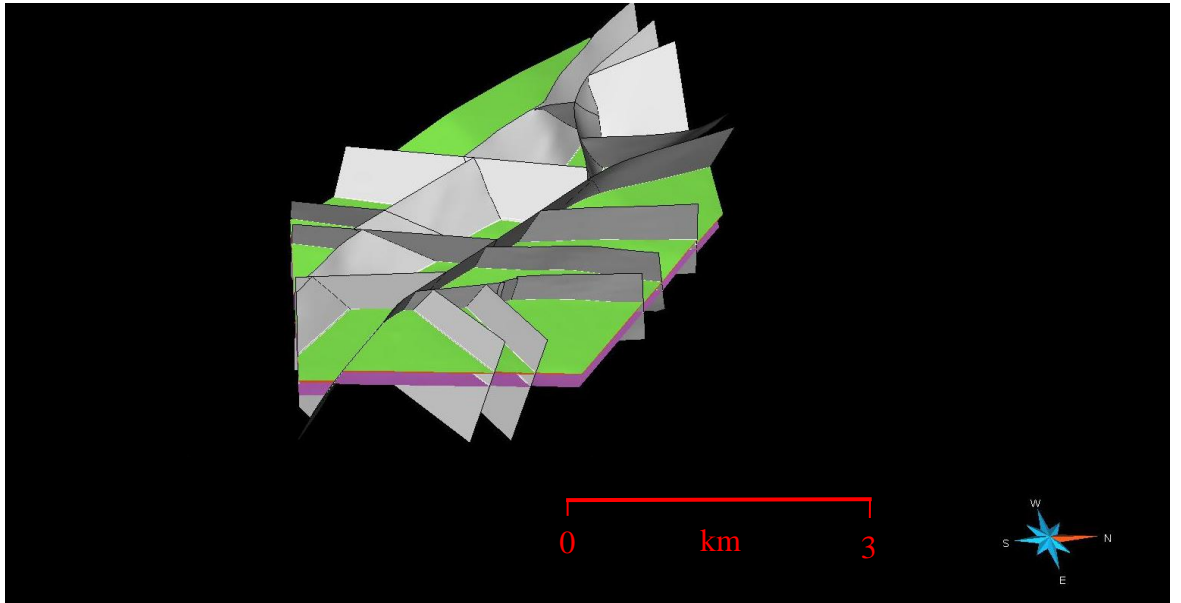
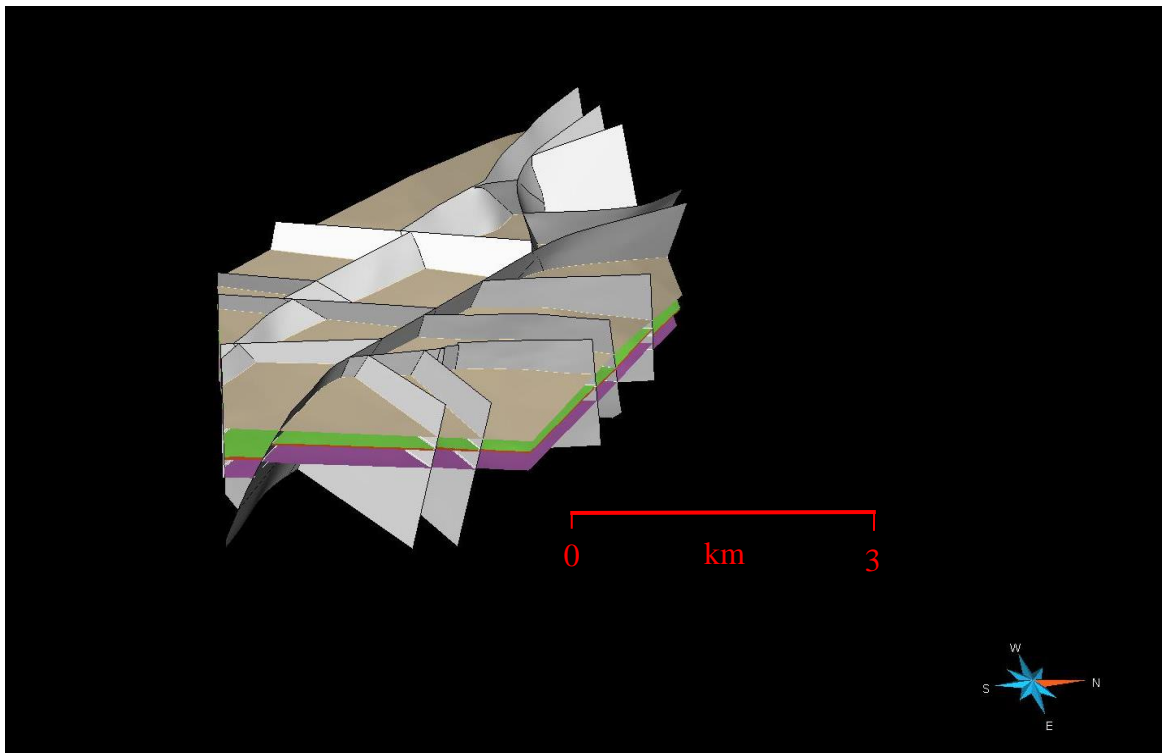


Fig. 122: The final horizons of the model



*Fig. 123: The horizons and the faults without the top of the Rotzo*



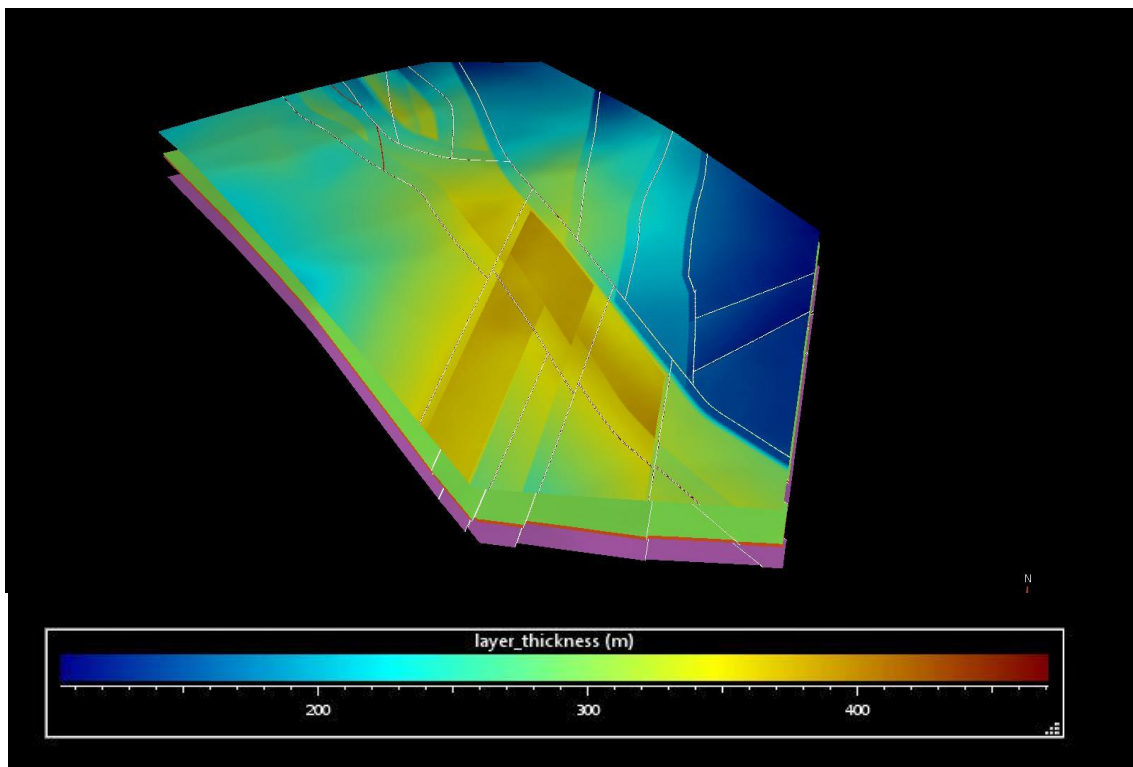
*Fig. 124: The model with the top of the Rotzo*



Once the horizons were built it was possible to compute volumes and thickness maps of the stratigraphic unit of the model. Volumes are reported in Table 5.

Table 5		
Formation	Thickness	Volume
Monte Zugna	200 m	$2.87355 \times 10^9 \text{ m}^3$
Loppio	30 m	$4.22666 \times 10^8 \text{ m}^3$
Rotzo	Variable	$3.88922 \times 10^9 \text{ m}^3$

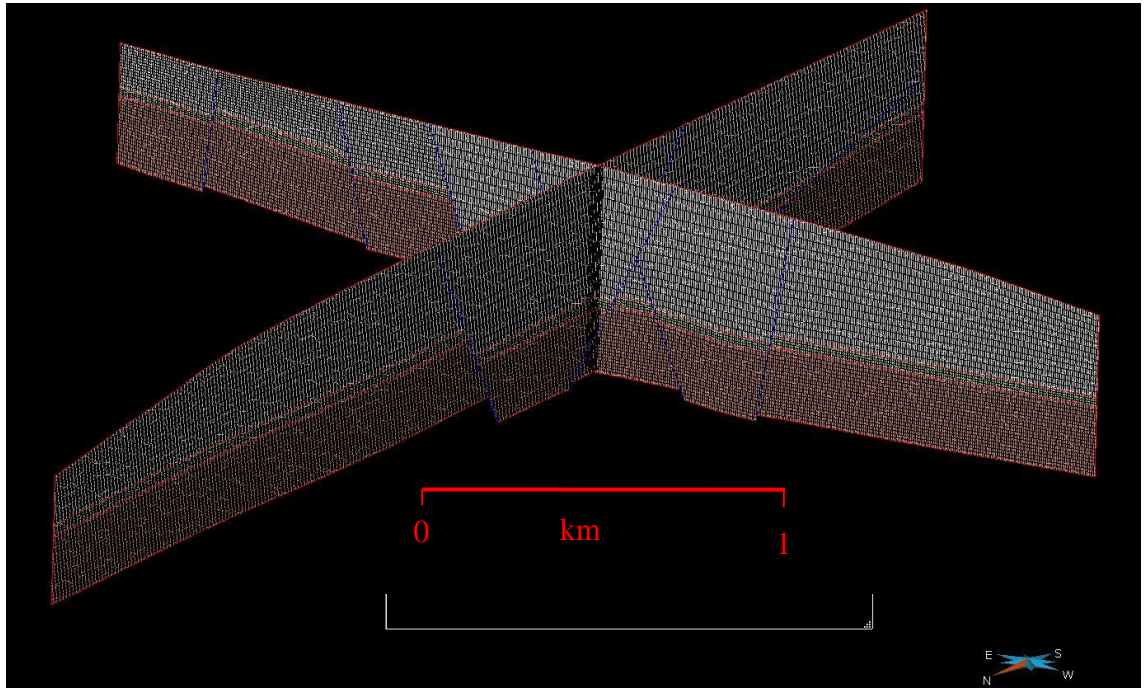
From the thickness map, it is possible to see clearly the thickness variations of the Rotzo Formation caused by the Jurassic syndimentary tectonic (fig.125).



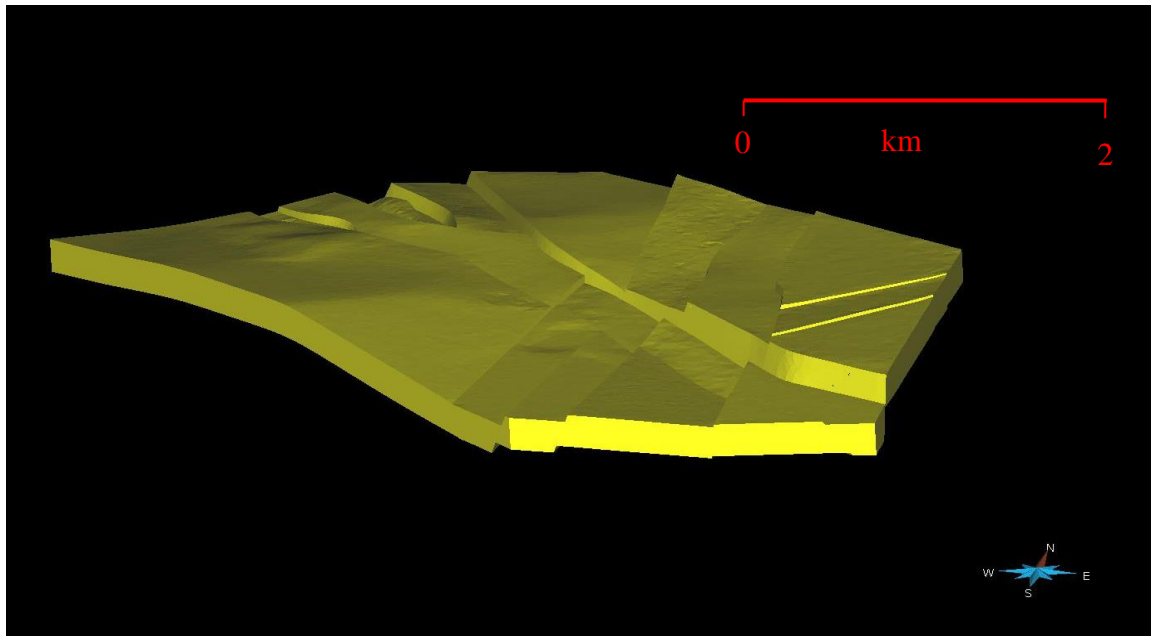
*Fig. 125: The thickness map of the Rotzo Formation*

The geological grid was finally generated by selecting the size of the cell and the vertical number of cells for each formation. A cell areal size of 5x5 meters was chosen. A different vertical cell resolution was selected for each unit. Monte

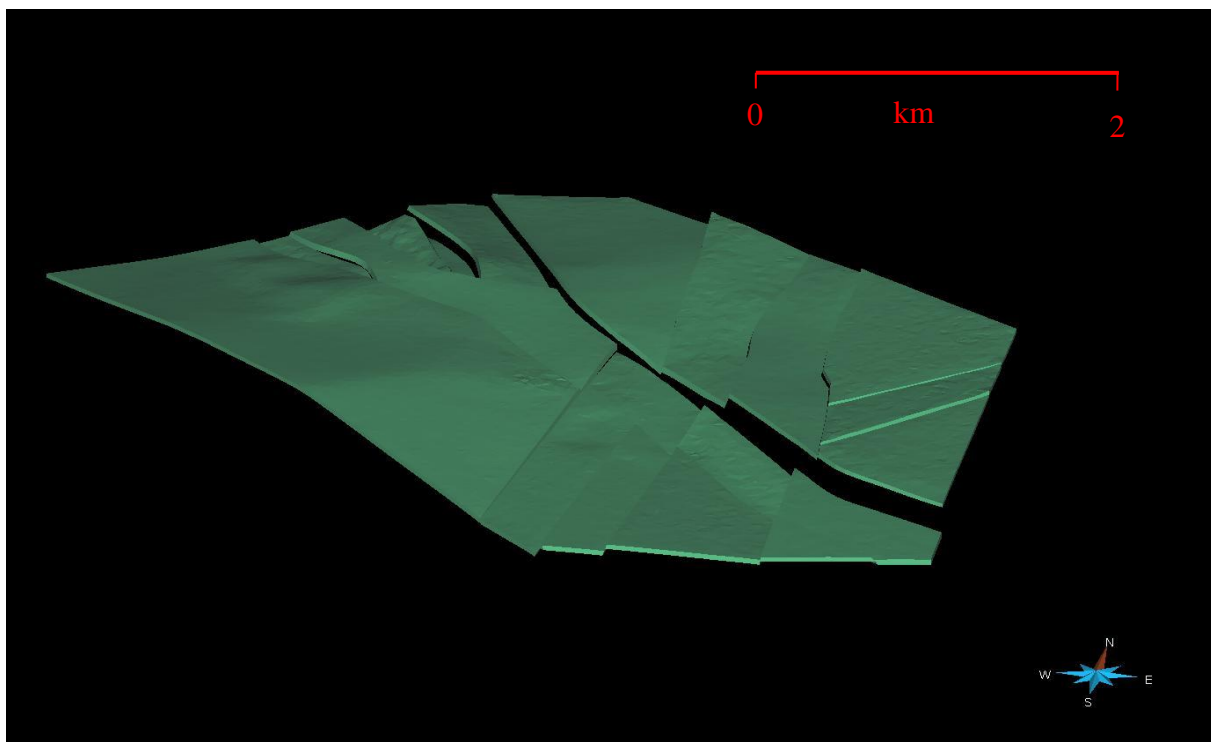
Zugna Formation was divided vertically in 20 cells, the Loppio Formation in 4 and the Rotzo Formation in 15. The cell size was chosen in order to have the possibility of modelling the fault related dolomitized bodies (width ranging from 10 to 30-40 m) that cut through the Monte Zugna and Loppio formations (see Chapter 2.1) without incurring in potential computational issues.



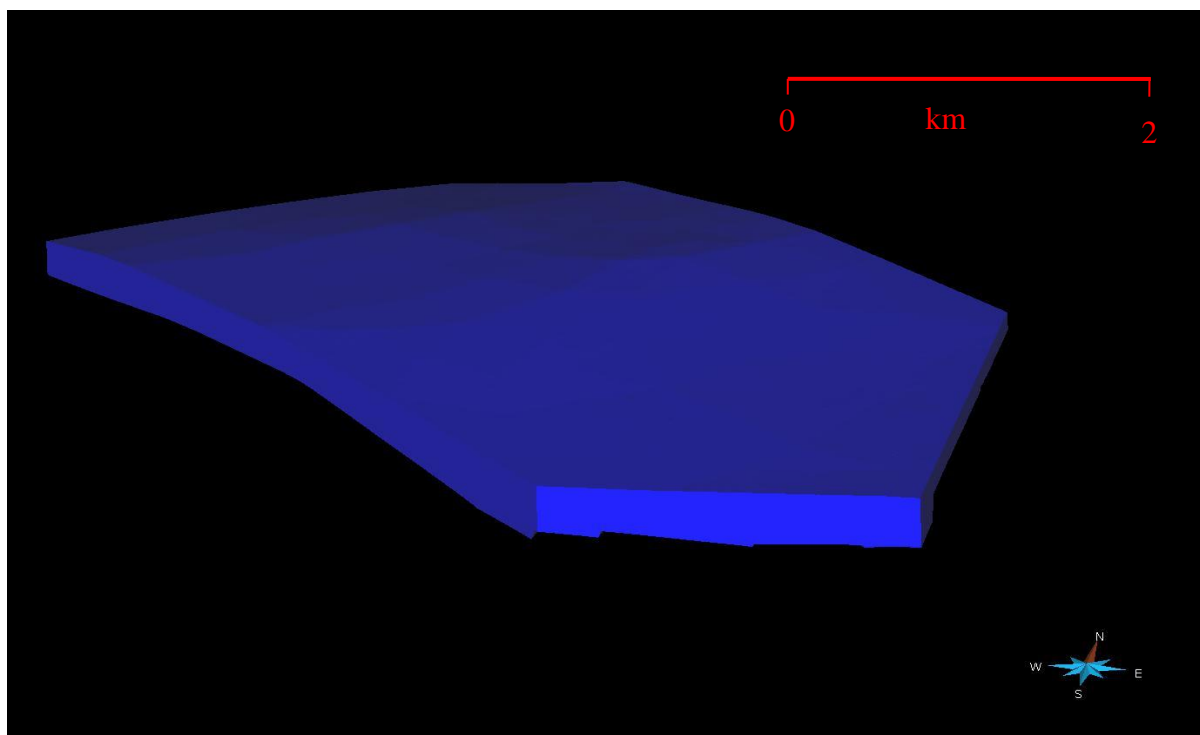
*Fig. 126: Two cross sections of the geological grid*



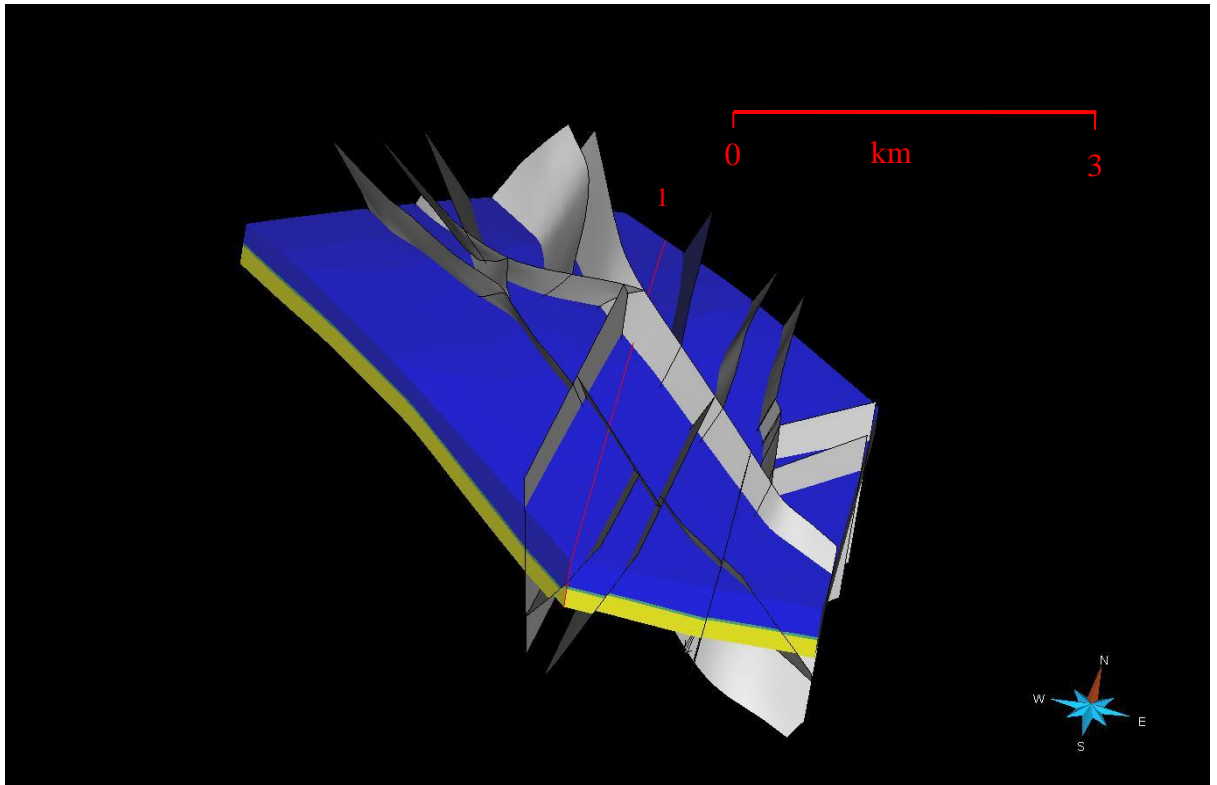
*Fig. 127: The region representing the Monte Zugna Formation*



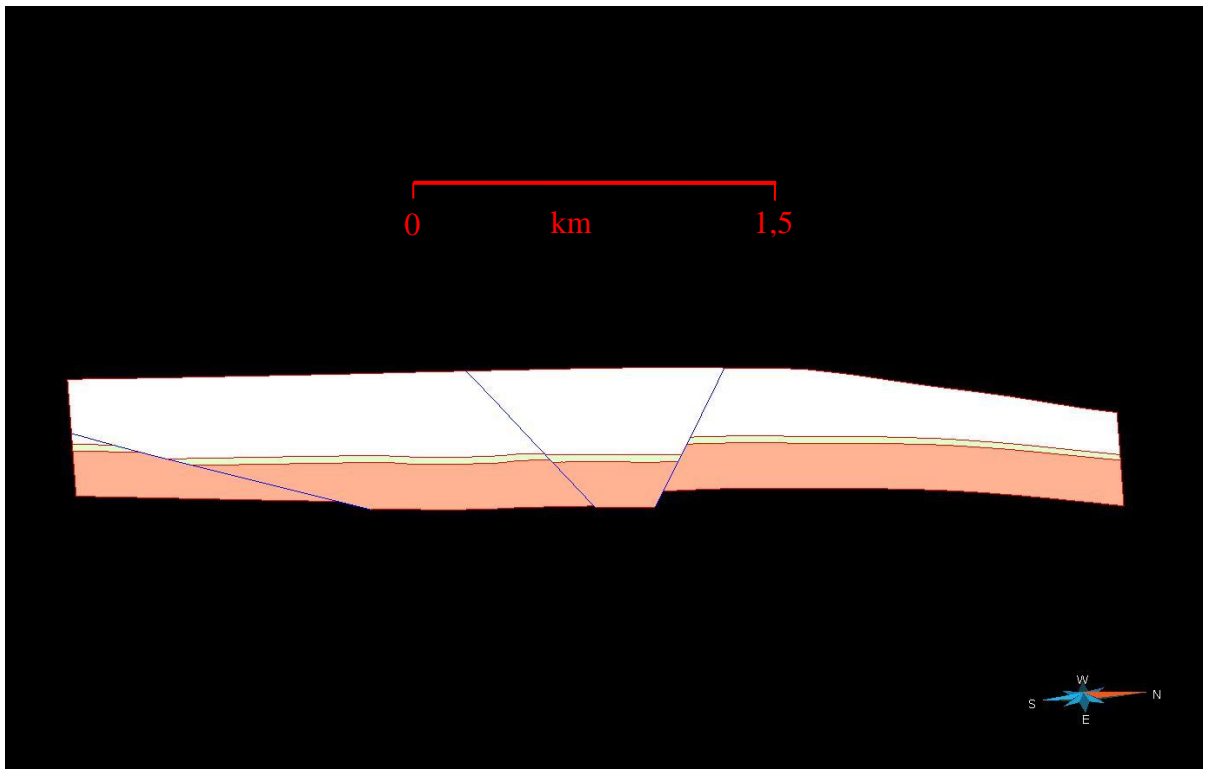
*Fig. 128: The Loppio Formation*



*Fig. 129: The Rotzo Formation*



*Fig. 130: The finale geological grid. The red line (1) represents the cross section of fig. 131.*



*Fig. 131: A cross section of the model*

#### 4.3.2.9 Modelling of dolomitized bodies.

The last feature to be modelled were the fault related dolomitized bodies described in Chapter 2.

These were modelled as region of the geologic grid. Since the dolomitized bodies run along faults and have average width of 30-40 meters in the Monte Zugna Formation and approximately 10 m in the Loppio formation, grid regions were created by applying a distance-from-fault constraints in the Monte Zugna and Loppio grid regions (fig 132). In this way, the width reduction of the dolomitized bodies from the Monte Zugna Formation to the Loppio Formation was preserved in the model.

The fault where samples for porosity analysis were collected were not in the model given their small throw, hence two small surface (faults) were added to permit the editing of the two bodies (fig.132).

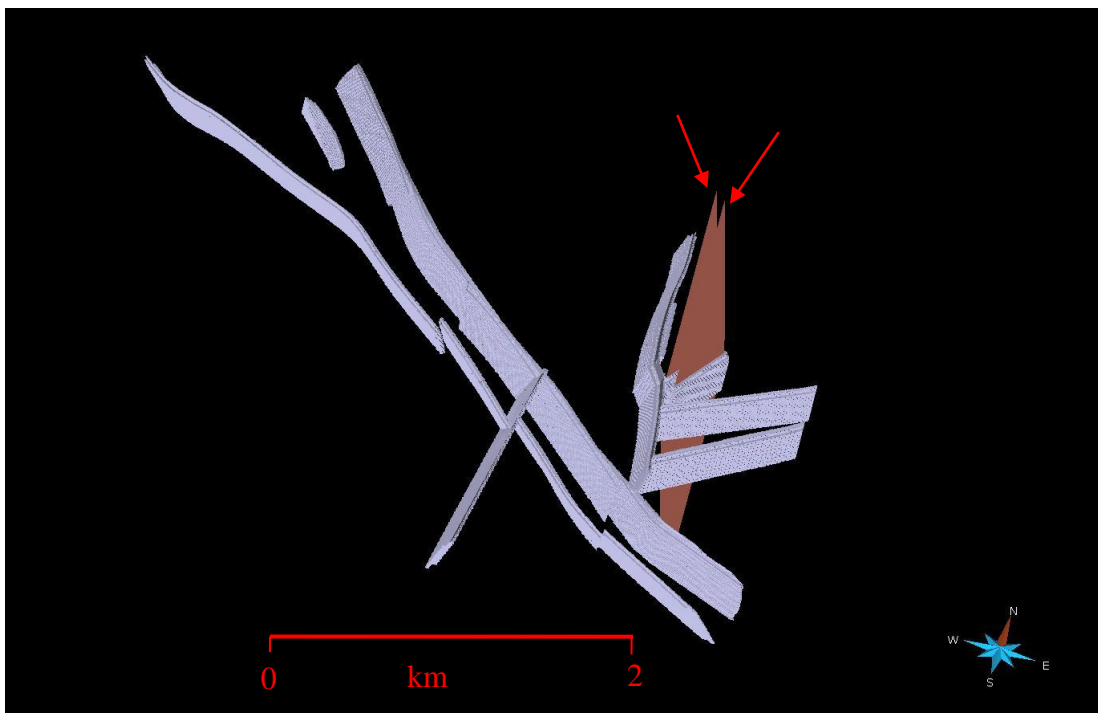


Fig.132: The dolomitized bodies and the two added surfaces (red arrows)



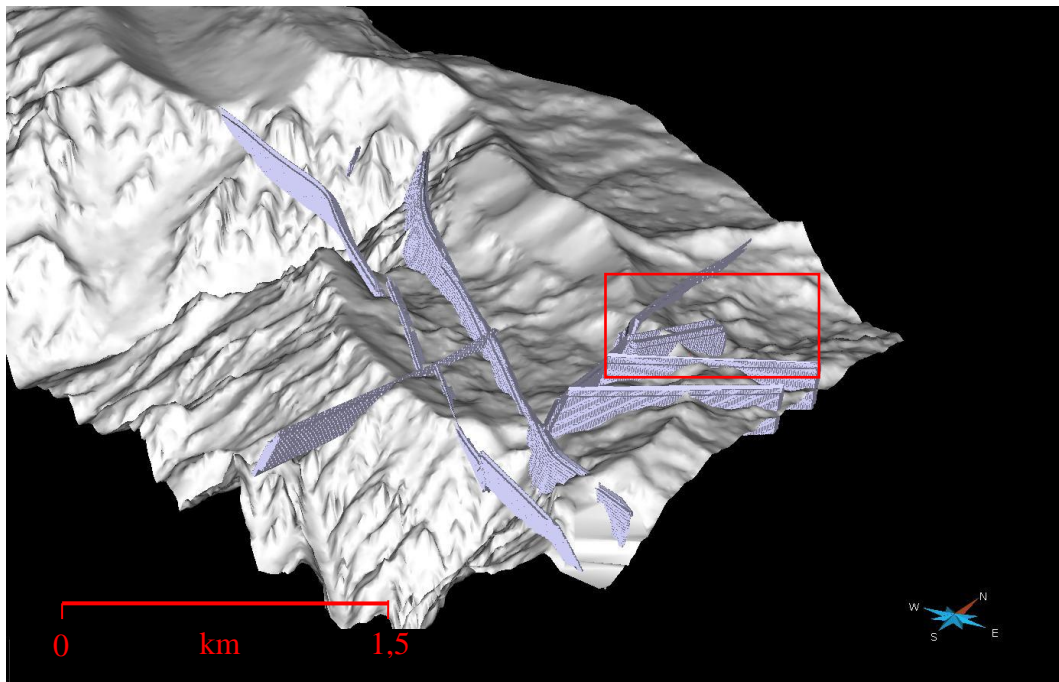


Fig. 133: The dolomitized bodies and the DTM. In the red rectangle the particular of fig. 134 and 135.

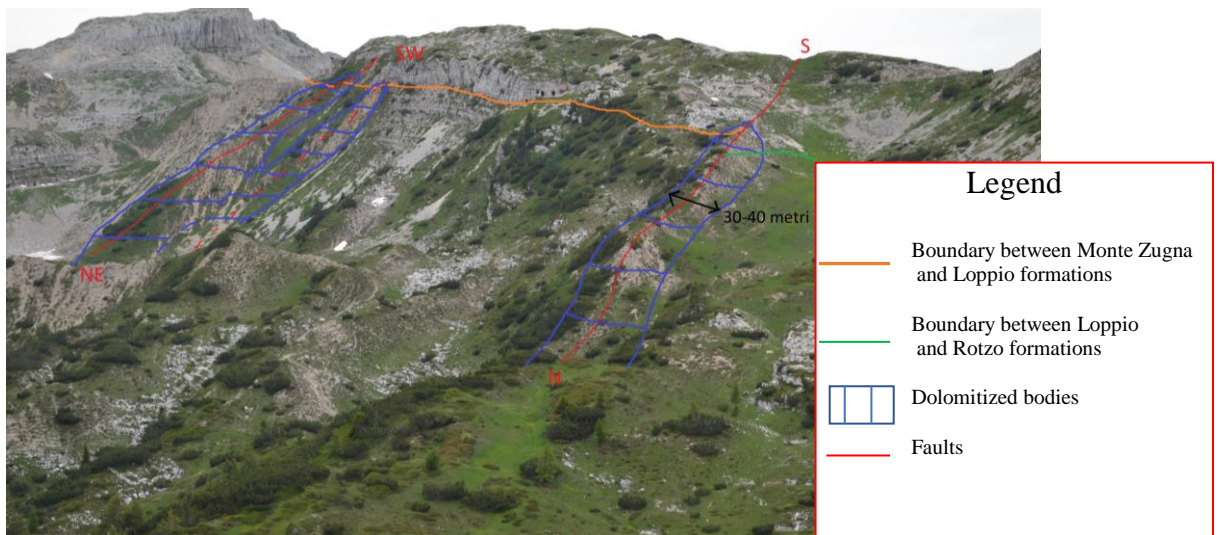


Fig. 134: The geological interpretation of the zone in the rectangle of fig.66

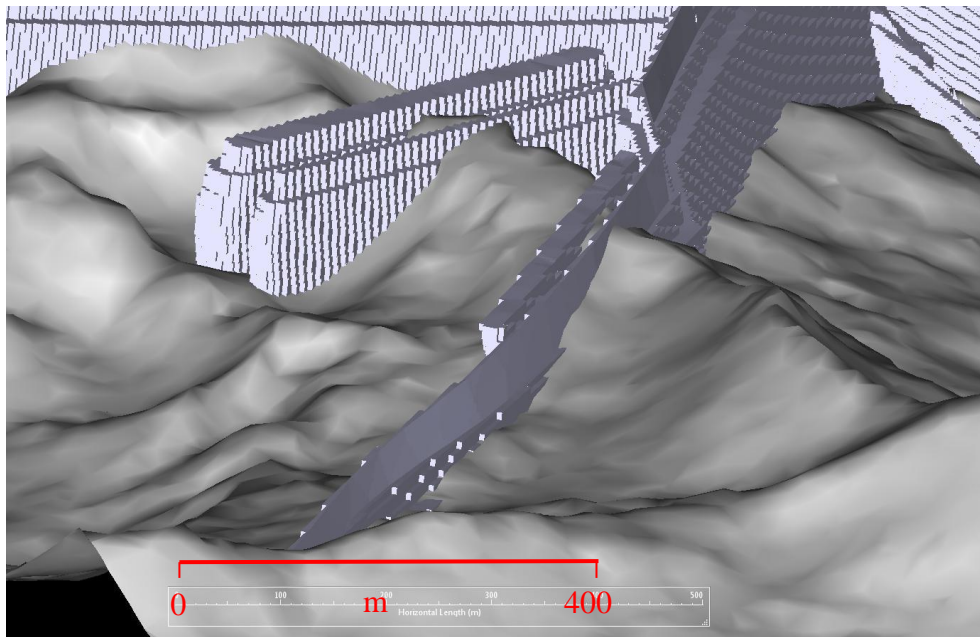


Fig. 135: The same zone of fig.134 representing into the model



#### 4.3.2.10 Features of the Monte Testa structure 3D geologic model

The 3D model gives some interesting information about the structural characteristics of the Monte Testa structure.

The shape of the horizons confirms that all the structure is gently folded (fig.136) along a NE-SW axis consistent with the Alpine compressive tectonic. Indeed the general dip of the strata increase going from SE to NW as testified by the dip map of the top of the Rotzo Formation (fig.137).

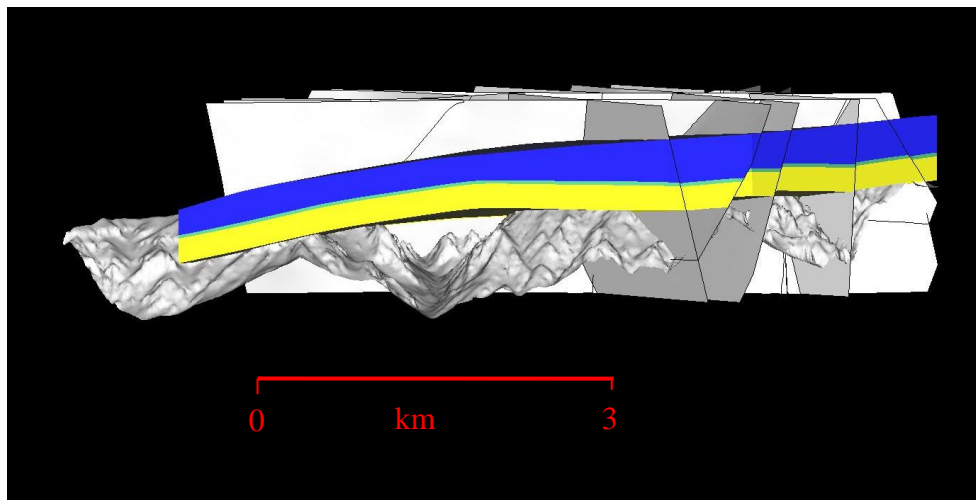


Fig. 136: The 3D model clearly shows the flexure that affected the whole area of the study

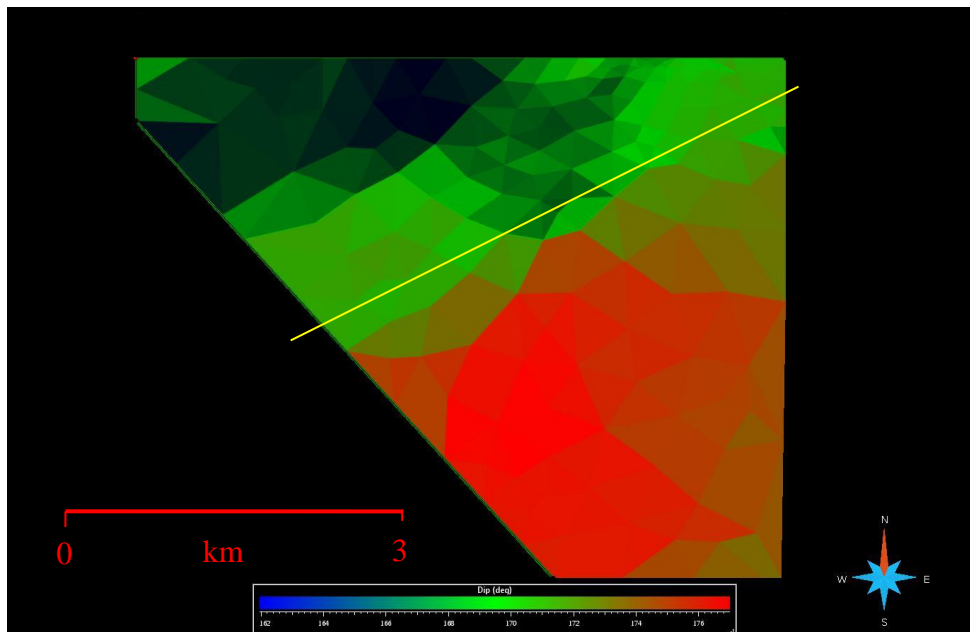


Fig. 137: The dip map of the top of Rotzo, view from top. It is possible to see that the dip of the strata increase going to NW (green colours). In yellow the fold axes.

The thickness map of the Rotzo Formation shows that this formation increases its thickness between fault 1 and 6, with a particularly sharp increase within the structure formed by fault 1 and 4. There the Rotzo Formation reaches a thickness of 400 m. Instead, the thickness decreases to 200 meters or less to the east of fault 1. This is a clear evidence of the synsedimentary character of the faults with fault 1 being the major boundary fault since the thickness of the Rotzo Formation increase on the west side of the fault.

It is noteworthy that the thickness of Rotzo increases also between the N-S trending faults 17 and 18, in agreement with the interpretation that both fault systems NW-SE and N-S were active during the Early Jurassic and the deposition of the Rotzo Formation (fig.71).

It is fair to say that this are not the total thicknesses of the Rotzo Formation because in the study area the real top of the formation is lacking. These thicknesses are referred to the top horizon chosen for the modelling. Nevertheless, even if partial, these values give interesting insights on the local differential subsidence induced by the Early Jurassic rifting.

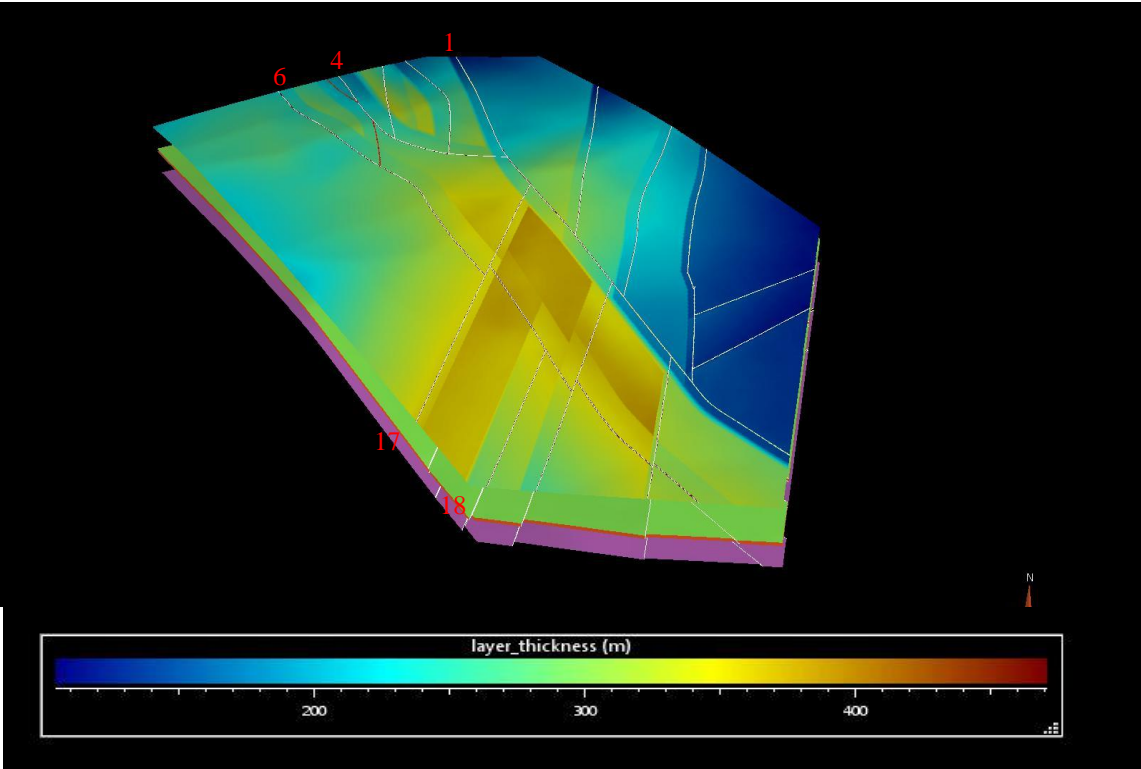
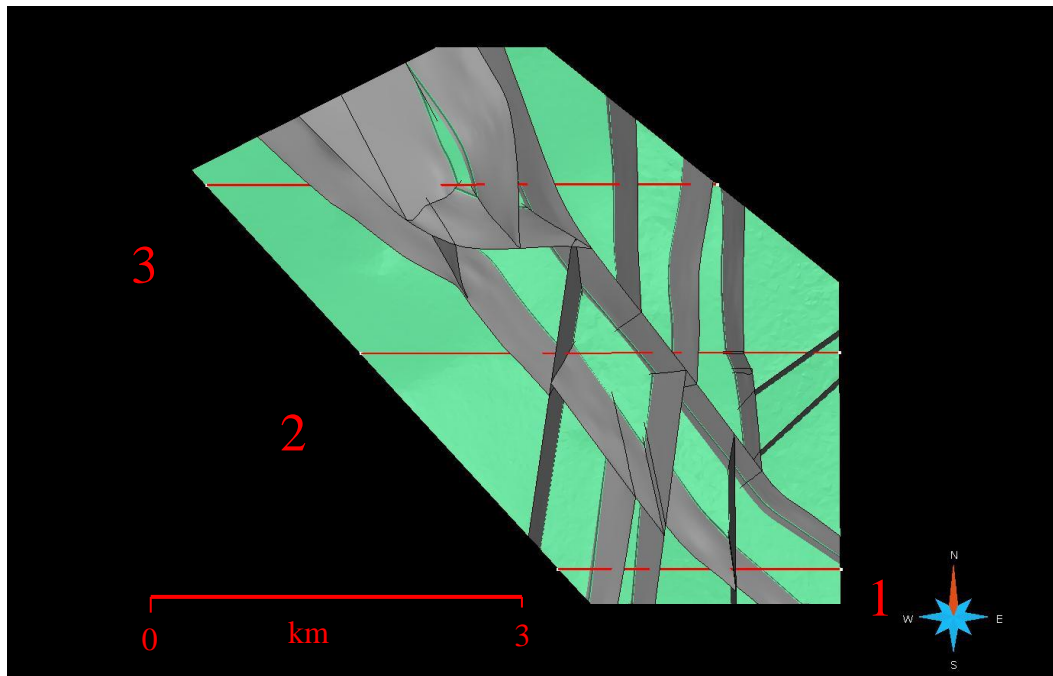


Fig. 138: The thickness map of the Rotzo Formation and the number of the faults

The 3D geo-model allows us to verify if the structure created by the tilting of the Loppio Formation can create favourable conditions for hydrocarbon accumulation. Cross sections (1, 2 and 3) of fig.140, 142, 144, show that the Early Jurassic extensional tectonic put in contact the high porous Loppio Formation with the low permeable Rotzo Formation, creating potential traps for hydrocarbon accumulation. Moreover, the hydrocarbon accumulation would be more probable within the syn-sedimentary structure because the large thickness of the Rotzo Formation (seal) as a thick seal prevents hydrocarbon escape.

A more complex situation can be described by considering the dolomitized bodies. Fig. 141, 143, 145 displays the same three cross sections of fig. with the dolomitized bodies highlighted. It is evident that the porous bodies are surrounded by two low-porosity and permeable formations (Zugna and Loppio) and sealed by the potential seal of the Rotzo. Again, this can lead to interesting hydrocarbon accumulation that would be favored by the persistency of the dolomitization along the faults as it has been revealed by the field mapping.



*Fig.139: The model view from top. In red the line of the three cross sections of fig.*

Cross section 1

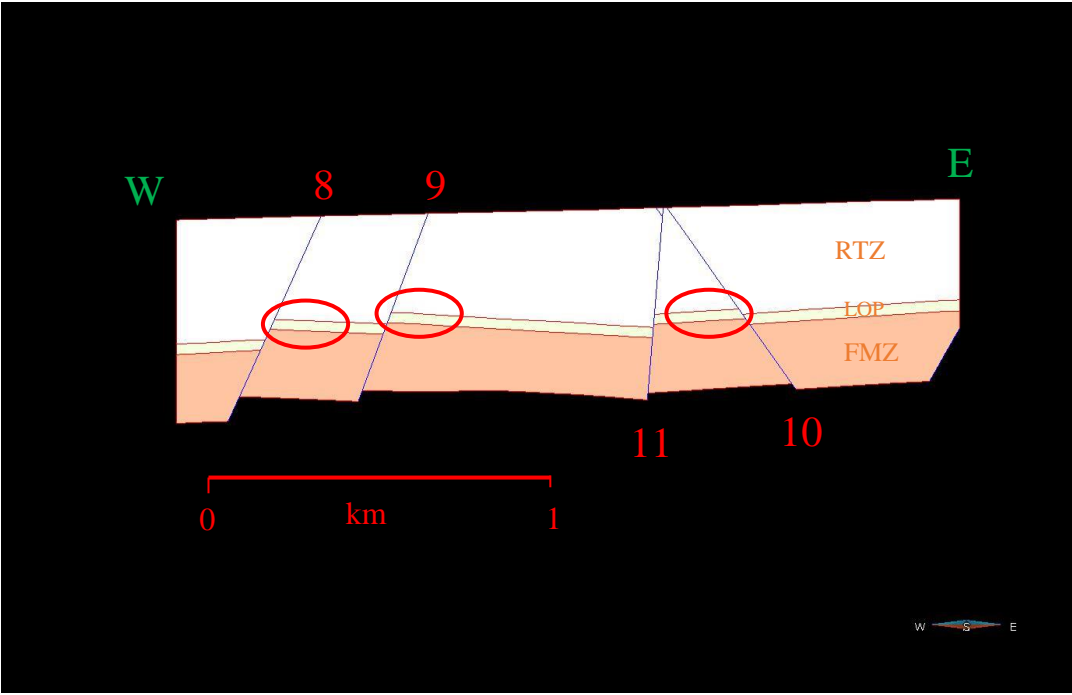


Fig. 140: From this cross section, it is possible to see that the Jurassic tectonic created favourable structure for hydrocarbon accumulation (red circle). The number is referred to the fault number.

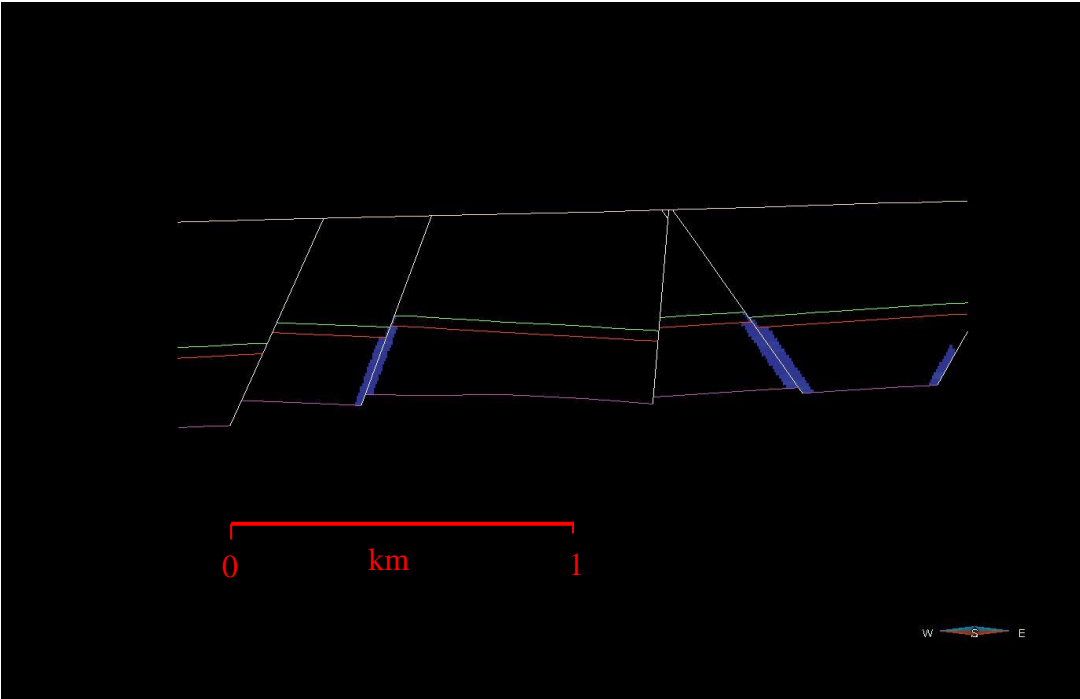
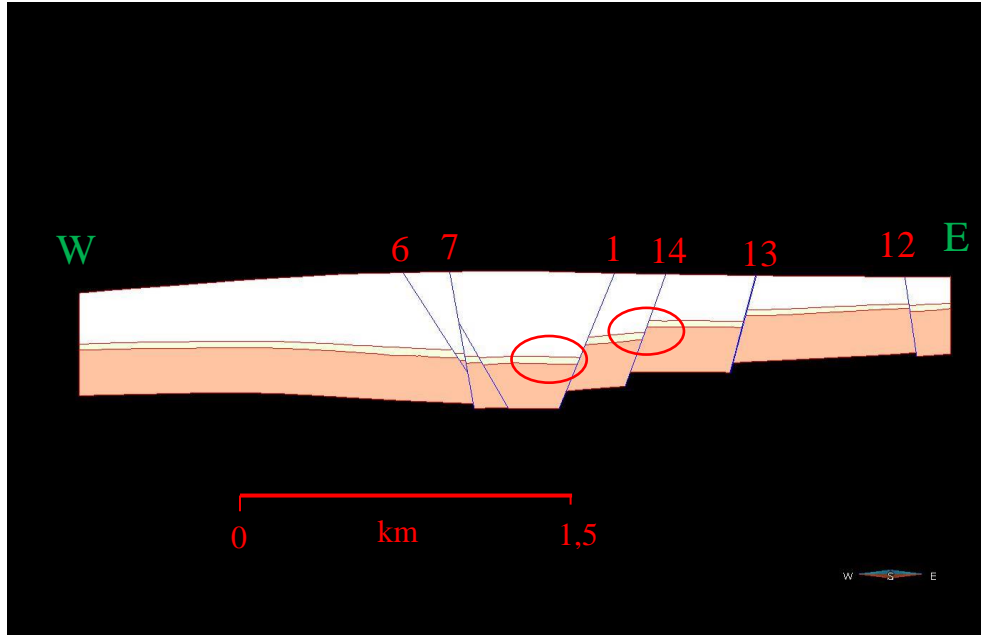
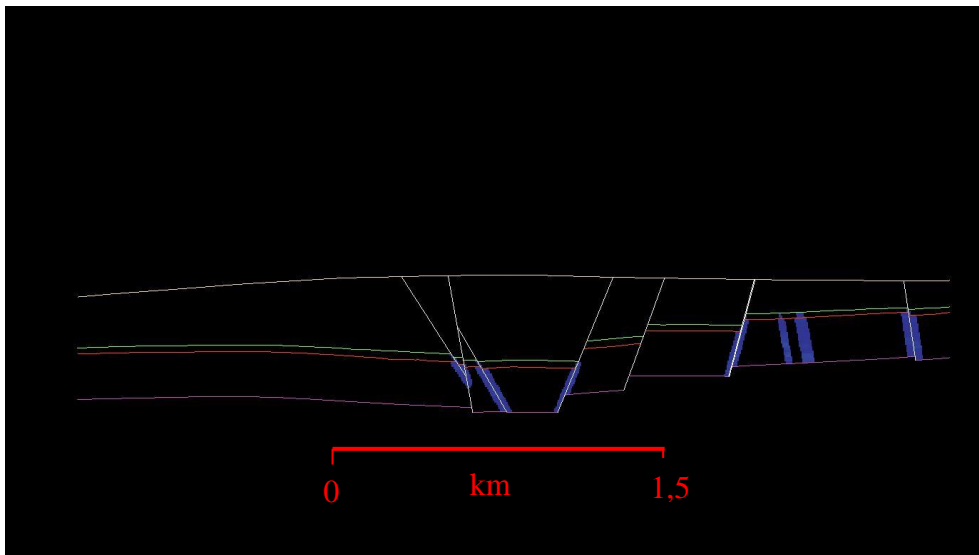


Fig. 141: The cross section with the dolomitized fault related bodies

Cross section 2



*Fig. 142: The traps created by the Jurassic tectonic. Here is evident the increase in thickness of Rotzo Formation within faults number 1 and 6*



*Fig. 143: The fault related dolomitized bodies*

Cross Section 3

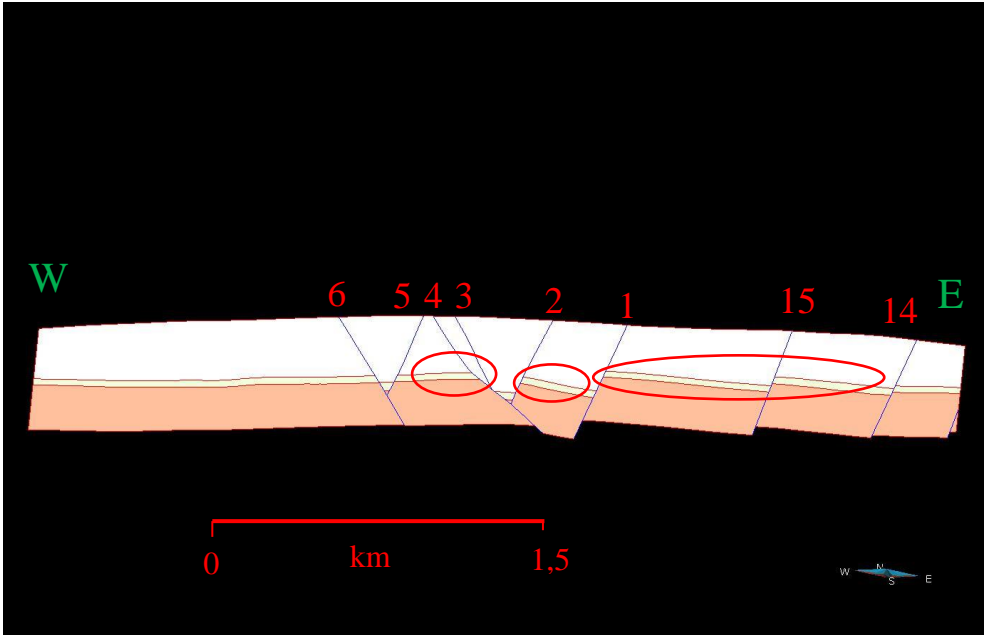


Fig. 144: The Cross section number 3

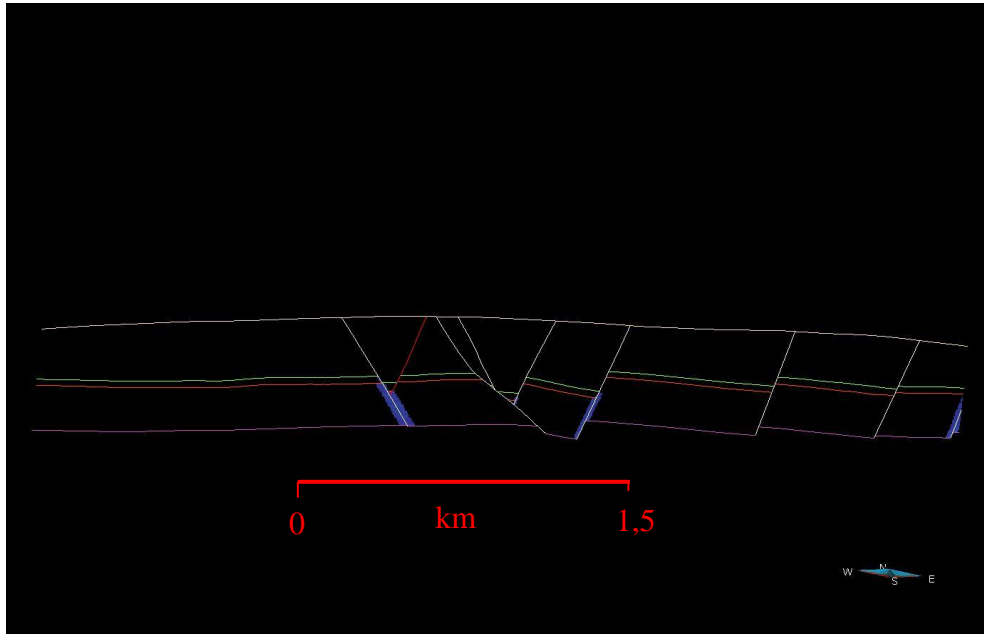


Fig. 145: Cross section number 3 with the fault related dolomitized bodies

## 5. Porosity distribution

### 5.1 The geostatistic

In Skua Gocad the geological grid can be populated with physical properties through several ways.

The simplest situation is when within a geological feature (rock formations, fault planes, etc.) a property is constant- i.e. the same in the whole unit. However usually, properties in geologic unit have a spatial variability, which can be predicted using geo-statistical methods.

Geostatistic takes in account that geological structures usually have a preferred orientation depending for example from channel orientation, fault planes attitudes, strata dip and azimuth ecc. . For this reason trends has a fundamental role in probability of finding a particular value of a physic parameter and the evaluation correlation between data point (Skua\_User-Manual).

The prediction of physical parameters in space depends on the statistical distribution of a give data set, which can be evaluated with histograms where data bins (range of value) are plotted against their frequency.

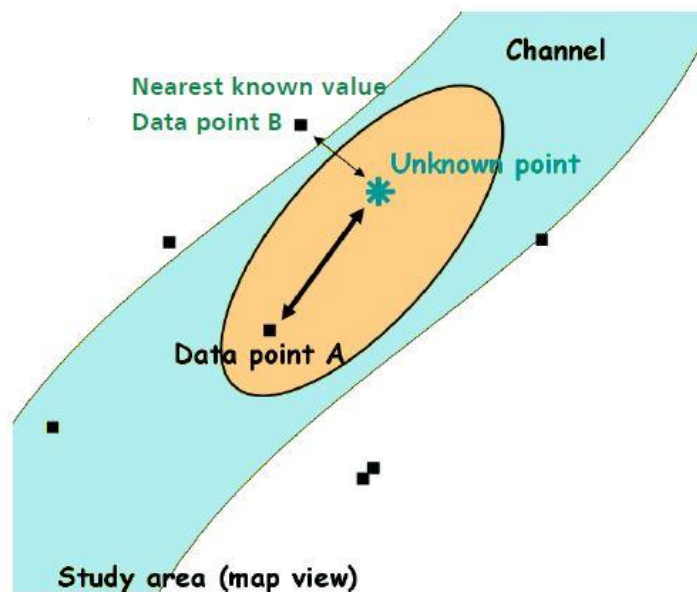
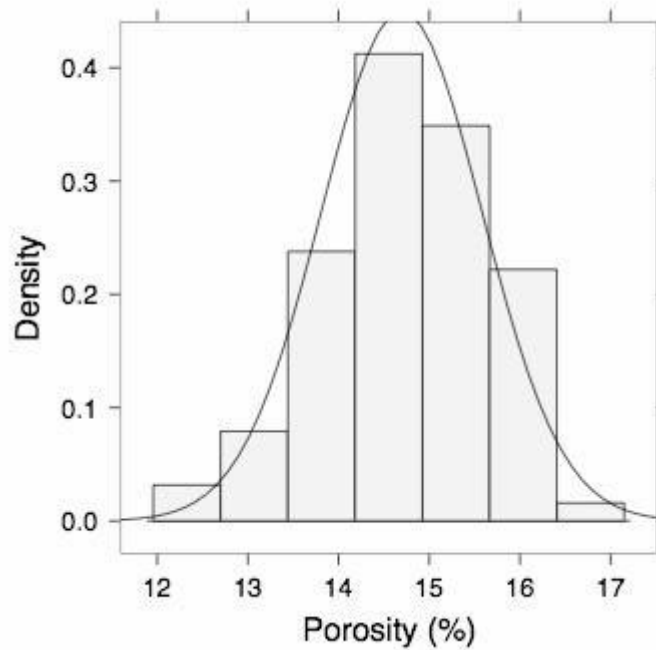


Fig. 146: A data unknown point related with a know data point (Skua-User-Manual).





*Fig. 147: An example of histogram (G. Bohling, 2005).*

From the histogram are then derived mean, variance and standard deviation of the available data.

These statistical values allow SKUA to perform geostatistical analysis of non constant values using interpolation or simulation algorithms.

The interpolation derive an estimate of the distribution of physical parameter in space on the base of nearby data. (Skua-User Manual). In this case, the user has to decide the data points and the weighting functions to be used during the interpolation. One of the most used weighting functions is the variogram, which describes the correlation of the data with their distance.

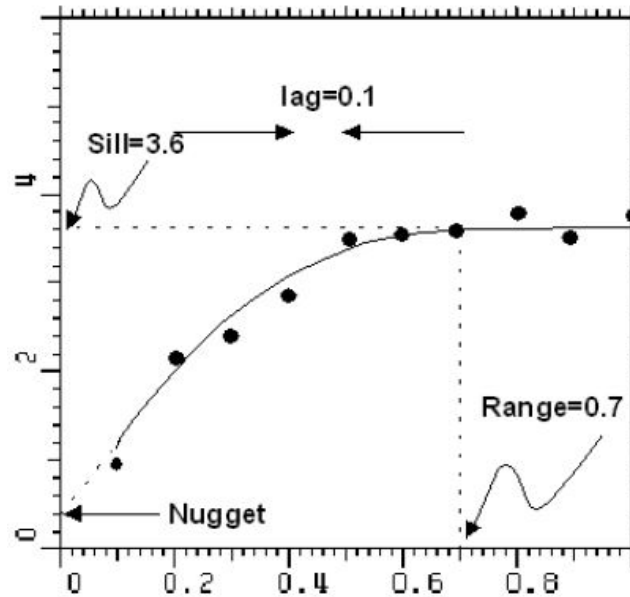


Fig. 148: A variogram with the three main parameters

In fig. 148 we can see a typical variogram where on the y axes is the variance and on the x axes the distance from the data points (lag). A variogram is characterized by three main parameters: the value of distance at which the data are not any more correlated called “range”, the variance value at the range point called sill” and the “nugget, which takes into account the data variance at small scale (G. Bohling, 2005; P. A. Burrough et al. 1998).

From the available dataset is possible to extract an experimental variogram using the method of moments (Matheorn, 1965).of fig. 149

$$\gamma(h) = \frac{1}{2m(h)} \sum_{i=1}^{m(h)} [z(x_i) - z(x_i + h)]^2$$

Fig.149: The method of moments of Matheron.  $z(x_i)$  is the available data,  $m(h)$  is the number of paired comparison at lag ( $h$ ).

In Skua Gocad is possible to obtain 1D (only the distance between points is taken into account), 2D (azimuth and distances), and 3D (distance, azimuth and dip angles) variograms. In the 2D and 3D cases, other parameters are needed: the lag distance (distance at which the variogram is computed), number of lags, bandwidth and lag tolerance (How much the distance between pairs can differ from the exact lag distance (<http://vsp.pnnl.gov/>) (fig.150)

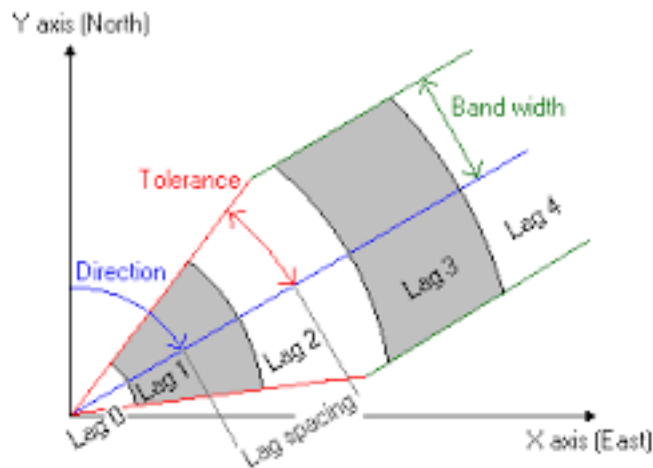


Fig. 150: The other variogram parameters (spatial analyst.net)

The experimental variogram cannot be used directly for the interpolation, because it can have some errors such as negative variance and the interpolation algorithms need positive values of variance (M.A. Oliver et al. 2013; Arcgis Help). For this reason it is necessary to create a model variogram fitting a mathematical curve to the points of the experimental variogram; the most used ones are Spherical, Gaussian and exponential curves (fig.151) (G. Bohling, 2005).

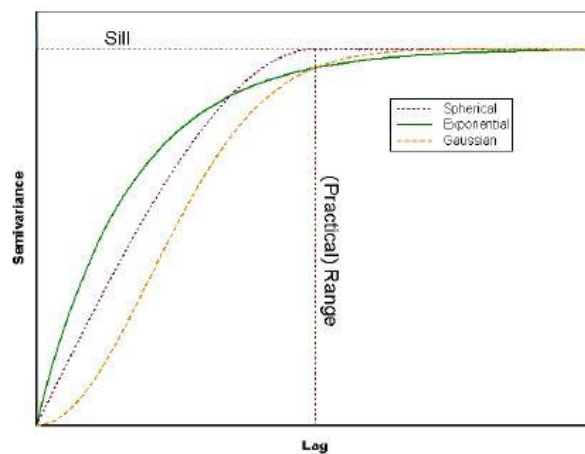


Fig. 151: The three main mathematical curves used for the realization of model variogram (G. Bohling, 2005).

Using the model variogram derived from the experimental data range, sill and nugget are automatically extracted by the software and can be used for the interpolation. However, it is also possible to eventually insert these values manually on the basis of field observation.

The main interpolation methods available Skua-Gocad are: Nearest Neighbour, Arithmetic mean, Linear Interpolation, Inverse Distance and Kriging. The most used is Kriging. Kriging technique uses variogram information in order to assign value to the unknown data.

The main types of kriging are simple kriging and ordinary kriging.

The simple kriging is used generally with data that have not any evident spatial trend and the mean of data is constant and known. When a point is out of the range of correlation of variogram, the kriging assigns to it the global mean value.

On the other hand, ordinary kriging is used when the data is characterized by an evident spatial trend, the mean of the value is not constant and it is calculated for each point. If a data is out of the range of correlation of the variogram, its value cannot be found and not be assigned (Skua User Manual).

#### Simulation algorithms

The geostatistical simulation uses data points (hard data), variogram and eventually soft data in order to produce equally probable numerical models (Skua User Manual).

The most important simulation methods is the SGS (Sequential Gaussian Simulation). Using this method the input data is converted into a Gaussian distribution and after that the following steps are performed (Geoff Bohling, 2007):

1. Generate a random path through the grid nodes
2. Visit the first node along the path and use kriging to estimate a mean and standard deviation for the variable at that node based on surrounding data values
3. Select a value at random from the corresponding normal distribution and set the variable value at that node to that number
4. Visit each successive node in the random path and repeat the process, including previously simulated nodes as data values in the kriging process

## **5.2 Distribution of porosity in the Monte Testa 3D model**

The area of the study from the Jurassic onward underwent a complex porosity evolution. For this reason, we decided to model two scenarios where a distinct and constant porosity value was assigned to each rock formations of the Calcari Grigi group.

The first scenario would represent the porosity of the area right after the deposition of the Rotzo Formation. As testified by the porosity analysis the Rotzo Formation has no macro-porosity and for this reason we decided to attribute a porosity value of 0% to this formation. The Loppio Formation had an initial porosity of 20% (as testified by the amount of cement between the grains), but when the Jurassic extensional tectonic started it had to be partially cemented allowing its documented syn-sedimentary brittle deformation. For this reason we adopted a sounding value of 8% for this formation.

The Zugna Formation such as the Rotzo Formation should had low porosity as testified by the thin section however the Jurassic tectonics surely caused fracturing. Typically, the porosity in fractured carbonates rocks can reach a value of 1% (Weber and Bakker, 1981) and for these reasons we decided to assign to the Monte Zugna Formation a porosity values of 1%.

The second scenario describe the porosity situation after the formation of the fault related dolomitized bodies. Also in this case a constant value of 0% has been assigned to the Rotzo Formation This estimate, supported by the porosity analysis, is also confirmed by field observation since the fault related dolomitized bodies cut-across the formation only in its lower part and only along the major faults. This confirms that Rotzo Formation porosity and permability had to be very low and did not allow the circulation of the dolomitizing fluids. Loppio and Zugna Formations are now completely cemented, but a porosity value of 0% is unrealistic since the two formations were likely affected by fracturing already in Jurassic times. For this reason, a porosity value of 1% was given to both the formations.

For the fault related dolomitized bodies two different approaches were chosen.

The collected porosity values were not enough to perform good interpolation or simulation in the whole volumes of the dolomitized bodies. This is due to the fact that the samples, where the porosity has been evaluated, were collected only from three dolomitized bodies and most of them in only one dolomitized body (fig.32). For this reason, it was decided to assign at the whole volume of the dolomitized bodies, the mean of the porosity values extracted from the histogram in fig, 152. The mean porosity value is 4,7%.

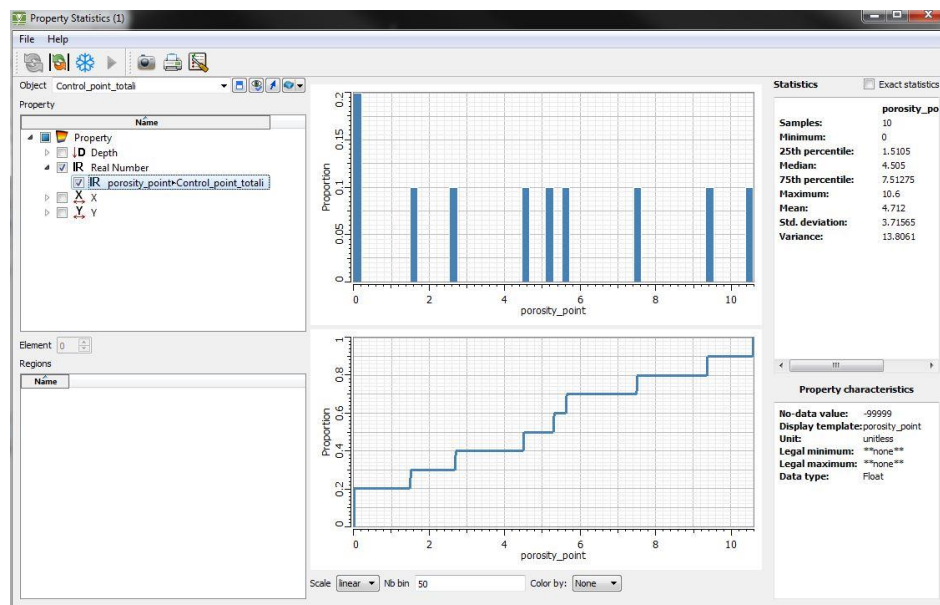


Fig.152: The histogram of the porosity values extracted from the samples collected for this work

On the contrary, an interpolation on the dolomitized body, where the higher number of sample were collected (5 samples), was perform using both Simple Kriging and SGS.

Five points is not enough to obtain a good experimental variogram. For this reason the model variogram was obtained giving manually the values of Azimuth, Dip (measured on the field) of the dolomitized body and the Range of the porosity. Because we are in a 3D model the values of Range are three, one for each direction.  $R_v$  is the vertical Range and in this case it follows the dip of the fault,  $R_1$  is the range along the azimuth and  $R_2$  is perpendicular to the fault plane. From field observation and porosity analysis we know that the higher porosity values are associated with breccia along faults. For this reason the values of  $R_v$

and R1 must be high and along dip and azimuth the faults porosity values should not have great variability. On the contrary, perpendicular to the fault plane the porosity values change abruptly and R2 value must be low. In particular, the values assigned were  $R_v = 600$  m;  $R_1 = 600$  m and  $R_2 = 20$  m

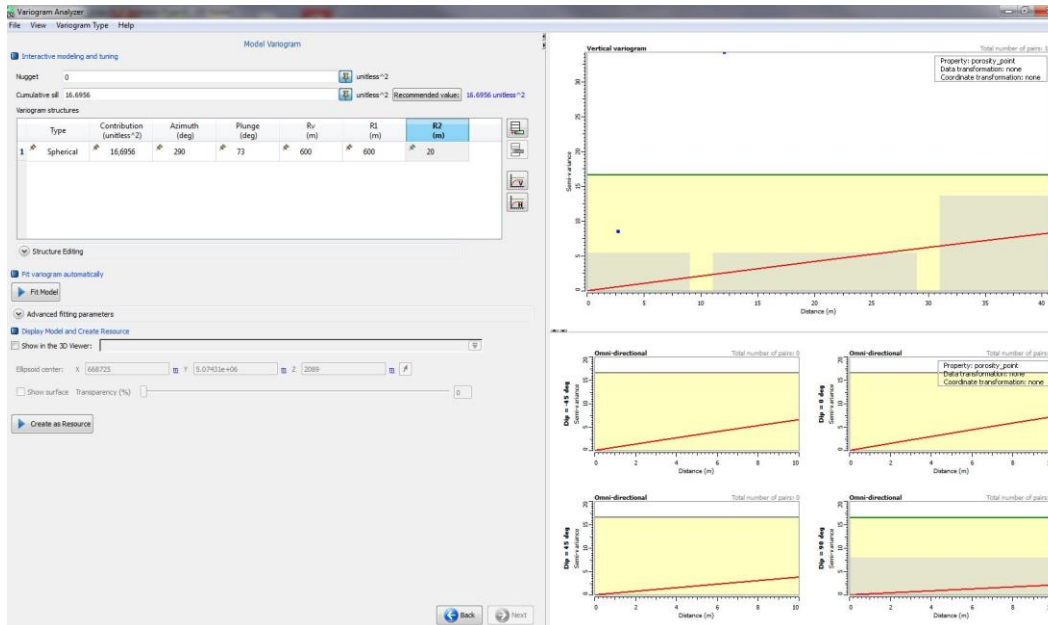


Fig. 153: The panel of the variogram analyzer in Skua where is possible to create the variogram

The model variogram was hence extracted using the values fixed above and used for both Simple Kriging interpolation and SGS.



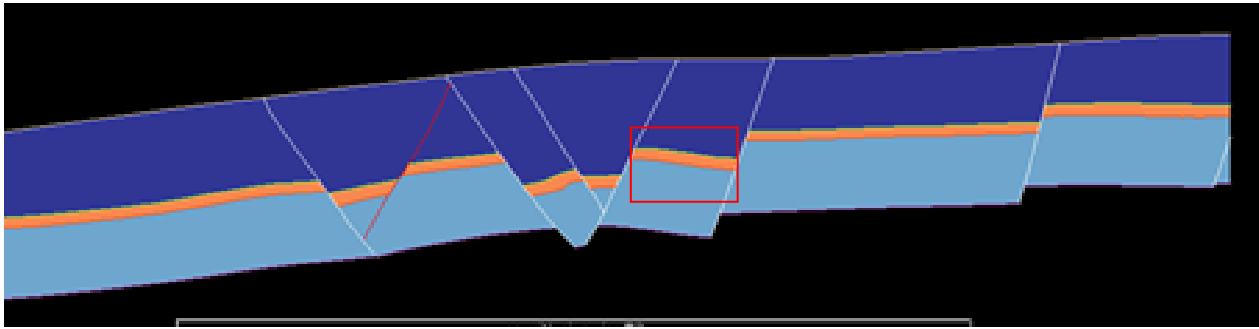
### 5.3 Results from the porosity distribution

The distribution of porosity in the 3D geomodel allows to reconstruct the porosity evolution of the area from the Jurassic (right after the deposition of the Rotzo Formation) up to today.

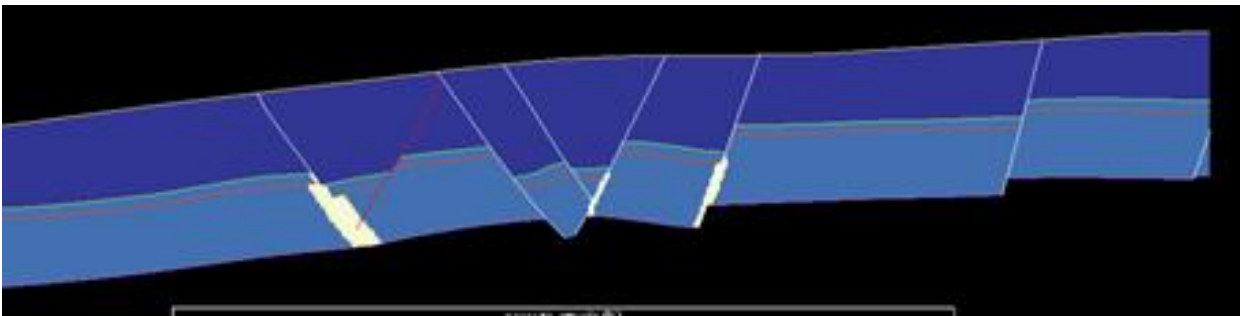
In fig. 154 we can see that the tilting of the Loppio Formation (8% of porosity) put in contact this high porous rock formation with a no porous and no permeable formation (Rotzo, 0% of porosity). This framework might have created good potential traps for the hydrocarbon, which could accumulate in the highest part of the tilted block where the Loppio Formation is laterally and above sealed by the Rotzo Formation. In addition the porosity of the Monte Zugna could likely have been very low (1%), and hydrocarbons could have not easily flowed through this formation, being confined within Loppio Formation. In such a kind of structural framework hydrocarbon might fill the porous formation (i.e.Loppio) laterally using fault zones as conduits. Similarly, if the porosity of the fault zone is high enough hydrocarbons could also escape whenever they reach the point of contact between the porous formation and the fault (fig.156). The permeability of the fault zones are hence of paramount important on such a kind of geological framework or potential hydrocarbon reservoir-sealing system (D.Wiprut and M.D.Zoback, 2002).

In fig. 155, we can see the porosity distribution after the formation of the fault related dolomitized bodies in the Late Paleocene-Early Oligocene (DiCuia et al., 2011). The porosity of the Loppio Formation was suppressed by cementation and likely was only formed by fracturing (1%) such as the Monte Zugna case.

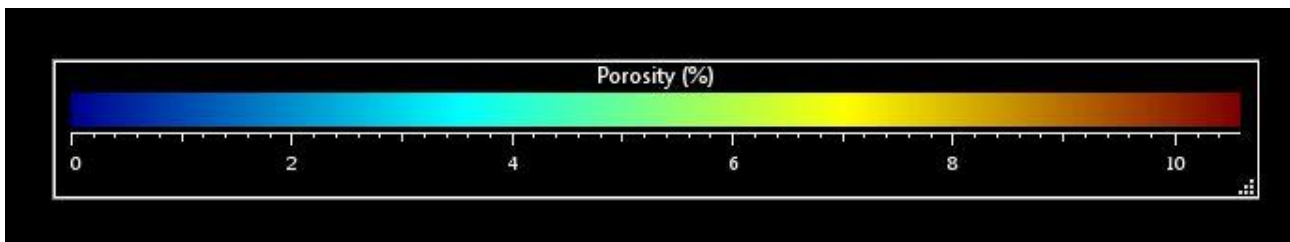
The Rotzo Formation has a porosity value of 0% like in the Jurassic. On the other hand, the fault related dolomitized bodies has porosity values ranging from 0% to 10,6% with a mean of 4,7%. This porous bodies enclosed by low porous and permeable formation might form very favourable hydrocarbon reservoirs.



*Fig. 154: The porosity distribution during the Jurassic, right after the deposition of the Rotzo Formation. It is clear that the Rotzo Formation is the seal and the tilted Loppio Formation forms a very good reservoir, (In the red rectangle, the particular of fig.5).*



*Fig. 155: Fig. 7: Right after the Formation of the fault related dolomitized bodies the situation is very different with respect to the Jurassic one. Here the Rotzo Formation forms always a seal but the reservoir is dominated by the dolomitized bodies.*



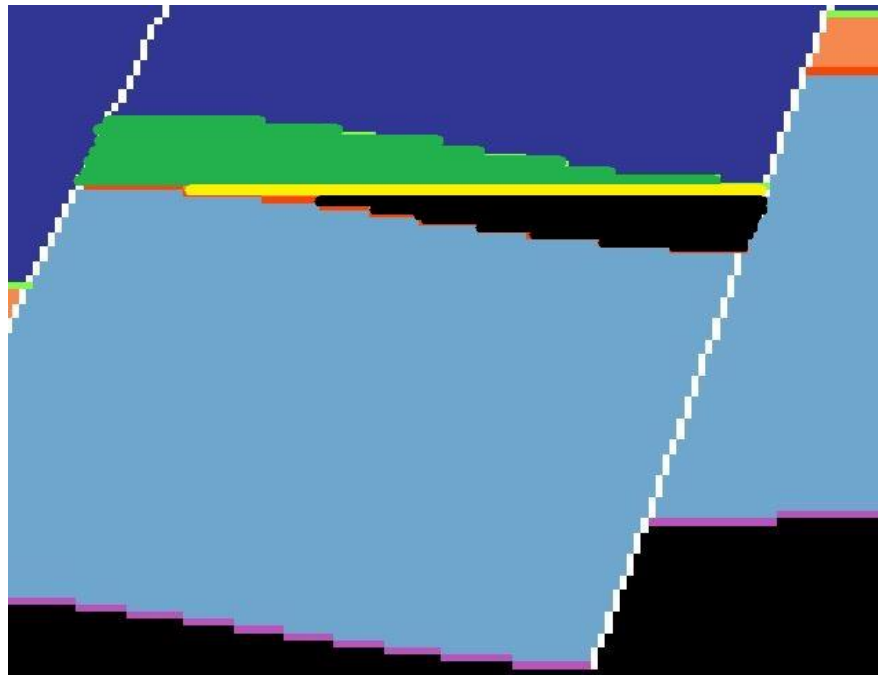
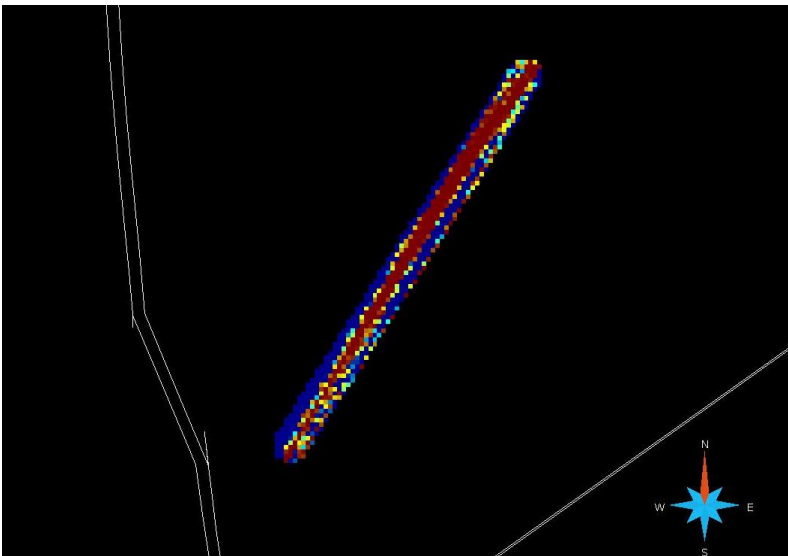
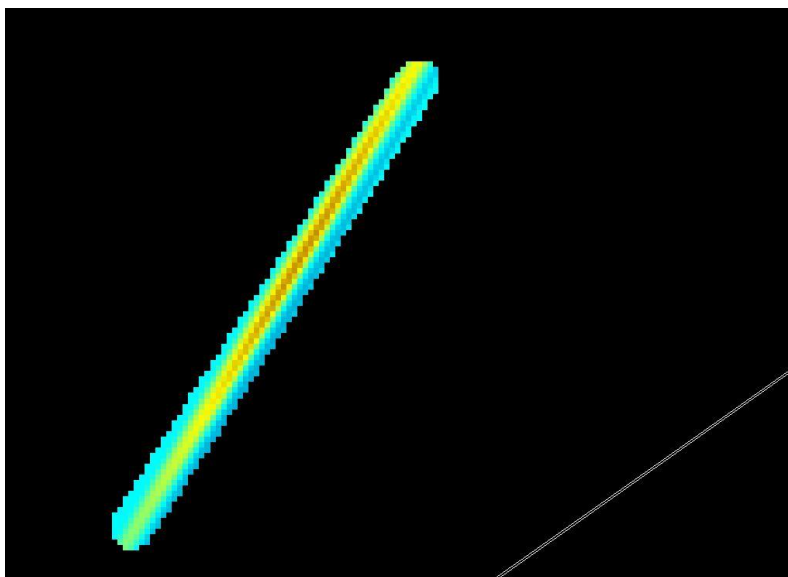
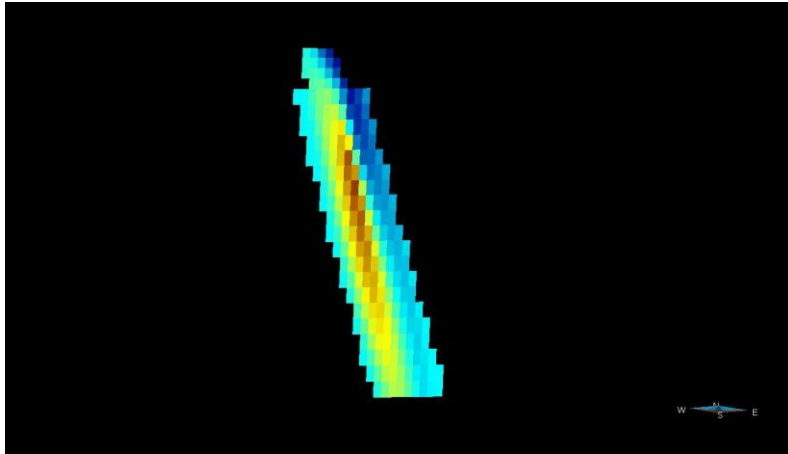


Fig. 156: A particular of the cross sections of fig. 3. Here we can see the three area of the reservoir. In the green area, the Loppio Formation is in contact laterally and above with the Rotzo Formation, this zone is a very good reservoir. In the yellow area the Loppio Formation is laterally in contact with the Monte Zugna Formation. Because this formation has low porosity and permeability, also this area of the Loppio can be consider a good reservoir. The last area is the black area. Here the Loppio Formation is in laterally in contact with the Monte Zugna Formation on the left and with the fault on the right. The reservoir potential depends from the permeability of the fault zone.

In fig.155, the fault related dolomitized bodies are represented with a constant porosity value (4,7%). We know from field observation that the high porosity value is concentrated in the breccia fault zone, in the middle of the dolomitized bodies while the external part are less porous. This observation is confirmed by the geostatistical analysis (Simple kriging and SGS) shown in Fig. 157.



*Fig. 157: The interpolation computed with the Simple Kriging looking from above (A) and from south (B) and the SGS simulation (C) looking from above. The geostatistic confirms that the higher value of porosity are concentrated in the middle of the fault related bodies corresponding to the zone dominated by fault breccias. Porosity scale is the same of fig. 154 and 155.*

## 6. Conclusion

The main goal of this work was to analyze the reservoir potential of the Monte Testa Jurassic synsedimentary structure, affected by fault related dolomitized bodies formed during Alpine tectonic (Di Cuia et al. 2011; Ronchi et al., 2012) and to reconstruct the porosity evolution of the structure. In order to achieve this purpose, a multi-method approach including geological mapping, structural and porosity analysis, photogrammetry and 3D geo-modelling was realized.

The geological map allows to recognize three main fault systems (NW-SE, N-S and NE-SW), to collect dip and azimuth data of fault planes and rock formations and to better understand shape and distribution of the fault related dolomitized bodies.

During the structural analysis, kinematic indicators data were collected from the fault planes and stress-tensors were derived using Wintesor software. This permit to recognize two main tectonic events. The first one was the Jurassic tectonic phase with an NE-SW main extension within a general oblate strain, which caused the formation of transtensive faults, tilting of the Loppio Formation and thickness variation of the Rotzo Formation. The upper part of Rotzo Formation seals the Jurassic faults, testifying that the Jurassic tectonic event vanished before the deposition of the upper part of the Rotzo Formation. The second tectonic event is related to the Alpine collision and was characterized by a N-S compression which led to the strike slip reactivation of the Jurassic faults and the circulation of the dolomitizing fluids responsible for the fault related dolomitized bodies.

The results from the porosity analysis suggest that dolomitized bodies have a porosity values that goes from 0% to 10,6% and the higher value can be found within the fault zones. At Present, the Rotzo Formation has no porosity, while Monte Zugna and Loppio Formation has a porosity given by fracturing with a value likely around 1%. The nowadays porosity values of Rotzo and Monte Zugna are very similar to those that the two formations could have during the Jurassic rifting, right after the deposition of the Rotzo Formation. On the contrary, the

initial porosity of the Loppio Formation could have reached values of 20% most probably not being completely cemented yet.

The photogrammetric 3D model was very useful to improve the resolution of the DTM (used as topographic base for the 3D geomodel), in the steep area of the Monte Testa. This allows to define faults plane and formation boundary of the Monte Testa main structure into the 3D geomodel.

Finally, from the 3D geomodel different information were extracted: geometry of faults and geometry and volume of rock formations, shape and distribution of the fault related dolomitized bodies, thickness map of Rotzo Formation, distribution and evolution of the porosity.

The geometric and volumetric reconstructions enabled me to verify if this type of structure can form favorable geometries for hydrocarbon accumulation, whereas the thickness map allowed to better understand the faults activity during the Jurassic extensional tectonics.

Finally, it was possible to distribute the porosity values into the 3D geomodel even with the help of geostatistical methods.

All these information together allowed to reconstruct the geometry and porosity evolution of the area from the Jurassic onward.

Right after the deposition of the Loppio Formation, characterized by an initial porosity of 20%, the extensional Jurassic tectonics begun dissecting the Loppio formation in several tilted blocks bounded by three fault systems (NW-SE, N-S and NE-SW) . In order to permit this brittle behavior, the Loppio Formation had to be already partially cemented and its porosity value was most likely lower than the initial 20% (let's say around 8%). Above the Loppio Formation the low porous and low permeable Rotzo Formation was deposited. In the lower part of this formation, great thickness variations are present testifying that the Jurassic faults were active during its deposition. On the contrary, the Jurassic faults are sealed by the upper part of the Rotzo Formation, which records the vanishing of the Jurassic extensional tectonics.

Thanks to the tectonic activity, right after the deposition of the Rotzo, the high porous tilted blocks of Loppio were put in contact laterally and above with the

low permeable Rotzo Formation creating very favorable potential traps for hydrocarbon accumulation. Furthermore, the increase in thickness with time of the Rotzo Formation created even a better seal within the synsedimentary structure.

Starting from this moment onwards the porosity of the Loppio Formation should have begun to decrease because of cementation until only fracture porosity remained. When this moment was reached, no hydrocarbon accumulation was any more possible.

The alpine tectonic caused the strike slip reactivation of the Jurassic faults and during Late-Paleocene-Early Eocene forced the dolomitizing fluids to flow along the fault zones leading to the formation of high porous fault-related dolomitized bodies with porosity values ranging from 0% to 10,6%. These bodies cross all the Monte Zugna Formation with a constant thickness of 30-40 m and when they reach the Loppio Formation the thickness decrease abruptly up to 0 m approaching the Rotzo Formation contact. These bodies are present along all the three fault systems but not along all the faults, this is due to the fact that probably some faults had not enough permeability to permit the circulation of the dolomitizing fluids. Only along the major faults the dolomitized bodies reached the lower part of the Rotzo Formation. The higher porosity values of these fault-related dolomitized bodies are indeed concentrated within the brecciated fault zone of Jurassic age. It is clear from these observations, that the inherited Jurassic structures played a primary role on the circulation of dolomitizing fluids. Indeed, the dolomitizing fluids followed the permeable breccia dominated fault zones created during the Jurassic tectonic event and when they reached the Loppio-Rotzo stratigraphic contact, their up-flow was impeded by the low permeability of the Rotzo Formation.

These porous bodies enclosed within low porous and permeable rock formations can be very good hydrocarbon reservoirs, giving a new life to the reservoir potential of the inherited synsedimentary structures.





## 7. Bibliography

- Bosellini, A. Castellarin, G.V. Dal Piaz e M. Nardin, 1999. Carta geologica del Trentino
- Avanzini, M. (1994) Tettonica distensiva e controllo di facies nel Giurassico del Monte Pasubio (Trentino Sudorientale): l'esempio di Alpe Alba. Stud. Trentini Sci. Natur. Acta Geol., 69, 71–79.
- Avanzini, M. and Masetti, D. (1992) Il filone sedimentario giurassico di Alpe Alba (M. Pasubio, Trento): un indicatore di tettonica distensiva polifasica. Att.Tic.Sc.Terra, 35, 47–52.
- Avanzini M., Masetti D., Romano R., Podda F., Pontono M., 2002. Carta Geologica d'Italia 1:50:000-elenco delle formazioni-Calcarei Grigi.
- Aydin, A. and Reches, Z., 1982. Number and orientation of fault sets in the field and in experiments. Geology, 10, 107–112.
- Bertotti, G., Picotti, V., Bernoulli, D., Castellarin, A., 1993. From rifting to drifting: tectonic evolution of the Southalpine upper crust from the Triassic to the Early Cretaceous. Sedimentary Geology 86 (1/2), 53e76.
- Bosellini A. and Hsu K.J., 1973 - Mediterranean Plate Tectonics and Triassic Palaeogeography. Nature, v. 249, n.5412, 144-146.
- Bosellini A., Gianolla P. and Stefani M., 2003 – *Geology of the Dolomites*. Episodes, v.26, 181-185.
- Bosellini A., Masetti D. and Sarti M., 1981 - A Jurassic “Tongue of the Ocean” infilled with oolitic sands: the Belluno Trough, Venetian Alps, Italy. Marine Geology, v.44, 59-95.
- Bosellini, A. and Broglio Loriga, C. (1971) I “Calcarei Grigi” di Rotzo (Giurassico inferiore, Altopiano di Asiago) e loro inquadramento nella paleogeografia e nella evoluzione tettono-sedimentaria delle Prealpi Venete. Ann. Univ. Ferrara, 5(1), 1–61.
- Bosellini, A., and Hardie, L.A. (1988) Facies e cicli della Dolomia Principale delle Alpi Venete. Soc. Geol. Ital. Mem., 30, 245-266
- Cannarozzo, R., Cucchiari L., Mestieri W. , 2012. Le forme del rilievo
- Castellarin A. 2010. Basic stratigraphy and tectonics of the Southern Alps around the Giudicarie Lineament (Southern Alps, Italy) Ital.J.Geosci. (Boll.Soc.Geol.It.), Vol. 128, No. 2 (2009), pp. 409-417, 7
- Castellarin, A. and Picotti, V., 1990. Jurassic tectonic framework of the eastern border of the Lombardian basin. Eclogae Geol. Helv., 83, 683–700.
- Castellarin, A., 1972. Evoluzione paleotettonica sinsedimentaria del limite tra Piattaforma Veneta e Bacino Lombardo a nord di Riva del Garda. Giorn. Geol., 38, 11–212. In Italian.
- Clari P. (1976) - Caratteristiche sedimentologiche e paleontologiche di alcune sezioni dei Calcarei Grigi del
- Coward M. P., Daltaban T. S., Johnson H. (1998) Structural geology in reservoir characterization, Geological Society, London, Special Publications, 127.

- D. Wiprut and M.D. Zoback, 2002. Fault reactivation, leakage potential, and hydrocarbon column heights in the northern North Sea. NPF Special Publication 11, pp. 203-219,
- Dal Piaz G.V., Bistacchi A., Massironi M., (2003). Geological outline of the Alps. EPISODES, vol.26; p.175-180, ISSN: 0705-3797
- Davies, G.J., and L.B. Smith, 2006. Structurally controlled hydrothermal dolomite reservoir facies: An overview: AAPG Bulletin, v. 90, p. 1641-1690
- Delvaux, D., Sperner, B., (2003). Stress tensor inversion from fault kinematic indicators and focal mechanism data: the TENSOR program. In: New Insights into Structural Interpretation and Modelling (D. Nieuwland Ed.). Geological Society, London, Special Publications 212, 75-100.
- Di Cuia, R., Riva, A., Scifoni, A., Moretti, A., Spotl, C., Caline, B., 2011. Dolomite characteristic and diagenetic model of the Calcari Grigi Group (Asiago Plateau, Southern Alps – Italy): an example of multiphase dolomitization. *Sedimentology*
- Enos, P., and L.H. Sawatsky, 1981, Pore networks in Holocene carbonate sediments: *Journal of Sedimentary Petrology*, v. 51, p.961-986
- Etchecopar, A., Vasseur, G., Daignie`res, M., 1981. An inverse problem in microtectonics for the determination of stress tensors from fault striation analysis. *Journal of Structural Geology* 3, 51–65
- Fossen, H., (2010), *Structural Geology*. Cambridge Press. 463 pp.
- Franceschi, M., Massironi, M., Franceschi, P., Picotti, V., 2014. Spatial analysis of thickness variability applied to an Early Jurassic carbonate platform in the central Southern Alps (Italy): a tool to unravel syn-sedimentary faulting. *Terra Nova*, 26, pp. 239-246, DOI: 10.1111/ter.12092
- From Schmoker, J.W. and R.B. Halley, 1982, Carbonate Porosity Versus Depth: A predictable Relation for South Florida: AAPG Bulletin, v.66, p.2561-2570.
- Geoff Bohling, 2007. *Hydrogeophysics: Theory, Methods, and Modeling*. Boise State University, Boise, Idaho
- Gluyas JG and Swarbrick RE (2003) *Petroleum Geoscience*. Oxford: Blackwell Science.
- Healy, D., Jones, R.R. and Holdsworth, R.E., 2006. Three-dimensional brittle shear fracturing by tensile crack interaction. *Nature*, 5, 64–67
- Iannace, A., Frisia, S., 1994. Changes in dolomitization patterns between Norian and Rhaetian in the Southern Tethys realm: clues to dolomitization of Dolomia Principale. In: Purser, B., Tucker, M., Zenger, D. (Eds.), *Dolomites, a Volume in Honour of Dolomieu*. Spec. Pub., vol. 21. International Association Sedimentologists, pp. 75e89.
- Jacquemyn C, Huysmans M, Hunt D, Casini G, Swennen R. et al., 2015, Multi-scale three-dimensional distribution of fracture- and igneous intrusion-controlled hydrothermal dolomite from digital outcrop model, Latemar platform, Dolomites, northern Italy, AAPG BULLETIN, Vol: 99, Pages: 957-984, ISSN: 0149-1423
- Krantz, R.W., 1988. Multiple fault sets and three-dimensional strain: theory and application. *J. Struct. Geol.*, 10, 225–237.
- Loreau, J.-P., and B. H. Purser, 1973, Distribution and ultrastructure of Holocene ooids in Persian Gulf, in B.H. Purser, ed., *The Persian Gulf*, New York, SpringerVerlag, p.279-328.

- Loucks, R. G., and C. R. Handford, 1992, Origin and recognition of fractures, breccias, and sediment fills in paleocave-reservoir networks, in M. P. Candelaria, and C. L. Reed, eds., *Paleokarst, Karst-Related Diagenesis and Reservoir Development: Examples from Ordovician-Devonian Age Strata of West Texas and the Mid-Continent, Midland, TX, Permian Basin Section- SEPM Publication 92-33*, p. 31-44.
- Loucks, R. G., M. M. Dodge, and W. E. Galloway, 1986, Controls on porosity and permeability of hydrocarbon reservoirs in lower Tertiary sandstones along the Texas Gulf Coast: The University of Texas at Austin, Bureau of Economic Geology Report of Investigations No. 149, 78 p.
- Masetti, D., Claps, M., Giacometti, A., Lodi, P., Pignatti, P., 1998. I Calcari Grigi della Piattaforma di Trento (Lias Inferiore e Medio, Prealpi Venete). *Atti Ticinensi di Scienze della Terra* 40, 139e183. Pavia.
- Møller-Pedersen P., Koestler A. G., eds (1997) *Hydrocarbon Seals: Importance for Exploration and Production (Norwegian Petroleum Society), Special Publication, 7*.
- Moretti A., 2007. *Tettonica distensiva sin-sedimentaria giurassica nella Valsugana centro occidentale*
- Moore C. H., *Carbonate Reservoirs, Porosity Evolution and Diagenesis in a Sequence Stratigraphic Framework*, 2001.
- Oliver M. A., Webster R., *A tutorial guide to geostatistic: Computing and modeling variograms and kriging* Catena 113, 56-69.
- P.J. Gibson and C. H. Power, 2000. *Introductory Remote sensing. Digital Image Processing and Applications*.
- Paradigm, Structure and stratigraphy*, 2011
- Philip A. Allen and John R, 2013. *Basin Analysis*, third edition
- Reches, Z., 1978. Analysis of faulting in three-dimensional strain field. *Tectonophysics*, 47, 109–129.
- Robinson, R. B., 1967, Diagenesis and porosity development in Recent and Pleistocene oolites from southern Florida and the Bahamas: *Journal of Sedimentary Petrology*, v. 37, p.355-364
- Romano, R., Barattolo, F., Masetti, D., 2005. Biostratigraphic evidence of middle Liassic Hiatus in the Foza section (Eastern sector of the Trento Platform, Calcari Grigi Formation, Venetian Prealps). *Bollettino della Società geologica Italiana* 124, 301e319.
- Ronchi, P., Masetti, D., Tassan, S., Camocino D., 2012. Hydrothermal dolomitization in platform and basin carbonate succession during thrusting: A hydrocarbon reservoir analogue (Mesozoic of Venetian Southern Alps, Italy), *Marine and Petroleum Geology* 29, 68-89.
- S. A. Drury, 1993. *Image Interpretation in geology*
- S. Qing Sun, 1995. Dolomite reservoirs; porosity evolution and reservoir characteristics *AAPG Bulletin*, v. 79, p. 186-204
- Sailer, A. H., D. A. Budd, and P. M. Harris, 1994a, Unconformities and porosity development in carbonate strata: ideas from a Hedberg Conference: *American Association of Petroleum Geologists Bulletin*, v. 78, p. 857-872.

Sailer, A. H., J. A. D. Dickson, and S. A. Boyd, 1994b, Cycle Stratigraphy and Porosity in Pennsylvanian and Lower Permian Shelf Limestones, Eastern Central Basin Platform: American Association of Petroleum Geologists Bulletin, v. 78, p. 1820-1842.

Saller A. 2013. Diagenetic evolution of porosity during burial. AAPG Search and Discovery Article #90159©2012 AAPG Foundation Distinguished Lecturer Series 2012-2013.

Shinn, E. A., 1968, Practical significance of birdseye structures in carbonate rocks: Journal of Sedimentary Petrology, v. 38, p.215-223

Skua User Manuals 2009.2

Structurally Complex Reservoirs. 292. ed. 2007. P

Tucker, M. E., and V. P. Wright, 1990, Carbonate Sedimentology: Oxford, Blackwell Scientific Publications, 482 p.

Veneto. Mem. Sc. Geol., 31: 1-63, Padova

Wang G., Li P., Hao F., Zou H. and Yu X., 2015. Dolomitization process and its implications for porosity development in dolostones: A case of study from the Lower Triassic Feixianguan Formation, Jiannan area, Eastern Sichuan Basin, China. Journal of Petroleum Science and Engineering 131 (2015) 184-199.

Weber, K.J. and M. Bakker 1981. Fracture and vuggy porosity. Proceedings of the 56th Society of Petroleum Engineers Annual Fall Technical Conference, San Antonio, Texas, 1981, SPE paper 10332, p. 1-11.

Zampieri, D. (1995) Tertiary extension in the Southern Trento Platform, Southern Alps, Italy. Tectonics, 14, 645–657.

## Webgraphy

<https://plot.ly/>

Arcgis\_help

<http://vsp.pnnl.gov/>

spatial anlyst.net







## 8.Thanks

Ci sono moltissime persone che devo ringraziare. Sia quelle che mi hanno aiutato durante la realizzazione di questo lavoro ma anche tutti gli amici che ho avuto la fortuna di incontrare durante questi anni di università e con i quali ho passato dei momenti indimenticabili.

Prima di tutti, devo ringraziare i miei genitori, che mi hanno dato l'opportunità di svolgere questo percorso e mi hanno sempre sostenuto durante questi anni permettendomi di fare quello che mi piace.

Ci sono poi tutti i miei coinquilini che hanno reso speciale gli anni passati a Padova. Lorenzo, Pietro, Nicola, Davide, Simone, Andrea, Giordano, Valeria, Debora, Piergiorgio e Margherita senza di voi quest'avventura non sarebbe stata così bella.

Non posso poi dimenticare tutti i miei compagni di corso. Ringrazio tutti per gli splendidi momenti e le grandi avventure che abbiamo passato assieme, ma un ringraziamento particolare va a Federico, Paolo, Riccardo e Ilaria.

Un grandissimo buona caccia a tutti i lupetti, a tutti i vecchi lupi e a tutti gli scout del Gruppo Pegine 1 che in questi anni ho avuto la fortuna di incontrare e con i quali ho vissuto molti dei momenti più belli della mia vita

Devo ora ringraziare coloro che mi hanno aiutato in questo lavoro.

Durante la realizzazione di questa tesi, ho avuto l'occasione e la fortuna di poter conoscere e collaborare con moltissime persone le quali in un modo o nell'altro hanno contribuito a realizzarla ed arricchirla.

Ringrazio: il mio relatore Matteo Massironi, che mi ha seguito durante tutta lo svolgimento di questo lavoro; Marco Franceschi il quale è stato un aiuto e un amico fondamentale durante tutte le fasi della tesi; Raffaele Di Cuia e Alberto Riva di Geplan consulting per gli indispensabili consigli sulla geologia del petrolio e per i miglioramenti portati al progetto; Alessandro Rizzi e Cinzia Slongo di SMART3K S.r.l di Trento, per l'aiuto durante la realizzazione del modello fotogrammetrico; Andrea Bistacchi per i preziosi consigli sulla modellazione 3D e la geostatistica; tutte le persone del dipartimento di

Geoscienze che hanno in qualche modo contribuito, Michele Secco, Leonardo Tauro, Stefano Castelli, Nicola Praticelli, e infine le persone che mi hanno accompagnato durante il rilevamento, mio Papà e poi gli amici Federico, Simone, Andrea, Giordano, Francesco.

Voglio poi ringraziare tutti gli amici della palestra di arrampicata Intelligenza project di Padova con cui ho condiviso molti viaggi e avventure e con i quali spero di porterne fare ancora in futuro.

Un pensiero e un ringraziamento particolare vanno a Franco e Lulli, grazie per tutto, per le cene, per le arrampicate e per i bellissimi momenti passati assieme.

**GRAZIE A TUTTI**